Publications of the Astronomy Department of
the Eötvös Loránd University
Vol. 20.

5TH AUSTRIAN HUNGARIAN WORKSHOP

ON CELESTIAL MECHANICS

Wien, Austria, 09-10 April, 2010

EDITED BY

Á. Süli

Published by the Department of Astronomy of the Eötvös University
Budapest 2011

ISBN 963 463 557
Responsible publisher: Dr. Áron Süli

Contents

Preface

Solar System

Exoplanetary Systems

Miscellaneous

Preface

The 5^{th} Hungarian-Austrian Workshop on Celestial Mechanics took place from 9^{th} until the 10^{th} of April 2010 in Vienna, Austria. The workshop was held in the Institute for Astronomy of Vienna University. From the Etvs University and from the host institute experts and PhD students gathered together to discuss the challenges and new results of the actual problems of celestial mechanics.

The workshop was held in the meeting room at the *Sternwarte* of the Vienna University located in a magnificent park in the heart of Vienna. Following the themes of the four previous events the focus for this workshop ranged from the Trojan problem, dynamics in binary star systems and exoplanetray systems. We were pleased to acknowledge the support of the host university.

The talks were characterized by a large spectrum, which is typical of the workshops on celestial mechanics. Several talks discussed different aspects of the trojan problem, such as the three Trojan problem, dynamics of trojan-like planets in binary stars, the frequencies of their motion around the triangular lagrangian points, etc. Several speakers focused on the formation and dynamics of planetary systems, like exoplanets in higher order mean motion resonances, evolution of exoplanets in binary systems, stability of exomoons and the forging of the planets in the Solar System. Some of the presentation used sophisticated mathematical tools in order to understand mean motion resonances, the Sitnikiv problem applying the KAM and the Nekhoroshev theorem. The theme of a number of talks was the motion of Solar System bodies: dynamics of the newly discovered moons of Pluto and of near-Earth asteroids. General problems were also addressed, among others chaos in Hamiltonian systems, adaptive Lie-integration method and iterative solution approximation to the generalised Sitnikov problem.

Budapest, 30 June, 2011

Áron Süli


STERNWARTE

PART ONE

SOLAR SYSTEM

PADEU
PADEU **20**, 5 (2011)
ISBN 963 463 557

Dynamics of possible Uranus Trojans

Ákos Bazsó and Rudolf Dvorak

Institute for Astronomy, University of Vienna, Türkenschanzstraße 17, A-1180 Vienna, Austria

E-mail: `akos.bazso@univie.ac.at`

Abstract
We conducted a dynamical survey to find the properties of—and influences on—the motion of hypothetical Trojan asteroids around Uranus. For low eccentric orbits, we integrated a set of more than 6000 Trojans with different initial semi-major axes and inclinations up to $i = 60^\circ$. The general integration time was set to 100 Myr, some selected orbits were integrated for a time span covering the age of the Solar System. We found two regions at which a Trojan can remain in a low libration amplitude state for at least 100 Myr, one at low inclinations up to 6°, and the other at higher inclinations from 40° to around 50°. Using frequency analysis on the output of numerical integrations we identified several important secular resonances. Those secular resonances with Jupiter and Neptune affect the motion of the Uranus Trojans, and shape the stability region around the equilateral equilibrium points. Although there is a fast depletion of Trojans within 100 Myr, the two stable regions would support the long-time presence of Trojans.

Keywords: *planet: Uranus – minor planets: Trojan asteroids – secular resonances – long-term stability*

1 Introduction

Trojan Asteroids are considered common objects of the Solar System today. They form a special group of asteroids in 1:1 Mean Motion Resonance (MMR) with a planet, having roughly the same semi-major axis and orbital period. Trojans are located near the so-called Lagrangian points L_4 and L_5, named after the French mathematician Lagrange[1], who found five particular solutions to the restricted three body problem. The points L_4 and L_5 form equilateral triangles with the primary and secondary mass, thus a Trojan is leading (L_4) or trailing (L_5) the planet it accompanies at an angle of about 60°.

For a long time the solutions were considered without an implication for the Solar System, but in 1906 the German astronomer Wolf[2] observed the object now known as (588) Achilles (Wolf , 1907), which turned out to be just the first one of the class of asteroids moving around the Lagrange points of Jupiter (Nicholson , 1961). Since then several thousand Trojans are known to accompany Jupiter[3]; also Mars and Neptune Trojans have been found. Though there is no lack of observational effort to find Saturn and Uranus Trojans, none of these objects has been discovered yet.

The solutions found by Lagrange are strictly valid only for the restricted three body problem, and consequently many studies of the Trojans applied this model, e.g. Érdi (1988); Lohinger & Dvorak (1993) for the elliptic restricted problem.

For a detailed study of the dynamics of Trojans—under the influence of the giant planets—it is necessary to resort to numerical integrations. Some of these studies were dedicated to Jupiter Trojans, e.g. Dvorak & Schwarz (2005); Robutel & Gabern (2006), while others also treated the possibility of Trojans for the other giant planets. The study by Holman & Wisdom (1993) concluded that there were no signs for Saturn, Uranus and Neptune not to retain Trojan-like asteroids for time scales of 20 Myr. Later Nesvorný & Dones (2002) intended to give a broader picture on the Trojans of the outer planets. They considered a primordial Trojan population orbiting Saturn, Uranus and Neptune, which was depleted by various effects. Their results suggested that Neptune could still have retained 50% of its original Trojan population, whereas for Saturn and Uranus the numbers decreased by a factor of 100, but this still did not rule out the possibility to detect Trojans. Marzari et al. (2003) used the Frequency Map Analysis (FMA) to determine the long-term stability of Trojans of the giant planets. Only for Jupiter and Neptune it was found, that a substantial number of Trojans is possible, for the other planets a high diffusion rate is responsible for short lifetimes.

The discovery of moderately inclined Neptune Trojans with $i \leq 30°$ (Sheppard & Trujillo , 2006, 2010) triggered investigations about highly inclined Nep-

---

[1] Joseph-Louis Lagrange (1736-1813)

[2] Max Wolf (1863-1932)

[3] for a list of Trojans see the web pages of the Minor Planet Center at: http://www.cfa.harvard.edu/iau/lists/Trojans.html

tune Trojans (Dvorak et al. , 2008; Zhou et al. , 2009). The latter investigated the dynamical behaviour of highly inclined Neptune Trojans with inclinations up to 60°. They used a frequency analysis method and identified three distinct stable regions, of which one lies at $51^\circ \leq i \leq 59^\circ$. To find stable Trojans for such high inclinations motivated our present study of inclined Uranus Trojans, since the earlier studies only considered inclinations up to 30°.

2 Methods

Our basic model is the 5-body problem consisting of the Sun and the planets Jupiter to Neptune, the Outer Solar System (OSS). The hypothetical Trojans of Uranus are considered as massless test particles, moving under the purely Newtonian gravitational attraction of the planets. The initial conditions for the planets were obtained from the JPL ephemeris[4]. For the Trojans we used an equidistant grid in the range $a_{\mathrm{T}} \in 18.9(0.005)19.4$ AU and $i_{\mathrm{T}} \in 0(1)60^\circ$. The initial values of the elements (e, Ω, M) were set to the values of Uranus, and we fixed $\omega_{\mathrm{T}} = \omega_{\mathrm{U}} \pm 60^\circ$. For most of the work we only considered motion about L_4, since—apart from a slight shift in the position of the libration centre, due to the choice of initial condition for the OSS—the motion is dynamically equivalent.

We integrated the equations of motion with the Lie-series method, based on the work of Hanslmeier & Dvorak (1984). This method enables the user to use an adaptive step-size, and in our application this is highly recommendable, since Trojans can have close approaches with planets when their orbits become chaotic. For this possibility we devised some methods to distinguish between tadpole and horseshoe orbits.

First we have applied a criterion based on the **libration amplitude** defined by $\sigma = \lambda - \lambda_{\mathrm{U}}$, where λ is the mean longitude; we take a mean value by $\langle\sigma\rangle = \sigma_{\max} - \sigma_{\min}$. If this value exceeds 180°, then the Trojan leaves the vicinity of L_4 (resp. L_5) and—by crossing the point L_3—can librate about L_5 (resp. L_4); in this case we do not consider it to be a Trojan any more.

The next method we applied is the **maximum eccentricity method** (MEM), which simply gives the highest eccentricity value a body has obtained during the course of the integration. This value will only give a coarse measure of regular or chaotic behaviour, but we can use it as a threshold. We have observed that there is a rather sharp boundary of the libration zone (see Fig. 1). The transition from libration to circulation occurs, whenever a Trojan obtains a maximum eccentricity of $e > 0.2$. For an even larger maximum eccentricity of

---

[4] see http://ssd.jpl.nasa.gov/

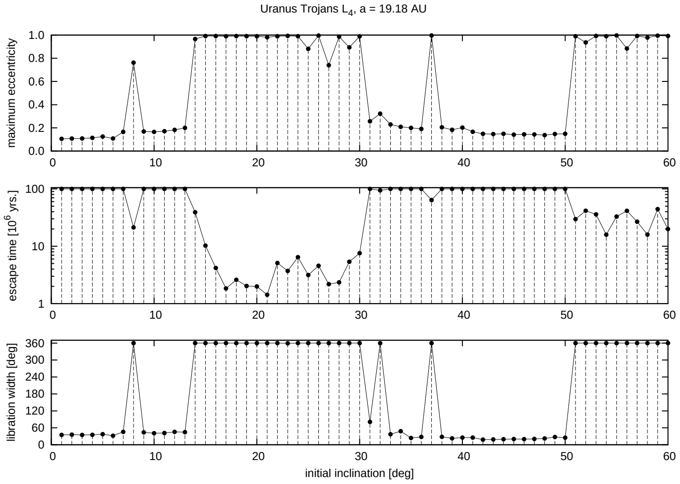

Figure 1: *Cut in inclination for Trojans about L_4, in all cases the values are given after 100 Myr of integration time. The top picture shows the maximum eccentricity, the middle picture depicts the escape time, and the bottom picture displays the libration amplitude.*

$e > 0.5$ it follows, that the body will have a large libration amplitude and will move away quite fast from the vicinity of the libration point, thus we adopted this as a cut-off value to distinguish libration from circulation.

The third method combines two empirical cut-off values for the semi-major axis and eccentricity to give an estimate of the **escape time** of a Trojan. We use the cut-off value from above for the eccentricity.

For carrying out the **frequency analysis** part we have used the program package SigSpec[5] by Reegen (2007). We convert the data from the numerical integration into the Laplace-Lagrange secular variables (h, k, p, q) (see Morbidelli (2002) and Murray & Dermott (1999) for details) via the transformations $k = e\cos(\omega + \Omega)$, $q = \sin i \cos\Omega$. Then SigSpec computes the spectral significance levels for the DFT amplitude spectrum of a time series at arbitrarily given sampling.

---

[5] for a description and the manual see:
http://homepage.univie.ac.at/peter.reegen/manual/3Manuals.html

3 Results

This section summarizes the results obtained from the analysis of the dynamical behaviour of the Uranus Trojans. We will briefly discuss different aspects that became evident during our investigations.

3.1 Cut for L_4

In a first step we studied the Trojans very closely located to the libration points L_4 and L_5 by means of cuts for different inclinations, but for a fixed initial semi-major axis of $a_{\mathrm{L}_4} = 19.18$ AU (resp. 19.28 AU for L_5). The different values are due to the choice of initial conditions, the "true" libration points in a three-body-problem would lie in between these two values. The calculations were carried out for 100 Myr, they reveal four distinct zones with low libration amplitudes in Fig. 1, interspersed with zones of chaotic motion.

It is also well visible from Fig. 1 that there are two extended regions which do not allow regular Trojan type motion, one ranges approximately from $14° \leq i \leq 30°$, and the other covers all values of $i > 50°$. We will give an explanation for this in the section with the frequency analysis.

3.2 Libration amplitudes

To give a more complete picture of the (a, i) parameter space we chose to compare the libration amplitudes for two different times, i. e. after 1 Myr and 100 Myr. This will give an impression of the different diffusion speeds as well as secular effects on the Trojans. However, Fig. 2 also shows the shrinking of the low libration amplitude zone especially for higher inclinations. For low inclinations the area shrinks as well, but at a lower rate. The arc shaped gaps in Fig. 2 (b) correspond to the locations already found in the cut in Fig. 1, and these must correspond to secular resonances.

As a consequence of this calculations we could compile a figure showing the different diffusion rates of Trojans. In total about 3100 initial conditions for Trojans were considered, for every value of the inclination in steps of 1° we traced how many objects had failed our constraints for Trojan motion mentioned above. The results are shown in Fig. 3, the bold line summarizes the average fraction of remaining Trojans over all inclinations. As expected from previous analysis, the fraction of surviving test particles is highest for low inclinations, whereas for inclinations between $i = 20 - 30°$ it is lowest.

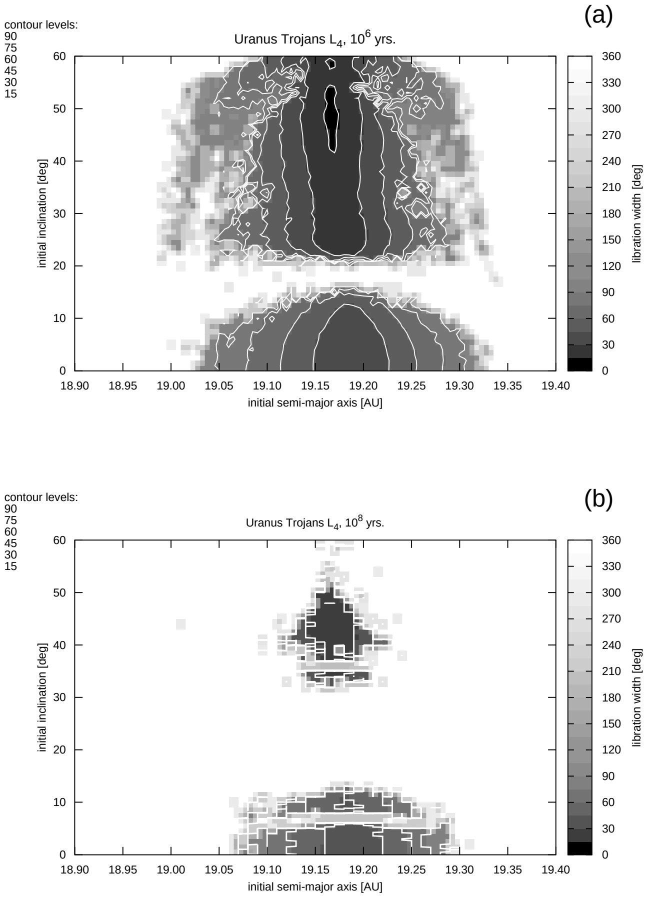

Figure 2: *Parameter plane semi-major axis vs. inclination: The colour code shows the libration amplitude for (a) T = 1 Myr (top), and (b) for T = 100 Myr (bottom). The white contour curves connect equal levels of the libration amplitude for selected values as indicated in the inset, from* $15 - 90^\circ$. *Note that low amplitude curves need not necessarily be present for the bottom picture.*

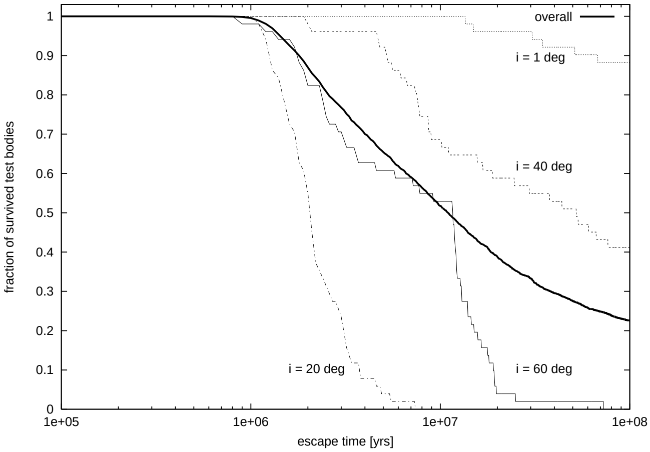

Figure 3: *Fraction of remaining Trojans versus escape time for different inclinations, the bold line gives the summary over all inclinations. The slope of the curve is similar to the one in figure 10 of Nesvorný & Dones (2002), but here we find that still about 20% of the Trojans survived after 100 Myr.*

3.3 Secular frequencies

Using the program SigSpec and overlapping time-windows with a width of $\Delta t = 10$ Myr we obtained a list of dominant secular frequencies in the signal of the variables (k, q), which we had to compare to the known secular frequencies in the OSS (see Tables 2 and 3 in Laskar (1990)). Table 1 gives an overview of these secular frequencies.

We show in Fig. 4 as an example the analysis covering the first 10 Myr of the Trojan with semi-major axis $a = 19.185$ AU, being the closest one to the point of minimum libration amplitude. The proper frequency (solid curve) is smoothly changing with increasing inclination, so that it can be separated from the (nearly) constant secular eigenfrequencies of the planets (and their combinations, horizontal lines). Whenever the proper frequency curve crosses one of the horizontal lines, the Trojan enters into a secular resonance. This effect is visible starting at low inclinations, where the curve crosses the $2g_5 - g_7$ resonance with Jupiter and Uranus, which causes the lower gap in Fig. 2 (b). At about $i = 15°$ (for this value of the semi-major axis) the Trojan enters into the linear secular resonance with Jupiter and this causes a fast increase

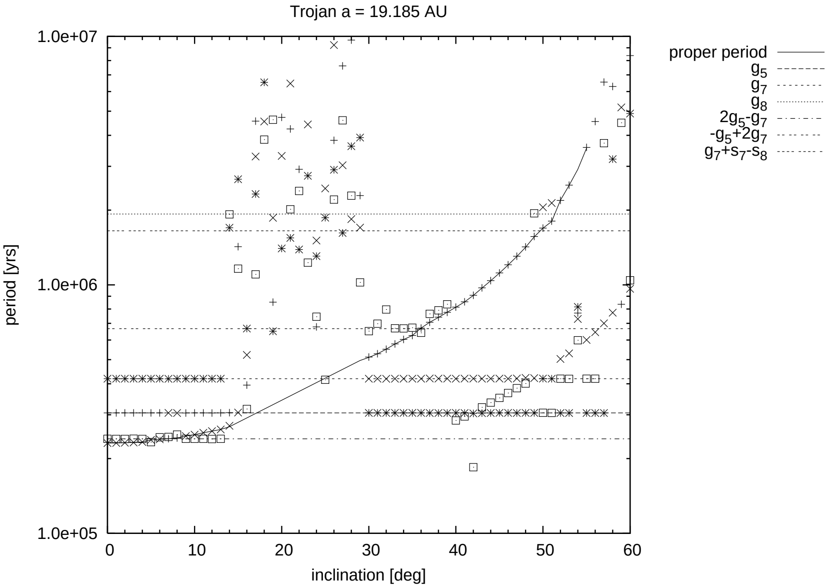

Figure 4: *Change of proper frequency (shown as the period in years) with inclination for a selected Trojan during the first 10 Myr. The upper curve corresponds to the proper frequency, while the lower one is its combination with another frequency. The horizontal lines are the quasi-static secular eigenfrequencies of the major planets Jupiter (g_5), Uranus (g_7) and Neptune (g_8), as well as some of their combinations. The different types of symbols just denote an ordering of frequencies after their amplitude. The recovered periods in the range $15^\circ \leq i < 30^\circ$ are artifacts, since in this region the Trojans exhibit chaotic motion (cf. Figs. 1, 2).*

in eccentricity and effectively removes the Trojans from the libration region. Following the curve we observe that it enters into linear secular resonance with Uranus, which causes the same effect but is acting on a somewhat longer timescale. The gap at $i \approx 35^\circ$ in the upper part of Fig. 2 (b) is thus related to another secular resonance involving Jupiter and Uranus ($-g_5 + 2g_7$), while at inclinations $i \geq 50^\circ$ also Neptune plays a role via g_8. Since the secular periods for Neptune are > 1 Myr they only take effect for longer integrations, and this also explains the comparatively strong shrinking of the high inclination libration zone in Fig. 2 (b).

Table 1: *Selection of important secular frequencies for the dynamics of Uranus Trojans. These values (for simplicity given as periods) were detected in the dynamical spectra of Trojans from the numerical integrations. The last line—denoting the quasi-mean-motion-resonance between Uranus and Neptune—is mainly found in combination with other secular frequencies from the table.*

combination	periods [10^3 yrs]
g_5	305.2
g_6	45.7
g_7	419.2
g_8	1928.0
$2g_5 - g_7$	240.1
$-g_5 + 2g_7$	666.8
$g_7 + s_7 - s_8$	1650.6
MMR 2:1 Uranus/Neptune	4.236

4 Conclusions

We have shown that Uranus Trojans are possible at low ($i \leq 7°$) and moderate ($i \approx 40°$) inclinations, for dynamical life-times of up to 5×10^8 years. There are well separated zones in the inclination range investigated allowing for low libration amplitude "classical" Trojan motion, cut by secular resonances. These resonances involve the planets Jupiter, Uranus and Neptune, but not (directly) Saturn, and they provide strong limitations on the long-term dynamical stability of the Trojans. From a given number of primordial (captured) Trojans we find that between 20% (for 100 Myr) and only 1% (for > 1 Gyr) remain (Nesvorný & Dones (2002)), making it hard to find them. In our opinion the most promising case would be to search for low inclination Trojans, but the effects of increasing the eccentricity on the stability have still to be studied.

Acknowledgement

The authors thank for the support through Austrian Science Foundation (FWF) project P18930-N16. We also thank Dr. P. Reegen for valuable discussions on the frequency analysis procedure, as well as Dr. L.-Y. Zhou for giving detailed insights into his work on Neptune Trojans. We appreciate the help of Dr. R. Schwarz, who carefully read the text and suggested many improvements.

References

Dvorak, R., Lhotka, C., Schwarz, R.: 2008, *Celest. Mech. Dyn. Astron.*, **102**, 97-110

Dvorak, R., Schwarz, R.: 2005, *Celest. Mech. Dyn. Astron.*, **92**, 19-28

Érdi, B.: 1988, *Celest. Mech.*, **43**, 303-308

Hanslmeier, A., Dvorak, R.: 1984, *A&A*, **132**, 203-207

Holman, M. J., Wisdom, J.: 1993, *AJ*, **105**, 1987-1999

Laskar, J.: 1990, *Icarus*, **88**, 266-291

Lohinger, E., Dvorak, R.: 1993, *A&A*, **208**, 683-687

Marzari, F., Tricarico, P., Scholl, H.: 2003, *A&A*, **410**, 725-734

Morbidelli, A.: 2002, "Modern Celestial Mechanics", London: Taylor & Francis

Murray, C. D., Dermott, S. F.: 1999, "Solar System Dynamics", Cambridge University Press

Nesvorný, D., Dones, L.: 2002, *Icarus*, **160**, 271-288

Nicholson, S. B.: 1961, *Leaflet of the Astronomical Society of the Pacific*, **8**, 239

Reegen, P.: 2007, *A&A*, **467**, 1353-1371

Robutel, P., Gabern, F.: 2006, *MNRAS*, **372**, 1463-1482

Sheppard, S. S., Trujillo, C. A.: 2006, *Science*, **313**, 511-514

Sheppard, S. S., Trujillo, C. A.: 2010, *Sciencexpress*, doi: 10.1126/science.1189666

Wolf, M.: 1907, *Astron. Notes*, **174**, 47-65

Zhou, L.-Y., Dvorak, R., Sun, Y.-S.: 2009, *MNRAS*, **398**, 1217-1227

PADEU | PADEU **20**, 15 (2011)
ISBN 963 463 557
© Published by the Astron. Dept. of the Eötvös Univ.

The Three Trojan Problem

Rudolf Dvorak and Ákos Bazsó

Institute for Astronomy, University of Vienna, Türkenschanzstraße 17, A-1180 Vienna, Austria

E-mail: `dvorak@astro.univie.ac.at`

Abstract
This paper is devoted to the stability study of three Trojan planets around a central star of 1 M_{Sun} in a distance of 1 AU. In an earlier study it was found for three Trojans in coorbital configuration, that if the angular separation is $47^\circ\!.4$, their motion is stable. We investigated the largeness of the stable region around the Lagrangian point L_4 by using numerical integrations, depending on the mass parameter and the distances of the three planets.

Keywords: *Trojan planets – celestial mechanics*

1 Introduction

The discovery of a Jupiter Trojan in 1906 (Achilles by Max Wolf in Heidelberg) proved that the equilateral equilibrium points in the three body problem Sun–Jupiter–asteroid are in fact populated by celestial bodies. Ever since many of such Trojan asteroids of Jupiter have been found and now we have knowledge of several thousands of objects in the 1:1 mean motion resonance (MMR) with Jupiter. Many investigations have been undertaken in different dynamical models like in the restricted three body problem (Érdi & Sándor , 2005; Érdi et al. , 2007), but also in the realistic dynamical model of the outer Solar System consisting of Jupiter, Saturn, Uranus and Neptune, like in e.g. Dvorak et al. (2004); Freistetter (2006); Schwarz et al. (2004); Robutel et al. (2005), or in a binary system (Schwarz et al. , 2009b).

In most of these studies the body close to the equilibrium point was taken to be massless, but in fact even massive planets may stay there in stable orbits

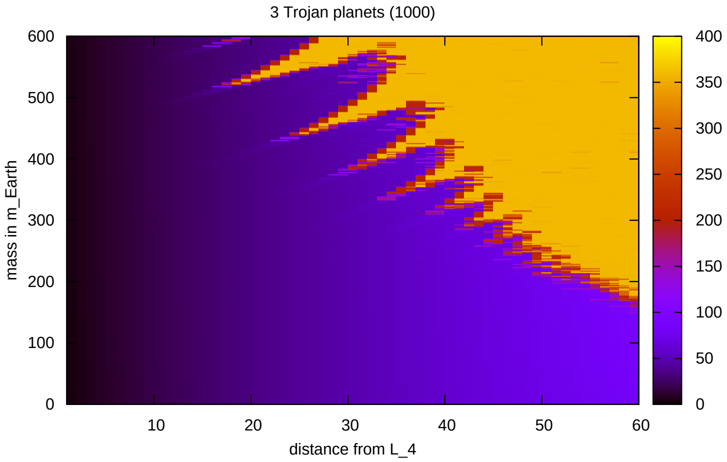

Figure 1: *Stability diagram for three equally massive Trojans: angular distance from the Lagrange point* L_4 *(*$i_{7c} = 47^\circ\!.4$*) versus the mass (in* $m_{\rm Earth}$*). The colors indicate the largest deviation from the equilibrium point in degrees.*

(Beaugé et al. , 2007; Chiang & Lithwick , 2005). As an interesting problem, we deal in this study with three massive bodies (planets) in the Trojan configuration, such that they are close to the 1:1 MMR, having almost the same semi-major axes and quasi circular orbits. The question of whether Trojans can form around the equilibrium points, and if they would be observable in extrasolar systems was addressed by different investigations, e.g. Caton et al. (2000); Davis et al. (2001); Laughlin & Chambers (2002); Ford & Gaudi (2006); Ford & Holman (2007).

Our investigation was undertaken using numerical computations for different initial configurations of the three planets. The basis of the present work was a very interesting article 'On the dynamics of coorbital satellite systems' by Salo & Yoder (1988), where the authors put up to 9 bodies with equal masses on a ring around a central body, but with different angular separation. For the most interesting case for a possible realisation in satellite systems or extrasolar

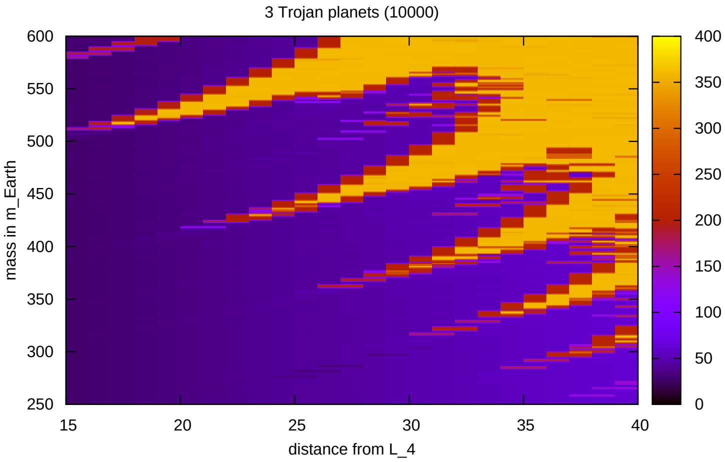

Figure 2: *Zoomed stability diagram for three equally massive Trojans; captions like in Fig. 1.*

planetary systems, we limited our research to three massive bodies on a 'ring'. But many more stable configurations are possible as was shown in a recent paper (Smith & Lissauer , 2009), where on different rings around a central body up to more than 200 planets may stay in stable orbits. The authors claim that in extreme extrasolar planetary system – although almost infinitely impossible – 'advanced civilizations may choose to construct planetary systems of this type in order to support a far larger population than on a single planet or even nested planets'. In our study we stay as close to reality as possible and limit – as mentioned – the dynamical system to three Trojans on a ring.

2 The model and the method of investigation

According to the results by Salo & Yoder (1988) two particles in the 1:1 MMR are stable with an angular separation of 60°; when we have 3 massive bodies on a ring the stable equilibrium points (in the following the leading point will be called L_4) are separated by 47°.4 on both sides of the body in the middle position.

Our model was the gravitational 4-body problem consisting of a central mass (a star) and less massive bodies (planets) in the Trojan position as it was stated before. We applied the Lie-integration code (e.g. Hanslmeier & Dvorak (1984); Lichtenegger (1984)), an already well tested method using an automatic step size which we have already used in many recent numerical computations (e.g. Schwarz et al. (2009a)). In a first step the three planets were given the same masses ($m_1 = m_2 = m_3$) with a central star ($m_0 = 1M_{\mathrm{Sun}}$) and the semi-major axes of the planets $a = 1$ AU. In a second step we gave the central Trojan planet the mass of Jupiter and varied only the masses of the accompanying planets. For different grids in masses (units in m_{Earth}) and in angular distance λ from L_4 the stability plots were computed:

- **Run 1** $\Delta m = 5m_{Earth}$ for $m_{Earth} < m_{123} < 2m_{Jupiter}$; $\Delta\lambda = 1^\circ$ for $0^\circ < \lambda < 60^\circ$.

- **Run 2** $\Delta m = 5m_{Earth}$ for $250m_{Earth} < m_{123} < 2m_{Jupiter}$; $\Delta\lambda = 1^\circ$ for $15^\circ < \lambda < 40^\circ$.

- **Run 3** $\Delta m = 1m_{Earth}$ for $400m_{Earth} < m_{123} < 500m_{Earth}$; $\Delta\lambda = 1^\circ$ for $30^\circ < \lambda < 38^\circ$.

- **Run 4** $\Delta m = 5m_{Earth}$ for $m_{Earth} < m_{13} < m_{Jupiter}$; $\Delta\lambda = 2^\circ$ for $0^\circ < \lambda < 60^\circ$ and $m_2 = m_{Jupiter}$.

The length of the integration was set to 10^3 years for **Run 1**, 10^4 years for **Run 2**, and 10^5 years for **Run 3**. Test computations up to 10^6 years have shown that an integration time of 10^5 years is an appropriate choice to reveal the 'fine' structure of the dynamical behaviour of the system in question, but shorter integration for only 10^4 years show already the main characteristics. **Run 4** was also undertaken for the moment for short time intervals of 10^3. As stability indicator we used the maximum libration angle which turned out to be very sensitive with respect to the stability of an orbit: $\lambda < 100^\circ$ was quite a good limit for stable orbits!

3 The Results for equally massive Trojan planets

In the respective Fig. 1 we show a stability diagram (results of **Run 1**) of the equilibrium points, where we used the libration width as stability measure. One can see that for all computed angular distances from L_4 (x-axis) and small masses up to the mass of Uranus the libration width stays within 100 degrees. It is surprising that even such large librations do not lead to instability. Then, for larger masses and larger initial distances to L_4, the configuration is unstable showing an interesting spike structure. The big unstable region without the spikes has an edge which could be approximated by a smooth curve, the cusps of the different spikes could also be approximated by a curve depending on the mass ratio and the angular distance from L_4. The small red strip on the border of stable and unstable region seems to show an abrupt change-over between stability and instability.

Fig. 2 (results of **Run 2**) has been done on a finer grid of initial conditions and for an extended integration time. The spike structure is confirmed, but in addition between these main spikes smaller ones (daughter spikes) seem to exist and the unstable regions extends far into the stable region.

To have a better picture of the spikes a third integration **Run 3**, again for an extended time (10^5 years), has been undertaken. On this fine scale it is visible that there are even more unstable spikes between the main ones. These spikes don't have a smooth edge, a phenomenon which is visible in all of them. On the contrary even in the unstable region sometimes tiny islands of stability arise.

Up to now we don't have an explanation for the interesting structure, but further computations on a fine grid (around stable islands in the unstable region and unstable regions in the stable spikes will clarify this situation.

4 Results with a 'central' Jupiter

For **Run 4** (Fig. 3) we gave the central Trojan planet the mass of Jupiter and changed the masses of the two neighbouring planets up to the mass of Jupiter. Because of the rough grid chosen for these computations the unstable fingers in the big stable zone are not well visible but they are present. It is interesting to note that there is no significant difference observable if one compares the respective results from Fig. 3 with the ones depicted in Fig. 1.

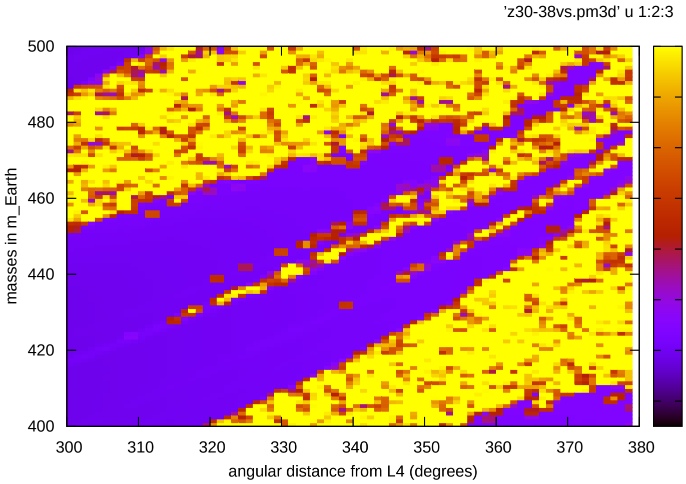

Figure 3: *Zoomed stability diagram for three equally massive Trojans; captions like in Fig. 1.*

5 Conclusions

In this working report we have shown our first results concerning the stability of three planets in a 1:1 MMR with respect to the angular distance from the equilibrium points. We started this investigation with a stability analysis of 3 equally massive planets (from 1 to 600 Earth masses) which move around a central body with 1 Solar mass in circular orbits; all three are exactly in a distance of 1 AU. We found a big stable region for masses up to 2 times Jupiter for small initial angular distance λ from the equilibrium point and vice versa for masses up to almost Saturn for large initial λ. The edge between stable and unstable region is not smooth but shows an interesting finger like structure which still needs to be explored in more detail. When the mass of the middle planet was kept constant (1 Jupiter mass) and only the outer two planets' masses were changed from low to high masses the structure seems to be quite similar to the equal mass studies. Next steps of research are to find the extension with respect to the semi-major axis and particularly how the stability changes when

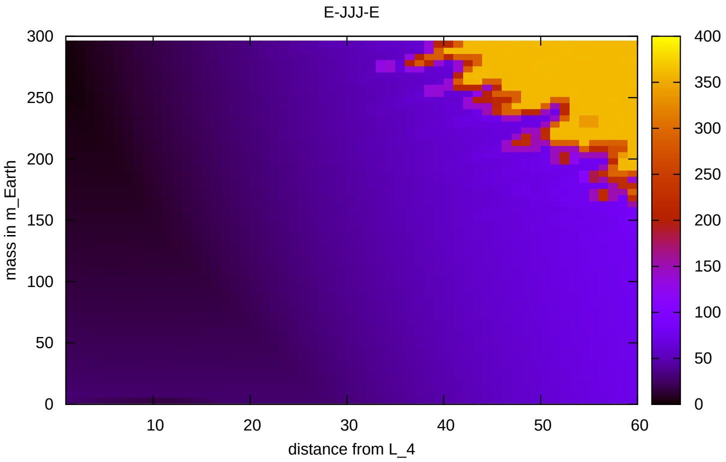

Figure 4: *Stability diagram for configuration with a fixed central mass ($m_2 = m_{\mathrm{Jupiter}}$); captions like in Fig. 1*

three different masses are in Three Trojan orbits.

Acknowledgement

The authors thank for the support through Austrian Science Foundation (FWF) project P18930-N16.

References

Beaugé, C., Sándor, Zs., Érdi, B., Süli, Á.: 2007, *A&A*, **463**, 359

Caton, D. B., Davis, S. A., Kluttz, K. A.: 2000, *AAS*, **32**, 1416

Chiang, E. I., Lithwick, Y.: 2005, *ApJ*, **628**, 520

Davis, S. A., Caton, D. B., Kluttz, K. A., Wohlman, K. D., Stamilio, R. J., Hix, K. B.: 2001, *AAS*, **33**, 1303

Dvorak, R., Pilat-Lohinger, E., Schwarz, R., Freistetter, F.: 2004, *A&A*, **426**, L37-40

Érdi, B., Sándor, Zs.: 2005, *CeMDA*, **92**, 113

Érdi, B., Nagy, I., Sándor, Zs., Süli, Á., Fröhlich, G.: 2007, *MNRAS*, **381**, 33

Ford, E. B., Gaudi, B. S.: 2006, *ApJ*, **652**, 137

Ford, E. B., Holman, M. J.: 2007, *ApJ*, **664**, 51

Freistetter, F.: 2006, *A&A*, **453**, 353-361

Hanslmeier, A., Dvorak, R.: 1984, *A&A*, **132**, 203

Laughlin, G., Chambers, J. E.: 2002, *AJ*, **124**, 592

Lichtenegger, H.: 1984, *Celestial Mechanics*, **34**, 357-368

Robutel, P., Gabern, F., Jorba, A.: 2005, *CeMDA*, **92**, 53-69

Salo, H., Yoder, C. F.: 1988, *Astron. Astrophys.*, **205**, 309-327

Schwarz, R., Gyergyovits, M., Dvorak, R.: 2004, *CeMDA*, **90**, 139-148

Schwarz, R., Süli, Á., Dvorak, R., Pilat-Lohinger, E.: 2009a, *CeMDA*, **104**, 69

Schwarz, R., Süli, Á., Dvorak, R.: 2009b, *MNRAS*, **398**, 2085

Smith, A. W., Lissauer, J. J.: 2009, *Icarus*, **201**, 381-394

PADEU
PADEU **20**, 23 (2011)
ISBN 963 463 557
© Published by the Astron. Dept. of the Eötvös Univ.

Third order resonances in the second fundamental mode of resonance

Bálint Érdi

Eötvös University, Department of Astronomy, H-1518 Budapest, Pf. 32, Hungary

E-mail: `B.Erdi@astro.elte.hu`

Abstract
Third order resonances are studied in the second fundamental mode of resonance. Comparisons are made with the 7:4 and 4:1 resonances of the restricted three-body problem. Librational solutions are computed by numerical integration of the equations of motion. The dependence of the amplitude of libration of the resonant angle variable on the semi-major axis and eccentricity is discussed.

Keywords: *models of resonances, phase portraits, restricted three-body problem, librational solutions*

1 Introduction

The first, basic model of resonance is the pendulum. The phase portrait of many resonances is analogous to that of the pendulum: there are two regimes of motion, libration and circulation, separated by a separatrix (Figure 1). In the center of libration there is a stable equilibrium point corresponding to the stable position of the pendulum, while the two branches of the separatrix connect two unstable equilibrium points corresponding to the unstable position of the pendulum.

In many problems of celestial mechanics, however, the phase portraits of resonances are more structured than that of a simple pendulum. To study these cases Henrard & Lemaitre (1983) introduced the second fundamental mode of resonance. This model is very useful for studying dissipative systems, for

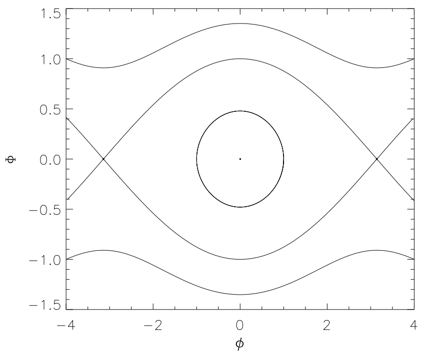

Figure 1: *The phase portrait of the pendulum.* Φ *and* ϕ *are action and angle variables.*

example tidally evolving satellites or migrating planets. Capture into resonance and passage through resonance can also be studied by using this model.

In a more general treatment (Murray & Dermott , 1999), it can be shown that in the case of a k-order inner resonance of the form $j:(j-k)$ between two bodies of masses m and m' orbiting a central body of mass m_c, the dominant part of the Hamiltonian, reduced to one degree of freedom, is

$$H = \alpha J + \beta J^2 + \varepsilon (2J)^{k/2} \cos k\theta, \tag{1}$$

where

$$\alpha = \frac{(j-k)n - jn' - k\dot{\varpi}}{k}, \quad \beta = \frac{3}{2k^2}\left[\frac{(j-k)^2}{ma^2} + \frac{j^2}{m'a'^{\,2}}\right],$$

$$\varepsilon = f_d\,(n^2)^{1-\frac{k}{4}}\,\frac{a^{3-k}}{a'}\,\frac{m'}{m_c}m^{1-\frac{k}{2}},$$

$$J = \sqrt{\mu a}\,(1 - \sqrt{1-e^2}), \quad k\,\theta = j\lambda' + (k-j)\lambda - k\varpi.$$

Here a, n, e, λ, ϖ are the semi-major axis, mean motion, eccentricity, mean orbital longitude, and longitude of the pericenter of the inner body with mass m. The orbital elements of the outer body with mass m' are denoted by prime. In the expression of ε, f_d depends on a/a' through the Laplace coefficients and its derivatives. In the present one-degree of freedom problem f_d is considered as constant. The action variable J (where $\mu = G(m_c + m)$ and G is the constant of gravity) is proportional to e^2. The angle variable θ describes the conjunctions ($\lambda' = \lambda$) of the two revolving bodies by giving the mean anomaly ($M = \lambda - \varpi$) of the location of such occasions.

The Hamiltonian (1) depends on several parameters. These can be comprised into a single parameter through a proper scaling transformation:

$$\Phi = \frac{J}{\eta}, \quad \phi = \theta + \pi \text{ (for } k \text{ even), or } \phi = \theta \text{ (for } k \text{ odd)}, \quad \tau = \beta\eta\,\mathrm{t}, \tag{2}$$

where

$$\eta = \left[\frac{(-1)^k\, 2\beta}{\varepsilon}\right]^{\frac{2}{k-4}},$$

and τ is the new independent variable instead of the time t in the Hamiltonian canonical equations. This transformation results in the Hamiltonian

$$H = \delta\Phi + \Phi^2 + (-1)^k 2(2\Phi)^{\frac{k}{2}} \cos k\phi \tag{3}$$

with one parameter

$$\delta = \alpha \left[\frac{4}{\varepsilon^2 \beta^{(2-k)}}\right]^{\frac{1}{4-k}}.$$

The Hamiltonian (3) was thoroughly studied for $k = 1$ and 2 (Henrard & Lemaitre , 1983; Murray & Dermott , 1999). The case $k = 3$ is also discussed in (Murray & Dermott , 1999). Here some additional considerations are given for $k = 3$ and comparisons with third order resonances of the restricted three-body problem are also made.

2 Third order resonances

For $k = 3$, Equation (3) reduces to

$$H = \delta\Phi + \Phi^2 - 2(2\Phi)^{\frac{3}{2}} \cos 3\phi \tag{4}$$

with

$$\delta = \frac{4\alpha\beta}{\varepsilon^2}.$$

Introducing the variables

$$x = \sqrt{2\Phi}\cos\phi, \quad y = \sqrt{2\Phi}\sin\phi, \tag{5}$$

the Hamiltonian (4) takes the form:

$$H = \frac{1}{2}\delta(x^2 + y^2) + \frac{1}{4}(x^2 + y^2)^2 - 2(x^3 - 3xy^2). \tag{6}$$

Curves of constant Hamiltonian are shown in Figure 2 for several characteristic values of δ. For $\delta > 9$ there is one stable equilibrium point at the origin. At $\delta = 9$ three bifurcation points occur. For $9 > \delta > 0$ there exist three pairs of stable and unstable equilibrium points, beside the stable origin. The unstable equilibrium points reach the origin at $\delta = 0$ that becomes unstable for this value of δ. For $\delta < 0$ there appear again three unstable points, beside the stable origin and the other three stable equilibrium points. Note the $2\pi/3$ rotational symmetry of the figures.

Curves of constant Hamiltonian of (4) are shown in Figure 3 for the same values of δ as in Figure 2. It can be seen that, in accordance with Figure 2, libration of ϕ is possible around three values (0, $2\pi/3$, $4\pi/3$) for $\delta < 9$.

3 Applications

The equations of motion of the restricted three-body problem were integrated for initial conditions near the 7:4 and 4:1 resonances to make comparisons with the model described in the previous section. The mass parameter was 0.001, corresponding approximately to a Sun-Jupiter-asteroid system.

In the case of the 7:4 resonance, Figure 4 shows a series of librational solutions for the initial values $a = 0.692$, $e = 0.17 - 0.34$ (the resonant value of a is 0.688612 in the unit of the semi-major axis of the outer body). These were obtained by computing the resonant angle variable $\phi = \theta = 7\lambda' - 3\lambda - 4\varpi$ from the results of the numerical integration and by making use of the result of Murray & Dermott (1999) that $\sqrt{2\Phi} = 2003.0\,e$ in Equation (5). A comparison with Figure 2 reveals that for a given librational curve the eccentricity does not change as much in Figure 4 as in Figure 2. Also, the amplitude of libration of the variable ϕ does not change much in Figure 4. This is also shown in Figure 5 for the smallest (0.017) and the largest (0.34) values of the initial eccentricity for which the librational solutions were computed. In contrary, Figures 2 and 3 allow large variation in the amplitude of libration of ϕ from one librational curve to the other. The numerical integrations show that for the 7:4 resonance librational solutions exist above the resonant value of a in a narrow interval of the semi-major axis, and in this interval for a given value of a in a narrow region of the eccentricity.

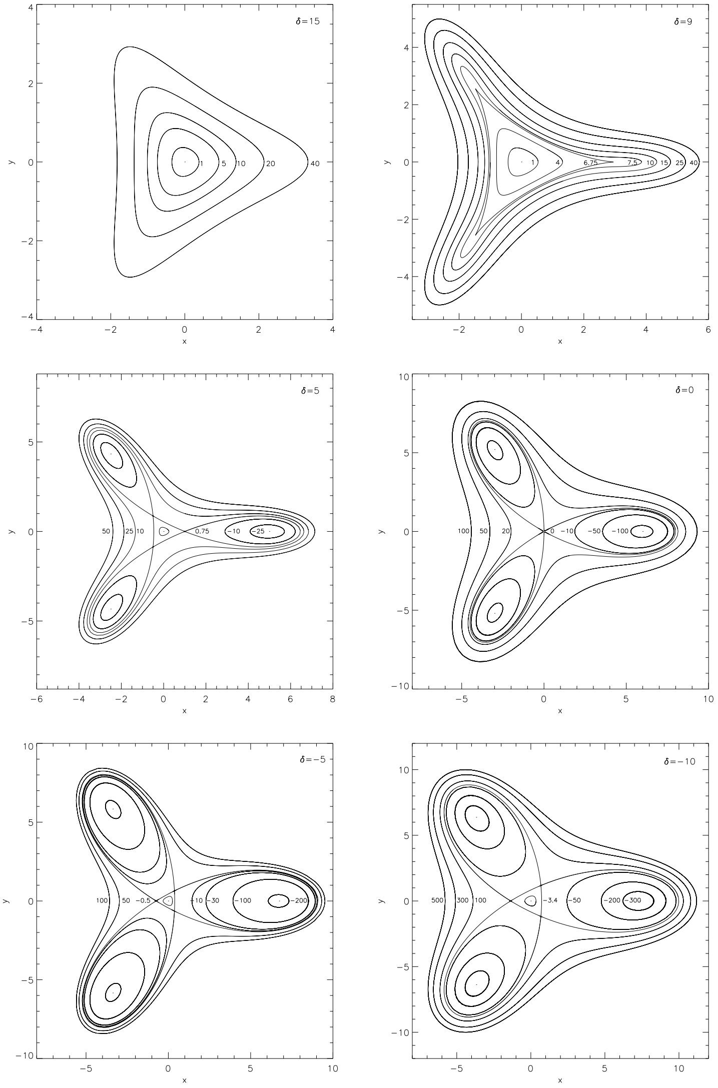

Figure 2: *Curves of constant Hamiltonian of third order resonances in the x, y plane for several characteristic values of δ (the values of H are given beside the curves).*

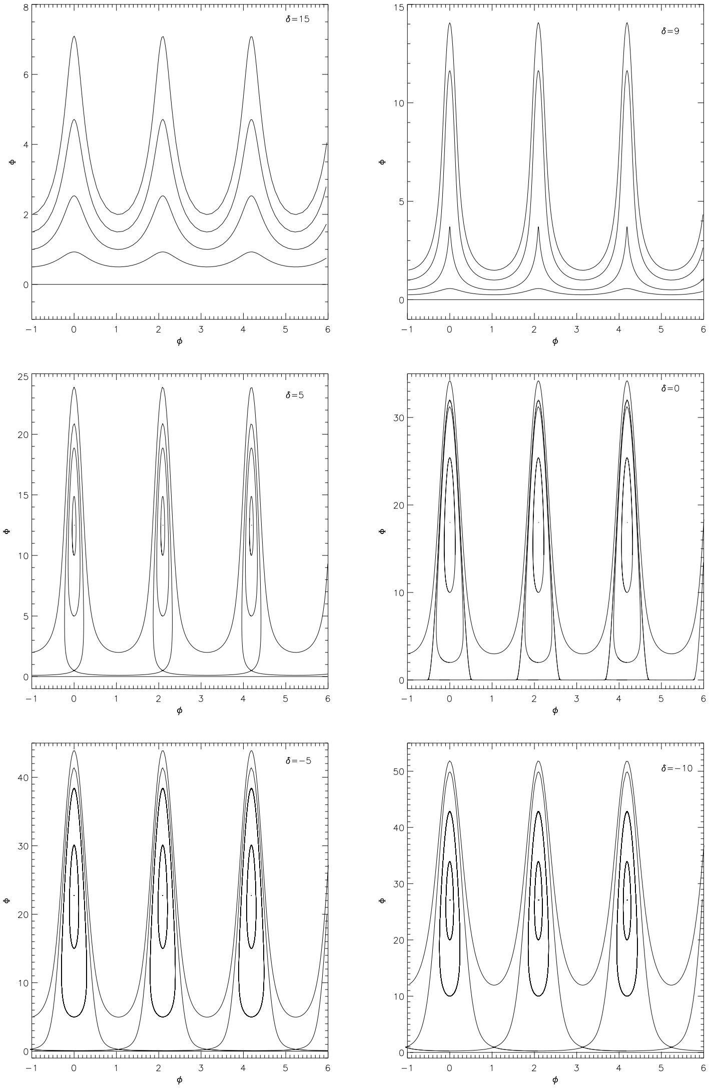

Figure 3: *Curves of constant Hamiltonian of third order resonances in the Φ, ϕ plane. (The values of H are different from those in Figure 2).*

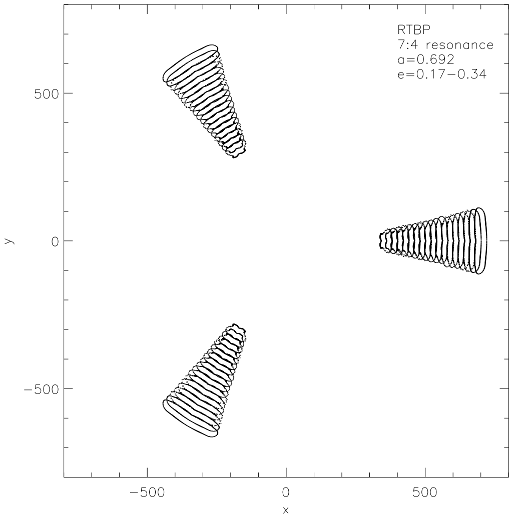

Figure 4: *Librational solutions in the case of the 7:4 resonance in the restricted three-body problem (the eccentricity is increasing from the centre outwards).*

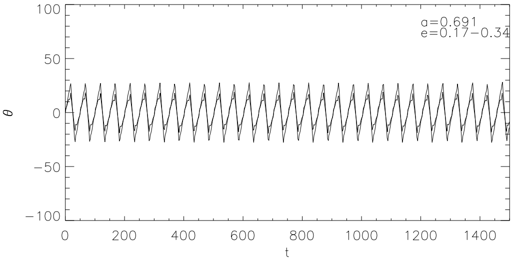

Figure 5: *Libration of the resonant angle variable* $\phi = \theta = 7\lambda' - 3\lambda - 4\varpi$ *for* $e = 0.17$ *(inner curve) and for* $e = 0.34$ *(outer curve).*

In the case of the 4:1 resonance, the resonant angle variable $\phi = \theta = 4\lambda' - \lambda - 3\varpi$ librates for initial semi-major axes belonging to a very narrow interval $0.393 < a < 0.400$ around the resonant value $a = 0.396851$. At the resonant

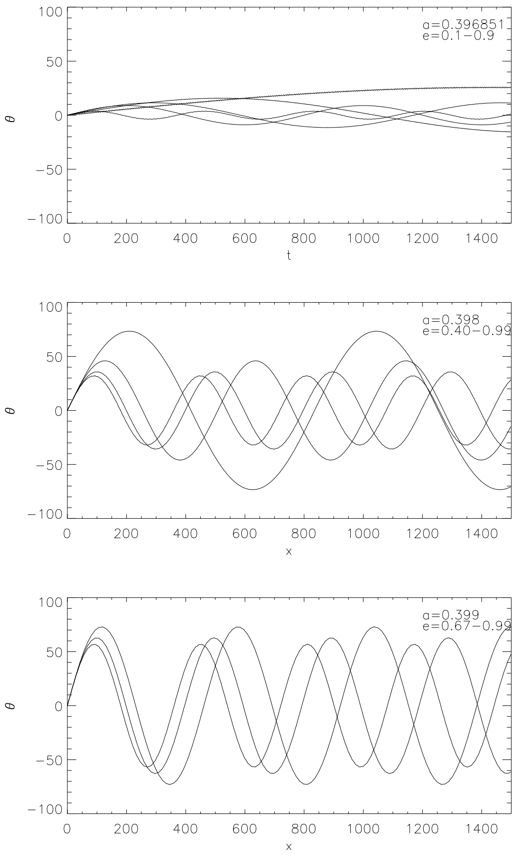

Figure 6: *Libration of the resonant angle variable* $\phi = \theta = 4\lambda' - \lambda - 3\varpi$*. Upper panel:* $a = 0.396851$*,* $e = 0.1, 0.2, 0.3, 0.4, 0.9$ *(to smaller eccentricities there correspond larger amplitudes). Middle panel:* $a = 0.398$*,* $e = 0.4, 0.6, 0.8, 0.99$*. Bottom panel:* $a = 0.399$*,* $e = 0.67, 0.80, 0.99$*.*

value of a, θ librates for all initial e between $0 \leq e < 1$, for smaller values of e with larger amplitudes. This is shown in the upper panel of Figure 6 for $e = 0.1 - 0.9$. Above the resonant value of a, libration of θ is possible above a lower limit of e, which increases as a gets larger. This is shown in the middle and bottom panels of Figure 6. For $a = 0.398$, the lower limit of e is 0.40 (middle panel), while for $a = 0.399$ this limit is $e = 0.67$ (bottom panel). At a given a, the amplitude of θ decreases as e increases. Similar features occur below the resonant value of a.

4 Conclusions

The model of the second fundamental mode of resonance describes well the qualitative behaviour of third order resonances. Quantitative differences, however, occur regarding the amplitudes of variation of the eccentricity and the resonant angle of third order resonances in the circular restricted three-body problem.

Libration of the resonant angle is possible in a very narrow interval around the resonant value of the semi-major axis, for a limited range of the eccentricity, depending on the semi-major axis. The lower border of the eccentricity range increases with the increase of the semi-major axis. This indicates, that in the model of the restricted three-body problem capture into a third order (for example 4:1) resonance is very difficult since the semi-major axis must be very close to the resonant value and even then the eccentricity must be above a lower limit.

Acknowledgement

The European Union and the European Social Fund have provided financial support to the project under the grant agreement no. TÁMOP-4.2.1/B-09/1/KMR-2010-0003.

References

Henrard J., Lemaitre A. 1983, Celestial Mechanics, 30, 197

Murray C., Dermott S. *Solar System Dynamics.* Cambridge University Press (1999)

PADEU PADEU **20**, 33 (2011)
ISBN 963 463 557
© Published by the Astron. Dept. of the Eötvös Univ.

THE USE OF MAPPING METHODS FOR SYSTEMS IN MEAN MOTION RESONANCES

Veresa Eybl

Institute for Astronomy, Universität Wien, Türkenschanzstr. 17, A-1180 Wien, Austria

E-mail: `vera.theresa.eybl@univie.ac.at`

Abstract
A symplectic mapping approach is used for the dynamical investigation of systems in mean motion resonances. In this work, the mapping approach by Hadjidemetriou is applied to the case of the planar elliptic restricted three-body problem. The construction of the equations for the mapping is described and results for the 5:3 mean motion resonance with Earth and the 3:1 mean motion resonance with Jupiter are presented.
Keywords: *mappings, mean motion resonances, solar system*

1 Introduction

Mean motion resonances (MMR) play an important role in the dynamics and stability of planetary systems. A MMR is an orbital resonance of the type $p : p + q$, where q is the order of the resonance. In the solar system the MMRs with Jupiter are especially important as they shape the distribution of bodies in the asteroid belt. The motion of an asteroid or a similarly small body moving in the gravitational field of a central body and a planet can be represented in a very good approximation by the restricted three-body problem (R3BP).

2 The restricted three-body problem

The R3BP describes a system of two massive bodies – primary and secondary – and a third massless body. It cannot be solved analytically, but it is possible to find a representation in the form of a nearly integrable Hamiltonian system. The equations of motion of the third body (or test particle) consist of an unperturbed Keplerian part due to gravitational attraction of the central body, and a perturbed part due to the influence of the secondary. The Hamiltonian formalism lets us write for the motion of the massless body $H = H_0 + \mu H_1$, where H_0 is the integrable Keplerian part and H_1 is the non-integrable part due to a small perturbation μ. The elliptic restricted three-body problem (ER3BP) can be reduced to a form similar to the circular restricted three-body problem using a non-uniformly rotating and pulsating frame of reference. In the planar ER3BP the mutual distance between the primaries is fixed to be unity and the plane of reference is set to the orbital plane of the primaries. Thus the system can be described by a form where the positions of the primaries are fixed and the motion of the third - perturbed - body is relative to the positions of the primaries. The main difference to the circular R3BP is however, that the Hamiltonian is time-dependent.

3 Construction of the mapping

Hadjidemetriou (1991) proposed a mapping method which has been used by several authors Ferraz-Mello (1996); Efthymiopoulos & Sándor (2005); Lhotka et al. (2008); Lhotka (2009) for the study of the dynamics of MMRs. The mapping transforms the continuous flow of the Hamiltonian into discrete steps while preserving the symplectic structure of phase space. Investigating the motion in the reduced phase space of the mapping makes it possible to understand the motion in the original phase space of the Hamiltonian. In this section the construction of a symplectic mapping for the planar ER3BP is shown. The planar ER3BP has two degrees of freedom, making up a 4-dimensional phase space. Choosing a constant energy for the Hamiltonian H, one momentum can be expressed by the other canonical variables and therefore 4D phase space can be reduced to a three-dimensional subspace.The analysis of the motion in the 3D-subspace makes it possible to deduce the geometry of the original 4-dimensional phase space.

3.1 The disturbing function

The disturbing function in terms of the mutual distances of the bodies can be written as

$$R(r,r') = \frac{1}{\Delta} - \frac{1}{r} + \frac{1}{2}\frac{\Delta^2}{r'^3} - \frac{1}{2}\frac{r^2}{r'^3} \tag{1}$$

where the mutual distance between the secondary and the perturbing body $\Delta = r' - r$, r' is the distance of the secondary from the primary and r the distance of the perturbed body from the primary. Primed variables always refer to the perturber, while unprimed variables refer to the perturbed body. The relations given for the primed quantities are also valid for the unprimed ones, respectively, and vice versa. The distance r in terms of Keplerian elements is given by $r = a(1 - e\cos E)$. The eccentric anomaly can be expressed as $M = E - e\sin E$. Using these relations we can write

$$\frac{\mathrm{d}E}{\mathrm{d}M} = \frac{1}{1 - e\cos E} = \frac{a}{r}, \;\; \frac{a}{r} = 1 + 2\sum_{s=1}^{\infty} J_s(se)\cos(sM) \tag{2}$$

The mean anomaly M can be written as $\lambda = M - \omega$. Using series expansions of Eq. 2 the disturbing function can be expressed in terms of Keplerian elements as $R(a, e, a', e', \lambda, \lambda', \omega, \omega')$.

Introducing new canonical variables To simplify some terms of the disturbing function all a' are set to, corresponding to a scaled distance of the secondary of 1. The e' are replaced with the numerical value of the respective eccentricity of the planet one wants to study. Further, ω' can be set to zero, corresponding to an arbitrary choice of the coordinate system in the planar ER3BP. The disturbing function $R(a, e, \lambda, \lambda', \omega)$ is then expressed in modified Delaunay variables following the method described by Tsiganis (2007). The canonical transformation is given by

$$\lambda = \lambda, \;\; \Lambda = \sqrt{\mu' a}, \;\; \gamma = -\omega, \;\; \Gamma = \sqrt{\mu' a}\left(1 - \sqrt{1 - e^2}\right) \tag{3}$$

where the normalized mass of the secondary perturbing body is $\mu' = \frac{m'}{m' + M_*}$, where m' denotes the mass of the secondary and M_* the mass of the primary.

Expansion around the resonance Since we are interested in the behaviour of the system in the MMR, the disturbing function for the investigated MMR has to be studied. The variable of the semi-major axis a in the disturbing function is therefore replaced by the value of a at the exact location of the resonance

$$a_{\mathrm{res}} = a' \left(\frac{p}{p+q} \right)^{2/3} (1-\mu)^{1/3}. \tag{4}$$

Again following Tsiganis (2007), resonant canonical variables are introduced.

$$\psi = p\lambda - (p+q)\,\lambda',\ \ \Lambda = p\Psi,\ \ \phi = \gamma,\ \ \Gamma = \Phi \tag{5}$$

Using Eq. 5 we get a disturbing function $R(\psi, \psi', \Psi, \phi, \Phi)$, where we can introduce the new momentum $J = \Psi - \Psi_{\mathrm{res}}$, where Ψ_{res} is the resonant angle $\Psi_{\mathrm{res}} = \frac{1}{p}\sqrt{\mu a_{\mathrm{res}}}$. The resulting disturbing function is of the form $R(\phi, \Phi, \psi, \psi', J)$.

3.2 The symplectic mapping approach of Hadjidemetriou

The method of Hadjidemetriou (1991) allows the construction of a symplectic mapping model from the continuous flow. The Hamiltonian is averaged with respect to the short periodic terms of the perturbation to construct a mapping preserving the structure of phase space. This is done by using the averaged Hamiltonian as the generating function for the mapping equations. In this section the averaging process and construction of the mapping is described.

Averaging the Disturbing Function To cancel out terms of the disturbing function not associated with the MMR, R is averaged over the secular terms of the motion of the disturbing body (the planet, in this case). This is done by integrating $\psi' = \lambda'$ over the period of the planet, so that

$$R(\phi, \Phi, \psi, \psi', J) \rightarrow \bar{R}(\phi, \Phi, \psi, J). \tag{6}$$

Constructing the averaged Hamiltonian The Hamiltonian function the mapping is based on is constructed of a undisturbed, Keplerian part H_0 and a disturbing part H_1 containing the averaged disturbing function $\bar{R}$ (Eq. 6).

$$H = H_0 - \mu\bar{R},\ \ H_0 = -\frac{{\mu'}^2}{2p\Psi^2} - n'(p+q)\Psi \tag{7}$$

Introducing semi-Cartesian coordinates The action-and-angle variables are converted into semi-Cartesian coordinates using the following coordinate transformation

$$\cos\phi = \frac{x}{\sqrt{2\,\Phi}},\ \ \sin\phi = \frac{y}{\sqrt{2\,\Phi}},\ \ \Phi = \frac{x^2+y^2}{2} \tag{8}$$

The resulting Hamiltonian $H(x, y, \psi, J)$ is not necessarily centered in the origin of the coordinate system, which would lead to distorted results. So, if necessary, another transformation ($x \to X$, $y \to Y$) has to be applied to translate the coordinate system accordingly. The centered Hamiltonian $H(X, Y, \psi, J)$ can now be used to construct the mapping.

The generating function Following the method described by Hadjidemetriou (1991); Tsiganis (2007); Hadjidemetriou (1993), the mapping is constructed by means of a generating function W, which is defined as

$$W = W_0 + 2\,\pi\bar{H},\ \ W_0 = J\psi + XY. \tag{9}$$

The generating function is then used to calculate the mapping equations

$$\frac{\partial W}{\partial J_{n+1}} = \psi_{n+1},\ \ \frac{\partial W}{\partial \psi_n} = J_n,\ \ \frac{\partial W}{\partial Y_{n+1}} = X_{n+1},\ \ \frac{\partial W}{\partial X_n} = Y_n \tag{10}$$

which describe an implicit mapping. The Eq. 10 have to be solved for the $(X_{n+1}, Y_{n+1}, \psi_{n+1}, J_{n+1})$ to get the explicit mapping equations, which can then be applied iteratively for each point in 4-dimensional phase space. Each step in the mapping from $(X_n, Y_n, \psi_n, J_n) \to (X_{n+1}, Y_{n+1}, \psi_{n+1}, J_{n+1})$ then represents one orbit of the secondary. The successive $(X_{n+1}, Y_{n+1}, \psi_{n+1}, J_{n+1})$ form the trajectory of a point in four-dimensional phase space.

3.3 Surface Of Section

To represent the four-dimensional phase space on a two-dimensional surface, a Poincaré surface of section (S.o.S.) has to be found (Poincaré , 1892). The choice of criteria for the S.o.S. is not trivial. In this work a criterion proposed by Tsiganis (2007) has been used:

$$\psi - \widetilde{Q} = \pi. \tag{11}$$

It can be found writing the Hamiltonian in the form

$$H = \frac{1}{2}\beta J^2 - \mu' d\Phi - \mu' \widetilde{D}(\phi,\Phi)\cos(\psi - \widetilde{Q}(\phi,\Phi)) \tag{12}$$

where

$$\widetilde{D} = \sqrt{A^2+B^2},\ \ \widetilde{Q} = 2\ \arctan\left(\frac{\sqrt{A^2+B^2}-A}{B}\right) \tag{13}$$

$$A = \sum D\ \cos(k\phi),\ \ B = \sum D\ \sin(k\phi). \tag{14}$$

Applying this criterion to the points of the trajectory in 4D phase space eliminates the ψ coordinate and gives a trajectory in 3D phase space. A second criterion,

$$J > 0 \tag{15}$$

has to be considered to reduce the phase space to two dimensions and make it possible to plot a 2D graphical representation of the trajectory.

4 Application to resonant motion in the solar system

Several authors have investigated resonant motion using mapping methods see e.g. Hadjidemetriou (1993); Dvorak (2008); Lhotka et al. (2008); Bazsó et al. (2010). The described mapping method was applied to the 3:1 MMR with Jupiter and the 5:3 MMR with Earth.

4.1 The 3:1 MMR with Jupiter

The 3:1 MMR with Jupiter is an unstable resonance, and the origin of the Alinda family of asteroids. Since the 3:1 MMR is a resonance of the second order ($q = 2$), the location of the resonance is calculated as

$$a_{3:1} = a'\left(\frac{p}{p+q}\right)^{2/3}(1-\mu)^{1/3} = 0.48 \tag{16}$$

which is scaled to the location of the secondary and corresponds to a semi-major axis of 2.50 AU. An overview of the input parameters used in the application of the mapping model to this resonance can be found in Table 1.

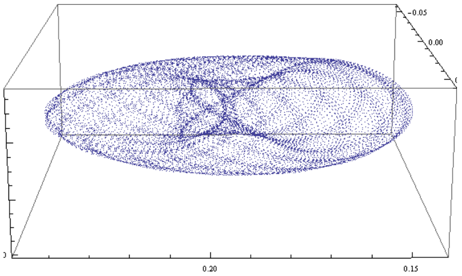

Figure 1: *Projection of a 4-dimensional trajectory onto the X-Y-ψ coordinates (the ψ-coordinate is on the z-axis of the plot).*

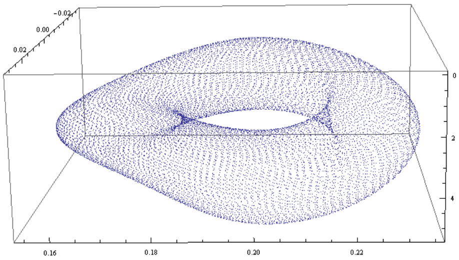

Figure 2: *Projection of another trajectory in the 3:1 MMR with Jupiter.*

The phase space portraits were created by iterating a grid of initial conditions with starting values along the X-axis for 300 000 steps. In Fig. 1(a) and 1(b) two trajectories in 4-dimensional phase space are projected into 3D. Fig. 3(a) shows the trajectory from Fig. 1(a), projected into two dimensions, with the points lying on the first surface of section condition (Eq. 11) plotted in brown (see online version for color figures). For stable orbits, the trajectory of one point in phase space describes an invariable curve. In Fig. 3(a) there are two invariable curves, which are reduced to one applying the second criterion from Eq. 15. This last step then gives the S.o.S. in the X-Y-plane, as described in Eq. 8. Fig. 3(b) shows an unstable trajectory with the corresponding points on the S.o.S. The points on the surface of section are scattered and do not describe an invariable curve. The phase space portrait of the 3:1 MMR with Jupiter with an initial grid of trajectories can be seen in Fig. 5(a). Only the points lying on the surface of section defined by Eq. 11 and 15 are visible. The different trajectories are color-coded. There are two fixed points, one elliptic (left) and one hyperbolic (right), due to the 3:1 MMR being a second order resonance. Around the fixed points regular (stable) motion is possible. Chaotic motion can be seen on the left of Fig. 5(a) at the tips of the crescent-shaped curve.

As expected for a second order resonance, there are two fixed points around which regular orbits can exist.

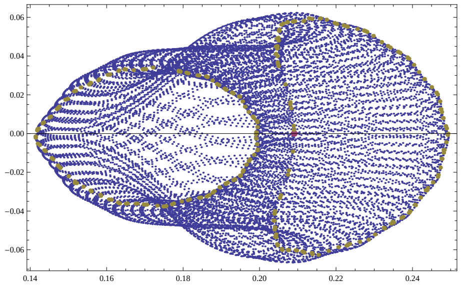

Figure 3: *Projection of the trajectory from Fig. 1(a) onto the X-Y-plane. Points on the S.o.S. are shown as larger brown points, starting point is shown in purple (see online version for color figures).*

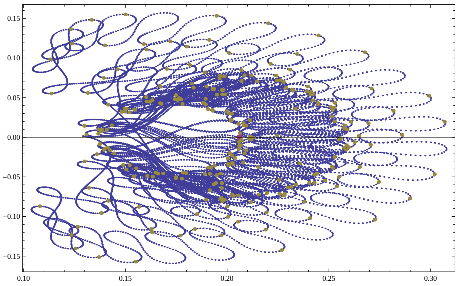

Figure 4: *Projection of a chaotic trajectory onto the X-Y-plane.*

Table 1: *Input parameters for Jupiter.*

semi-major axis a (scaled)	1
semi-major axis a	5.21 AU
eccentricity e	0.048
mass μ'	9.54×10^{-4}
a_{res} (scaled)	0.48
a_{res}	2.5 AU

Table 2: *Input parameters for Earth.*

semi-major axis a	1 AU
eccentricity e	0.0167
mass μ'	3.0045×10^{-6}
a_{res}	0.71 AU

4.2 The 5:3 MMR with Earth

The 5:3 MMR was chosen because of the proximity of the current locations of Earth and Venus to this resonance. Earth and Venus are located very close to the 13:8 MMR, placing them right between the 5:3 and 8:5 MMR (Bazsó et al. , 2010). The 5:3 MMR is also a second order resonance, so $p = 3$ and $q = 2$. The location of the resonance is at

$$a_{5:3} = a' \left(\frac{p}{p+q} \right)^{2/3} (1-\mu)^{1/3} = 0.71. \tag{17}$$

Since Earth already has a semi-major axis of 1, scaling is not necessary and the location of the resonance is at an orbital distance of 0.711 AU. The input

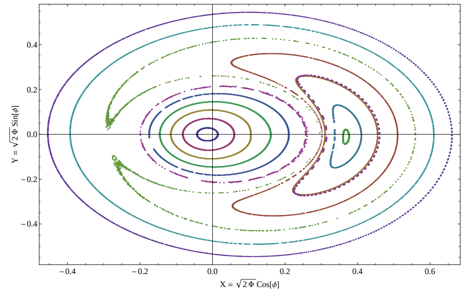

Figure 5: *Phase space portrait of the 3:1 MMR with Jupiter.*

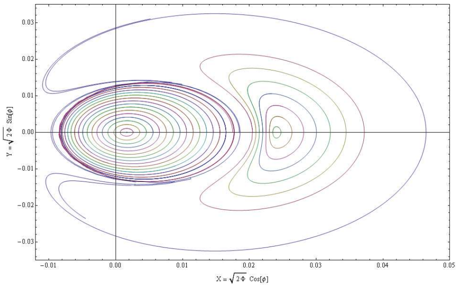

Figure 6: *Phase space portrait of the 5:3 MMR with Earth.*

parameters used for the calculation of the Hamiltonian are shown in Table 2.

Fig. 5(b) shows the phase space portrait of the 5:3 MMR with Earth. As in the 3:1 resonance, there are two fixed points surrounded by stable regions. Stable regions of the phase space are represented as invariable curves, whereas chaotic regions are represented by changing trajectories, as can be seen in the outermost curve.

5 Conclusions

The Hadjidemetriou mapping model is a useful tool for the study of low order MMRs. It was successfully applied to second order resonances in the solar system, like the 3:1 MMR with Jupiter and the 5:3 MMR with Earth. However, more work needs to be done on higher order resonances.

Acknowledgement

The author wants like to acknowledge the support from the Austrian FWF project 18930-N16.

References

Hadjidemetriou, J. D. (1991) *Mapping models for Hamiltonian systems with application to resonant asteroid motion*, Predictability, Stability, and Chaos in N-Body

Dynamical Systems, 157–175.

Ferraz-Mello, S. (1996), CeMDA, 53, 421

Efthymiopoulos, C. and Sándor, Z. 2005, MNRAS, 364, 253

Lhotka, C., Efthymiopoulos, C. and Dvorak, R. 2008, MNRAS, 384, 1165

Lhotka, C. 2009, CeMDA, 104, 175

Tsiganis, K. 2007, Lecture Notes in Physics, Berlin Springer Verlag, 729, 111.

Hadjidemetriou, J. D. 1993, CeMDA, 56, 536

Poincaré, H. (1892) *Les methodes nouvelles de la mecanique celeste*, Gauthier-Villars et fils Paris.

Dvorak, R. and Lhotka, C. and Schwarz, R. 2008, CeMDA, 102, 97

Bazsó, Á., Dvorak, R., Pilat-Lohinger, E., Eybl, V. and Lhotka, C. 2010, CeMDA, 107, 63

PADEU | PADEU **20**, 43 (2011)
ISBN 963 463 557
© Published by the Astron. Dept. of the Eötvös Univ.

LIGHT CURVES AND COLORS OF THE CENTAURUS 2060 CHIRON (1977 UB) AND 10199 CHARIKLO (1997 CU_{26})

Mattia Galiazzo[1], **Giovanni Carraro**[2], **Michele Maris**[3],
Carlos de la Fuente Marcos[4], **Raul de la Fuente Marcos**[5],
Marco Montalto[6]

[1] Institute for Astronomy, University of Vienna, Türkenschanzstraße 17, A-1180 Vienna, Austria
[2] European Southern Observatory, Alonso de Cordova 3107, Vitacura Santiago, Chile
[3] Osservatorio Astronomico di Trieste, via G.B. Tiepolo 11, I-34131 Trieste, Italy
[4,5] Suffolk University Madrid Campus, Vina 3, E-28003 Madrid, Spain
[6] University Observatory Munich, Scheinerstrasse 1, D-81679 Munich, Germany

E-mail: `mattia.galiazzo@univie.ac.at`

Abstract

Chariklo and Chiron are two minor bodies classified as Centaurs but with somehow slightly different properties. The first one is the largest known Centaur but its rotational period is still unknown, the second one is a periodic comet characterized by rapid changes in magnitude. Here we study their light curves in order to obtain the rotational periods and their photometrical properties. Our main results are: (i) Chariklo exhibits a statistically significant variability of 0.138 ± 0.036; (ii) for Chiron a variability of 0.154 ± 0.056 is found; (iii) our data suggest a rotational period for Chariklo of about 3.5 hours.

Keywords: *Chariklo – Chiron – Photometry – minor bodies: Centaurs – periodic comet*

1 Introduction

Centaurs are an unstable dynamical class of minor bodies which orbit around the Sun between the orbits of Jupiter and Neptune. They are characterized by very short dynamical lives, $\sim 10^6 - 10^7$ years. The largest one known so far is Chariklo, with a size ranging from $256.8\pm^{13.2}_{12.8}$ km for $p_V = 5.81\pm^{0.62}_{0.55}$ to $260.9\pm^{16.4}_{16.0}$ km for $p_V * 5.63\pm^{0.76}_{0.65}$ (Stansberry et al. 2008). The early spectroscopic study by Brown et al. (1998) revealed that Chariklo's spectrum is characterised by a strong absorption around 2.05 μm, associated with the 2.03 μm water absorption band. More recently, Dotto et al. (2003) suggested the presence on its surface of a mixture of tholins, amorphous carbon and water ice in diverse percentage. Infrared studies confirmed the presence of water ice. This together with chemical inhomogeneities can affect the determination of the size of the object. Besides, this ice could emit gas, making difficult to measure the real albedo. Chariklo has been studied several times aiming at measuring its physical properties and, in particular, its rotational period, for which so far no agreement has been found, it has been traditionally difficult to determine it, because of the very small amplitude variation detected in the lightcurve. This suggests either long period or one close to 24 hours (Davies et al. 1998; McBride et al. 1999). Peixinho et al. (2001) claimed that it can be due to its almost spherical shape without significant albedo variations on the surface or also that its pole was facing the sun during previous observations.

Here we provide new observational material in an attempt to better constrain Chariklo's rotational period. The material presented here consists of multicolor photometry obtained in the winter of 2006, when the object was visible in the Hydra constellation.

Together with Chariklo and during the same observing run we have also followed the prototype of the Centaur class, Chiron, which is a very peculiar object. In fact it exhibits a dual existence, passing from total inactivity to a significant cometary activity, and becoming this way one of the most massive comets in the Solar System. Its orbit is chaotic, significantly more than that of Chariklo. His path drastically changes every few decades when passing close to the giant planets, its orbit becoming unstable and unpredictable. The detection of a strong magnitude change between 1988 and 1989, when Chiron was at 11 astronomical units (AU), was accompanied by the presence of a cometary coma close to the perihelion, where activity is supposed to be caused by the sublimation of the carbon monoxide. Its size (the nucleus) as estimated by Stansberry et al. (2008) is $233\pm^{14.7}_{14.4}$ km for $p_V = 7.57\pm^{1.03}_{0.87}$. Chiron therefore is more reflective than Chariklo. As in the case of Chariklo, Luu & Jewitt (1990) reported the presence of water ice on the absorption lines around 2.0 μm. Its low albedo was confirmed by Hartmann (1982), who found that Chiron has dark chondritic-carbonaceous material and/or dirty ices like the asteroids of type C. Luu & Jewitt (1990) suggested that the strong cometary activity was driven by isolated explosive emissions of CO_2 and other gases. During a period of activity, Chiron can exhibit a coma of 20000 km (Silva & Cellone 2001); the presence of the coma does not always coincide with Chiron's maximum luminosity. These bursts of activity are however not yet completely understood.

2 Chariklo

Figure 1: *Chariklo' position on the first (left panel) and last night (right panel). The area is 6.49 × 9.01 arcmin^2. North is up, east to the left. The arrow indicates Chariklo' motion over the whole run.*

Chariklo was observed in the Hydra constellation on the nights of 2006 June 27 to 29, from JD 2453914.6153 to JD 2453916.7772. During the time we monitored it, Chariklo moved by 267.2 arcsec, as shown in Fig. 1.

Observations were performed at the Las Campanas Observatory, using the 1.0-m Swope telescope equipped with the Site#3 2048 × 3150 CCD camera. The field of view is about $14'8 \times 22'8$ with a pixel scale of 0.435 arcsec/pixel. Chariklo observations were acquired during a 5 nights run, 3 of which were photometric. Preliminary processing of the CCD frames was completed using standard routines in the IRAF package. Both dome and sky flat-field frames were obtained in each filter, and the images were also corrected for linearity

(Hamuy et al. 2006; Carraro 2009). The average seeing was $1''20$ along the entire 5 nights run (26 to 30 June, 2006). However, out of the 5 nights, only 3 (26, 28 and 30 June 2006) were photometric. In each of the photometric night we observed 96 standard stars using an aperture of 14 pixels, from repeated observations of the three fields Mark A, PG 1657, PG 2213 and SA 110 (Landolt 1992) at different air masses.

The following relations between the instrumental (lower case letters) and the standard colours and magnitudes were adopted, as derived merging together standard stars from the three different photometric nights, after checking that they were stable:

$$V = 22.115(0.004) + v - 0.068(0.007) \times (B - V) + 0.16(0.02) \times X \quad (1)$$

$$B = 22.084(0.004) + b + 0.054(0.007) \times (B - V) + 0.30(0.02) \times X \quad (2)$$

$$I = 22.179(0.006) + i + 0.058(0.009) \times (V - I) + 0.06(0.02) \times X \quad (3)$$

(X =airmass). Second order color terms have also been computed, but they turned out to be negligible. Aperture photometry of standard stars was obtained with an aperture radius of $6'69$ arcsec (14 pix).

We collected a grand total of 24 frames, as highlighted in Table 1, 20 in R, 3 in V and 1 in I. The instrumental photometry of Chariklo and several field stars was extracted with the DAOPHOTII (Stetson 1987) package, using a fitting radius of 5 pixels. We use 5 stable field stars as reference to shift Chariklo magnitudes to the first night (June 27), which was photometric. We then estimated aperture corrections on the field stars, that we applied to Chariklo measurements - see Carraro et al. (2006) and Galiazzo (2009) for further details. This correction turned out to be smaller than 0.10 mag in all filters. The final apparent magnitudes are reported, together with their uncertainties, in Table 1. At these data, this body has a phase angle of 4.34° and a mean magnitude in the R-band of 18.08 ± 0.02 for the 28^{th} of June 2006. This compares nicely with previous estimates, as illustrated in Table 2.

2.1 Light curve and rotational period

Up to now the only attempt to determine the the rotational period of Chariklo from its light curve was carried out by Peixinho et al. (2001) which detected a possible periodicity in the light curve of about 18.5 hours but with a confidence level below 50%. For this reason we investigated whether the data presented here support the presence of some significant variability and if they could give

Table 1: *Observational data for Chariklo. Mag is the apparent magnitude, σ error is the sum of the magnitude of Chariklo and the weighted average of the magnitude of the stars in common between the frames, A.M. the airmass, α is the solar phase angle and $t_0 = JD2453910$.*

JD date	*UT date*	*Filter*	*Exp(s)*	*A.M.*	*Mag*	$\alpha(°)$
t_0+4.6153	27/06 22:46:05	R	300	1.00	18.011 ± 0.050	4.34
t_0+4.6267	23:02:24	R	400	1.00	18.115 ± 0.017	4.34
t_0+4.6390	23:20:12	R	400	1.01	18.076 ± 0.012	4.34
t_0+4.6514	23:38:03	R	400	1.02	18.093 ± 0.021	4.34
t_0+4.7036	28/06 00:53:15	R	400	1.14	18.147 ± 0.027	4.34
t_0+4.7097	01:01:55	R	400	1.16	18.177 ± 0.021	4.34
t_0+4.7431	01:50:05	R	400	1.32	18.154 ± 0.026	4.34
t_0+4.7492	01:58:54	R	400	1.26	18.166 ± 0.020	4.34
t_0+4.7823	02:46:34	R	400	1.65	18.076 ± 0.030	4.34
t_0+5.6383	23:19:11	R	400	1.01	18.196 ± 0.048	4.35
t_0+5.6540	23:41:45	R	400	1.03	18.118 ± 0.053	4.35
t_0+6.6185	29/06 22:50:38	R	400	1.00	18.264 ± 0.028	4.36
t_0+6.6234	22:57:38	R	400	1.00	18.301 ± 0.018	4.36
t_0+6.6282	23:04:39	R	400	1.01	18.261 ± 0.016	4.36
t_0+6.6752	30/06 00:12:21	R	400	1.07	18.178 ± 0.033	4.36
t_0+6.6994	00:47:11	R	400	1.14	18.179 ± 0.020	4.36
t_0+6.7253	01:24:23	R	400	1.25	18.209 ± 0.023	4.37
t_0+6.7507	02:01:00	R	500	1.40	18.239 ± 0.015	4.37
t_0+6.7772	02:39:08	R	500	1.65	18.257 ± 0.017	4.37
t_0+4.6328	27/06 23:11:17	V	400	1.01	18.709 ± 0.027	4.34
t_0+4.6205	22:53:27	V	400	1.00	18.677 ± 0.024	4.34
t_0+4.6482	27/06 23:33:23	I	400	1.01	17.542 ± 0.018	4.34

us some insight on a possible light curve periodicity. At first we inspected accurately all the frames in our observations looking for possible dim sources in the vicinity of Chariklo which could disturb our brightness determination. This happened just in the first 4 frames (occultation of the star *USNO-A2.0/0600-14872238*) of the first night which consequently where excluded from our time series.

The stability of our reduced frames has been tested by looking at the variability of the brightness of a background star located near Chariklo on the CCD.

Table 2: *Data are shown in chronological order, all the absolute magnitudes were calculated using the value, $G = 0.15 \pm 0.05$ (Romanishin & Tegler 2005), for the Centaur class: date of observation, heliocentric distance, geocentric distance, phase angle, mean apparent magnitude in R- and I-band, the mean reduced magnitude in R-band, the absolute magnitude in R-band. All the data were normalized at $G = 0.15$: the absolute magnitudes in R-band evaluated before the 28^{th} of June 2006 are extrapolated by the mean apparent magnitude in the R-band in Table 1. The data are in order from the top to the bottom of: McBride et al. 1999, McBride et al. 1999, Jewitt & Luu 2001, Peixinho et al. 2001,Dotto et al. 2003,Dotto et al. 2003, this study.*

Date	r	Δ	α	$\overline{M_R}$	$\overline{M_I}$	$\overline{H_R(<\alpha>)}$	H_R
05/05/97	13.859	13.994	4.10	18.01±0.03	17.43±0.02	6.57	6.20
07/05/97	13.858	14.025	4.10	18.01±0.03	17.46±0.03	6.57	6.20
15/11/98	13.554	13.542	4.19	17.87±0.02		6.55	6.18
03/02/00	13.358	12.430	1.48	17.54±0.02		6.44	6.25
06/02/00	13.357	12.415	1.31	17.57±0.09	17.06±0.01	6.47	6.29
19/02/00	13.352	12.385	0.93	17.81±0.14		6.72	6.57
28/06/06	13.197	12.975	3.09	18.08±0.02	17.54±0.04	6.91	6.60

The brightness of the background star did not reveal any significant variability.

Considering that we only have few data, we studied the light curve with mainly two different statistical methods.

We use the `Period04` tool (http://www.univie.ac.at/tops/period04/), which is based on the Discrete Fourier Transformation (DFT). Second, we fit the data with a sinusoidal function through a classical weighted mean squares fit. The remaining frames (having been excluded the first four) were analyzed by using various values of the period window looking for periodicities in the range 2 hours to 48 hours. In this analysis we assumed that Chariklo's shape can be represented by a triaxial ellipsoid, with main axes $a > b \geq c$ and that rotation occurs around c. With this simplifying assumption the light curve could be approximated by a sinusoid. We hunt for a best fit periodicity by using a χ^2 method derived from the Lomb-Scargle periodogram.

$$\chi^2(P) = \sum_{i=1}^{N} \frac{(R(t_i) - R_i)^2}{\frac{\sigma_i^2}{N-1}}; \tag{4}$$

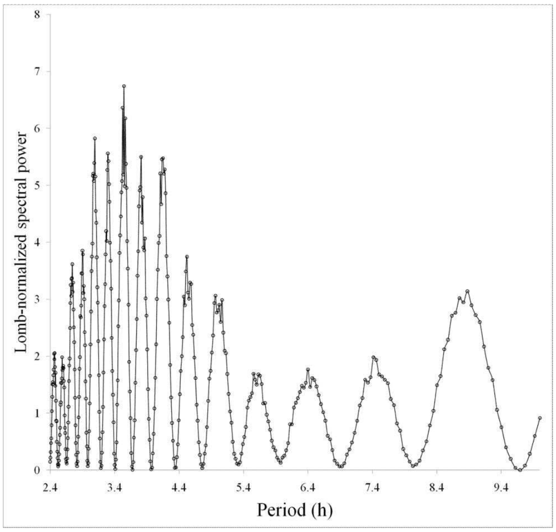

Figure 2: *The periodogram for Chariklo gives a period of (*3.55 ± 0.01*)h. With the Fisher randomization test (Monte Carlo permutation procedure), the probability that P does not have the computed-value is 0.012 and the probability of having a different period is 0.002. Using 2.4-10 h for the period search window (no asteroids with a rotational period lower than 2.4 h have been ever found, fission limit). The upper limit is conventional because we try to avoid getting something around 24 h that is the interval between observations.*

So we study the light curve in different cases, starting always to fit with a sinusoid; in this case the fitting of the sinusoid have been attempted by using several methods: in our one, the Lomb-Scargle periodogram and the χ^2 minimization, taking special care in minimizing the noise made by the time window. Using `Period04` we find a period equal to $(3.48 \pm 0.03)h$ and an amplitude of $(0.047 \pm 0.014)m$, a result very close to the one that we have perform with the periodogram (see Fig. 2).

Second, we fit the light-curve with a linear trend considering this fitting-function: $R(x) = A\sin(kx+w)+R_0+m*x$ (x =time, P =period, A =sinusoidal amplitude, R_0 =apparent magnitude at time zero and m =slope;m is used to model possible trends in the light-curve.). Having 13 degrees of freedom, the critical value for χ^2 at the 0.005 c.l. is $\chi^2_{0.995} = 29.82$, so having attempted by imposing m, the corresponding critical value is $\chi^2_{0.995} = 25.19$. For this reason we find the light-curve with the best chi-square ($\chi^2_{0.995} = 5.07$) and the period becomes $(3.49 \pm 0.01)h$, with $A = (0.068 \pm 0.007)m$, again inside the range suggested previously.

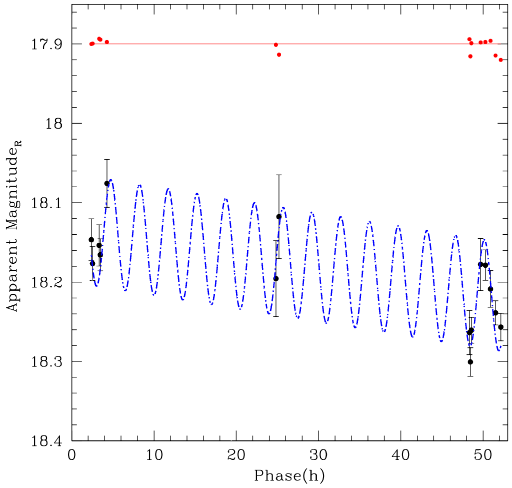

Figure 3: *Light Curve for the differential photometry of* $1997CU_{26}$ *with equation* $R(x) = -0.0684\sin(1.7988x - 0.6983) + 18.1311 + 0.0017x$. *Axis-x with the total-time with zero-point at 22:30 UT June 27th 2006; axis-y with the apparent magnitude. At the top the light curve of the control-star with his average magnitude*

We also compute the period assuming $m = 0$ and the best solution for this is $P \approx 30$ hours, with an overimposed variability of period 3.2 - 3.7 hours. But if m is left as a free parameter the long term periodicity disappears, suggesting that part of the "long term" variability is likely due to some residual trend in the data. Since both the phase angles, the heliocentric range and the geocentric range do not change appreciably over the three nights of observation, we investigated the possibility that the trend is due to some systematic effect in the calibration of the first night. It has to be noted that the gain in χ^2 leaving m as a free parameter is quite significant. Hence, a trend has to be included in the light–curve model, which can not be explained as a result of a residual calibration problem. Indeed, the analysis of the stability of the background stars did not reveal any trend in their light curves. It can not be due to an alias with the

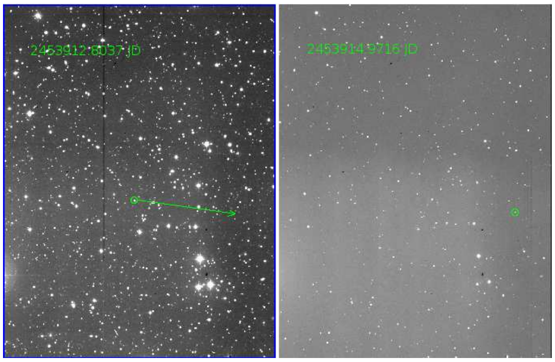

Figure 4: *Chiron' position on the first (left panel) and last night (right panel). The area is 13.78 × 18.00 arcmin. North is up, east to the left. The arrow indicates Chiron' motion over the whole run.*

time window too, as a simple Montecarlo analysis can demonstrate. It cannot be excluded however that Chariklo's real light curve is more complex than a sinusoid, but the present data can not prove or disprove this hypothesis.

In conclusion, our data suggest a rotational period from the Chariklo light curve of about 3.5 hours, with some hint for a more complex light curve.

3 Chiron

We secured photometric observations of Chiron during one run at June 2006 ($\bar{\Delta} = 13.32AU$ et $\bar{\alpha} = 2.30$). Here we have all photometric nights and we present a summary of the photometry in Table 3.

Due to the fact that the period of Chiron is well-known, we do a less peculiar analysis on the light curve of Chiron in front of the one of Chariklo. So we consider our best analysis to this data with this light curve which show strongly the linear trend, which we calculated as 0.004 mag/h during the night from June 26 to 28 and we find $A = (0.056 \pm 0.003)mag$, obtaining a final period of $(5.91 \pm 1.63)h$, which is in the range (Fig. 5) of the official recognized value.

Then we look for the activity over the last 2 decades obtaining the light curve over 20 years period integrated with the other researches on this Minor body, calculating and correcting all the absolute magnitude assuming a G value of 0.15, the most often adopted for this class of objects (Romanishin & Tegler

Table 3: *We have kept the proper error to the singular datum, because we need it for finding the rotational period for few data, we did the weighted least mean square method with a macro purpose-made to do this kind of thing adapting all to a sinusoid.* Mag *=values of R magnitude,* m_R*, at the proper UT-time, Filtr.=filter and* α *=solar phase angle and* $t_0 = JD2453910$.

JD	*Filt.*	*A.M.*	*Mag*	$\pm\sigma$	α
t_0+2.8037	R	1.05	16.921	0.023	2.36
t_0+2.8221	R	1.07	16.932	0.026	2.36
t_0+3.0228	R	1.13	16.936	0.035	2.35
t_0+3.0284	R	1.15	16.924	0.024	2.35
t_0+3.0344	R	1.16	16.908	0.032	2.35
t_0+3.0404	R	1.19	16.954	0.022	2.35
t_0+3.0464	R	1.21	16.935	0.021	2.35
t_0+3.0614	R	1.28	16.981	0.021	2.35
t_0+3.0674	R	1.31	16.996	0.021	2.35
t_0+4.8536	R	1.28	17.014	0.017	2.25
t_0+4.8596	R	1.25	17.065	0.019	2.25
t_0+4.8656	R	1.22	17.091	0.021	2.25
t_0+4.8888	R	1.14	17.066	0.014	2.25
t_0+4.8949	R	1.13	17.046	0.014	2.25
t_0+4.9009	R	1.11	17.074	0.011	2.25
t_0+4.9233	R	1.07	17.061	0.012	2.25
t_0+4.9294	R	1.07	17.070	0.038	2.25
t_0+4.9354	R	1.06	17.030	0.017	2.25
t_0+4.9414	R	1.06	17.040	0.017	2.24
t_0+4.9474	R	1.05	17.032	0.018	2.24
t_0+4.9535	R	1.05	17.035	0.0211	2.24
t_0+4.9595	R	1.05	17.012	0.013	2.24
t_0+4.9656	R	1.05	17.008	0.027	2.24
t_0+4.9716	R	1.06	17.076	0.059	2.24
t_0+4.9716	R	1.06	17.117	0.025	2.24
t_0+2.9616	B	1.05	17.815	0.025	2.36
t_0+2.8097	V	1.06	17.287	0.026	2.36
t_0+2.9826	I	1.06	16.564	0.590	2.36

(2005)): Fig.6 and Table 4.

Looking at the light curve on the twenty (years), we see that the figure

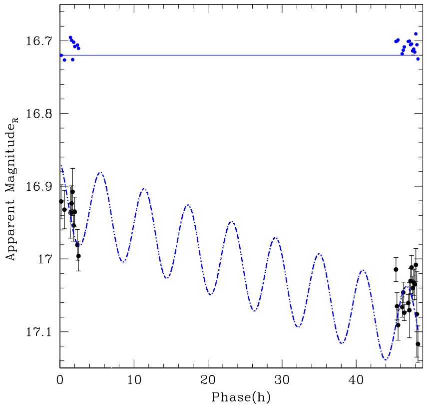

Figure 5: *Rotational light curve of* 2060 *Chiron obtained UT 2006 June 26-28 at Swope 1.0m Telescope on Las Campanas. The rotational period had a linear brightening trend. The equation of the curve is* $M_R = 0.0560 * (1.0630 * h - 1.1398) + 16.9162 + 0.0038 * h$.

confirms the trend of the previous ones, as it can be seen in Duffard et al. (2002), so correcting the slope-parameter G does not get too much difference. However the variations in the absolute magnitudes during the years show the presence of the cometary activity of this body and we can see changement in the range of the light curve when the coma is diluting itself, causing variations in the reflected light of the nucleo. In fact we can think on the well studied of back-scattering effect, so when the coma decreases its amplitude, the intensity of back-scattering does the same in a proportionally way.

Colours and Conclusions

Chariklo looks much more red than Chiron and if we look the absolute magnitude in Table 2 and 4 is just like the opposite, Chiron is more brilliant in red than 1997 CU_{26} of quite a magnitude of difference.

Here a comparison with some of the most recent data of the range of colours (http://www.psi.edu/pds/asteroid/EAR_A_COMPIL_3_TNO_CEN_COLOR_V3_0/data/tnocencol.tab) of Centaurs and the Sun. In particular for the Sun:

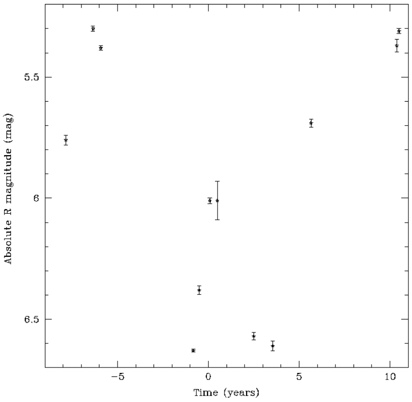

Figure 6: *Absolute R magnitude of Chiron from 1988 to 2006. The zero-point is January* 1^{st} *1996. Relevant is the maximum of 1996 and the 3 maximum points, one in 1991 and two in 2006.*

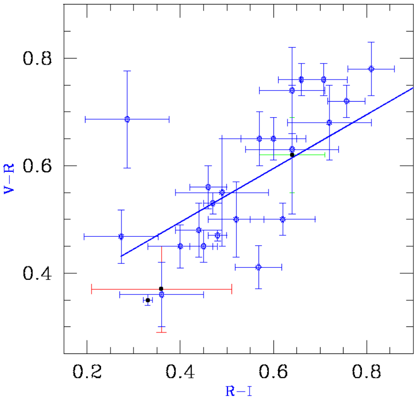

Figure 7: *Centaurs-Colour indexes* $(V-R)$ *vs* $(R-I)$*. Full dots for the Sun, Chiron and Chariklo, in order from left to right.*

Table 4: *r is the heliocentric distance, Δ is the geocentric distance, α is the solar phase angle, $\overline{m_R}$ is the mean apparent R magnitude, $\overline{H_R(\alpha)}$ is the mean absolute R magnitude and H_R the reduced R magnitude. First three lines are taken from Luu & Jewitt (1990), the 4^{th} and 5^{th} ones from Lazzaro et al. (1996); the 6^{th} and 7^{th} are signed with a symbol, because they are not properly a medium, but single measures, taken from Lazzaro et al. (1997); the two after are medium values taken from Duffard et al. (2002) and the last two are our ones.*

UT	r	Δ	α	$\overline{m_R}$	$\overline{H_R(\alpha)}$	H_R
29/02/1988	12.60	12.33	4.4	17.10 ± 0.02	6.14	5.76
25/08/1989	11.56	12.20	3.8	16.40 ± 0.01	5.65	5.30
30/01/1990	11.26	10.39	2.4	16.11 ± 0.01	5.77	5.38
25/03/1995	8.538	7.557	1.22	15.850± 0.006	6.80	6.63
02/07/1995	8.494	8.764	6.51	16.231±0.017	6.87	6.38
29/01/1996	8.454	8.033	6.19	15.651± 0.012 (♣)	6.49	6.01
12/06/1996	8.465	8.133	6.60	15.694± 0.08(♣)	6.51	6.01
01/07/1998	9.012	8.411	5.40	16.409± 0.016	7.01	6.57
20/07/1999	9.445	8.959	5.10	16.671± 0.020	6.77	6.61
24/08/2001	10.891	10.460	4.90	16.230 ± 0.016	5.95	5.69
22/05/2006	14.115	13.723	3.83	17.103 ± 0.026	5.73	5.37
26/06/2006	14.175	13.332	2.35	16.948± 0.011	5.57	5.31

Table 5: *Colour index $(B-V)$,$(R-I)$,$(V-I)$ of 2060 Chiron and 1997 CU_{26}.*

Minor Body	*Date*	$(B-V)$	$(V-I)$	$(V-R)$	$(R-I)$
Chariklo	26 June 2006	$--$	1.17 ± 0.08	0.62 ± 0.07	0.64 ± 0.07
Chiron	26 June 2006	0.53 ± 0.05	0.72 ± 0.08	0.37 ± 0.08	0.36 ± 0.15

$(B-V)_\odot = 0.642 \pm 0.016$,$(R-I)_\odot = 0.332 \pm 0.008$,$(V-I)_\odot = 0.688 \pm 0.014$ and $(V-R)_\odot = 0.354 \pm 0.010$. There is a linear trend in $(V-R)$ vs $(R-I)$ colours (Fig.7) and with a linear least square we obtain this linear relation in colours: $(V-R) = 0.50 * (R-I) + 0.29$. Colour indexes of Chiron are very similar with those ones of the Sun (Holmberg et al. (2006)). Chiron is one of the least reddish of the Centaur, instead Chariklo is quite over the average.

For $(V-R)$ vs $(B-V)$, it seems that Centaurs are divided in 2 main families with Chiron being a peculiar one with 2002 CB_{249} (the least Bluish, Fig. 8), but again with a linear correlation (Fig. 9): $(V-R) = 0.33 * (B-V) + 0.29$.

Finally for (V-I) vs (B-V): $(V-R) = 1.20 * (B-V) + 0.06$. There is a very nice linear correlation and it is still possible to have 2 families (Fig. 10).

References

Brown, M.E., Koresko, C.C.: 1998, *ApJ*, 505, L65
Carraro, G. 2006, A&A, 460 L39
Carraro, G. 2009, AJ, 139, 3089
Davies, J.K. 1997, Icarus, 134, 213
Duffard, R. 2002, Icarus, 160, 44
Galiazzo, M. 2009, Master Thesis, Padova University
Hartmann, W.K. 1982, BAAS, 14, 719
Holmberg, J. 2006, MNRAS, 367, 449
Landolt, A.U. 1992, AJ, 104, 340
Lazzaro, D. 1996, Planet. Space Sci., 44, 1547
Lazzaro, D. 1997, Planet. Space Sci., 45, 1607
Luu, J.X., Jewitt, D.C. 1990, AJ, 100, 913
McBride, N. 1999, MNRAS, 306, 799
Peixinho, N. 2001, A&A, 371, 753

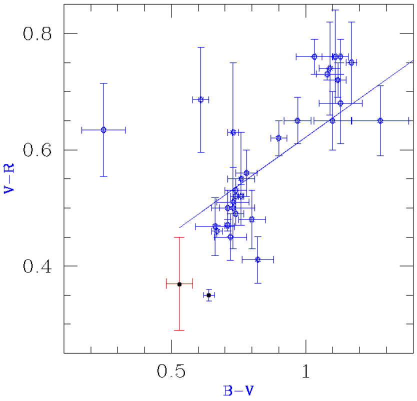

Figure 8: *Centaurs-Colour indexes* $(V-R)$ *vs* $(B-V)$*. Full dots for the Sun and Chiron, in order from right to left.*

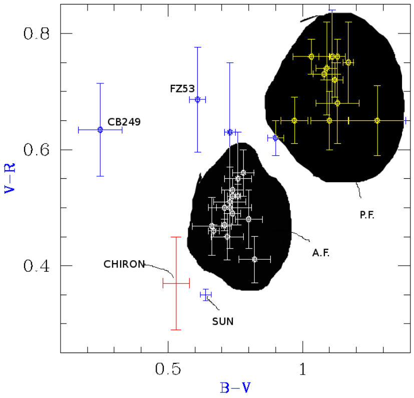

Figure 9: *Distinction in two families for Colour indexes of Centaurs* $(V-R)$ *vs* $(B-V)$*. We can see a couple of peculiar Cenataurs as Chiron and two main families, that we have called the Asbolus Family (A.F.) and the Pholus Family (P.F.).*

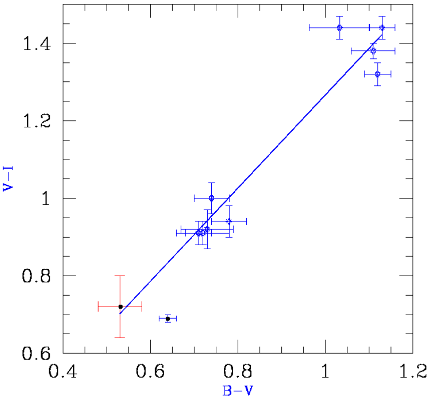

Figure 10: *Colour indexes of Centaurs* $(V-I)$ *vs* $(B-V)$*. The full dots are about the Sun and Chiron, in order from left to right.*

Romanishin, W., Tegler, S.C. 2005, Icarus, 179, 523
Sheppard, S.S., Jewitt, D.C. 2002, AJ, 124, 1757
Silva, A.M., Cellone, S.A. 2001, Planetary and Space Science, 49, 1325
Stansberry, J. 2008, The Solar System Beyond Neptune, 161
Stetson, P.B. 1987, PASP, 99, 191

PADEU **20**, 59 (2011)
ISBN 963 463 557
© Published by the Astron. Dept. of the Eötvös Univ.

Near-Earth asteroids and the Kozai-mechanism

Barbara Koponyás

Eötvös University, Department of Astronomy, H-1518 Budapest, Pf. 32, Hungary

E-mail: `b.koponyas@gmail.com`

Abstract
In 1962 Yoshihide Kozai found that above of a critical inclination the argument of pericenter don′t precess rather than librate around 90° or 270°, we name this the Kozai-mechanism. I examined the Near-Earth Asteroids, in order to find out how many of them are in the Kozai-mechanism. More than 10 years ago, some astronomers examined this, but at that time they knew less than 500 Near-Earth Asteroids. Now we know more than 6500.

Keywords: *Near-Earth asteroids, Kozai-mechanism*

1 Introduction

Near-Earth Objects (NEOs) are comets and asteroids that have been nudged by the gravitational attraction of nearby planets into orbits that allow them to enter the Earth's neighborhood. In terms of orbital elements, NEOs are asteroids and comets with perihelion distance q less than 1.3 AU. Near-Earth Comets (NECs) are further restricted to include only short-period comets (i.e orbital period P less than 200 years).

The vast majority of NEOs are asteroids, referred to as Near-Earth Asteroids (NEAs). NEAs are divided into groups (Aten, Apollo, Amor) according to their perihelion distance (q), aphelion distance (Q) and their semi-major axes (a).

In 1998 NASA commenced its part of the "Spaceguard" effort, with the goal of discovering and tracking over 90% of the near-Earth objects larger than one kilometer by the end of 2008. There are several Near-Earth Object (NEO) discovery teams: Lincoln Near-Earth Asteroid research (LINEAR), Near-Earth Asteroid Tracking (NEAT), Spacewatch, Lowell Observatory Near-Earth Object Search (LONEOS), Catalina Sky Surveys, Japanese Spaceguard Association (JSGA), Asiago -DLR Asteroid Survey.

You can find these results in the Horizons System, or in the JPL Small-Body Database Search Engine. The JPL HORIZONS on-line solar system data and ephemeris computation service provides access to key solar system data and flexible production of highly accurate ephemerides for solar system objects. You can use JPL Small-Body Database search engine to generate custom tables of orbital and/or physical parameters for all asteroids and comets.

In 1962 Yoshihide Kozai examined the secular perturbations of asteroids with high inclination and eccentricity with analytical methods. He found that above of the critical inclination (39.2°) the argument of pericenter don't precess rather than librate around 90° or 270°, while the oscillations of e and i are coupled (Kozai , 1962). In 1979 astronomers discovered the first asteroid, which showed this mechanism, the 3040 Kozai.

In 1995 Patrick Michel and Fabrice Thomas examined 10 NEAs by numerical and analytical methods, which semi-major axes smaller than 2 AU (Michel & Thomas , 1996). They found 4 asteroids which showed the Kozai mechanism, but 2 of them has small inclination ($i < 14°$) and the ω librate around 180°. An important effect of the mechanism is to protect the objects from encounters with the planets. Two types of protection mechanisms are possible:

1. For bodies whose values of a and e are such that they could encounter the planets only near perihelion (or aphelion), such encounters may be prevented by the high inclination and the libration of ω about 90°or 270° (even when the encounters occur, they do not affect much the asteroid's orbit due to comparatively high relative velocities)

2. Another mechanism for NEAs, is viable when at low inclinations when ω oscillates around 0° or 180° and the asteroid's semi-major axis is close to that of the perturbing planet: in this case the node crossing occur always near perihelion and aphelion, namely far from the planet itself provided the eccentricity is high enough and the orbit of the planet is almost circular.

For main-belt asteroids ($a > 2$ AU) only the former mechanism can work, while among NEAs both are possible. With both protection mechanisms, during the stay inside the mechanism there are no drastic changes of a and the orbits behave as if they were in a meta-stable state.

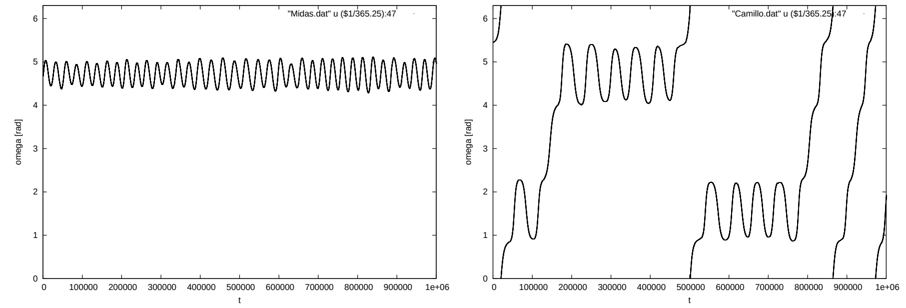

Figure 1: *The results of the calculations for the Midas and the Camillo.*

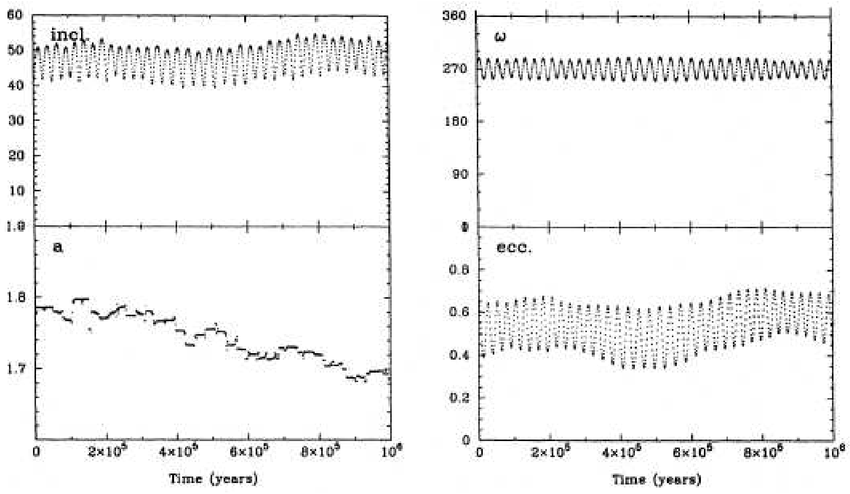

Figure 2: *The results of Michel & Thomas (1996) for Midas*

2 Calculations

I used the Bulirsch-Stoer integrator. First I examined the same asteroids, which was examined by Michel & Thomas (1996), these are the Midas, Camillo, 1986 PA and the Nereus. After that I calculated the orbital elements of other NEAs. From the JPL Small-Body Database I found 309 NEAs, whose inclination is

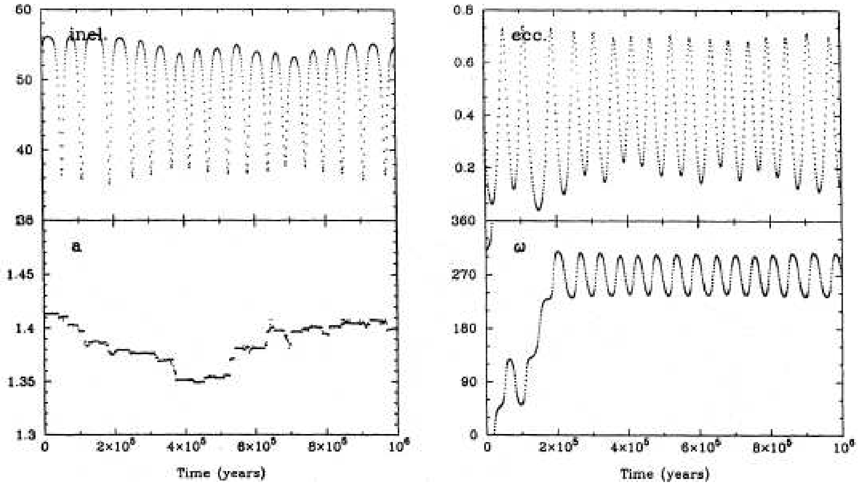

Figure 3: *The results of Michel & Thomas (1996) for Camillo*

larger than 39.2° and the perihelion distance q less than 1.3 AU, and 4149 NEAs, with inclination smaller than 14°. I have numerically integrated the orbital elements of 104 asteroids with high inclination and 50 with low inclination to 1 Myr forward in time, as well as 4 asteroids with high inclination to 5 Myr. The perturbing planets are Venus, Earth, Mars, Jupiter, Saturn, Uranus and the Neptune. The program show the results every 10th year, in this way we can see the little changes too.

3 Results

Midas I found that the orbit elements show the same changes that Michel & Thomas (1996) have got over 1 Myr. The ω librate around 270° over 1 Myr.

Camillo In this case the changes of the ω show the same behaviour until the first 0.5 Myr, after that the ω librate around 90° instead of 270°.

1986 PA This asteroid has low inclination, and my results are not the same as earlier. I didn't find ω -libration around 180° from 700000 yr to 900000

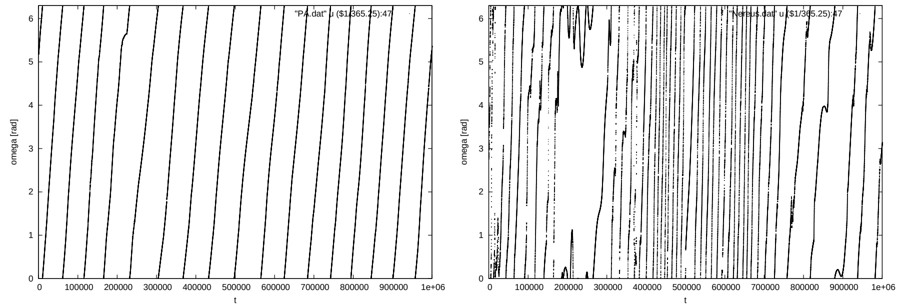

Figure 4: *The results of the calculation for the 1986 PA and the Nereus.*

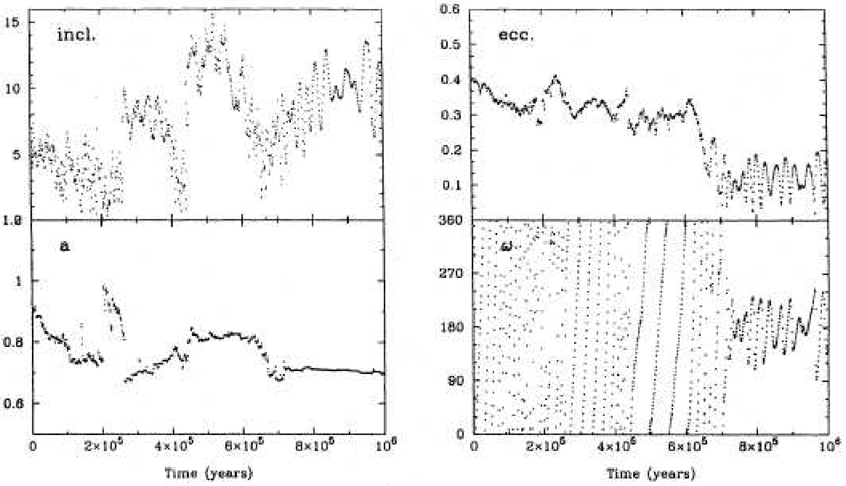

Figure 5: *The results of Michel & Thomas (1996) for 1986 PA*

yr. The ω precess over 1 Myr. The other orbit elements show discrepancy too.

Nereus The argument of pericenter precess and librate but don't librate around the expected value and at the right time. This asteroid has low inclination too.

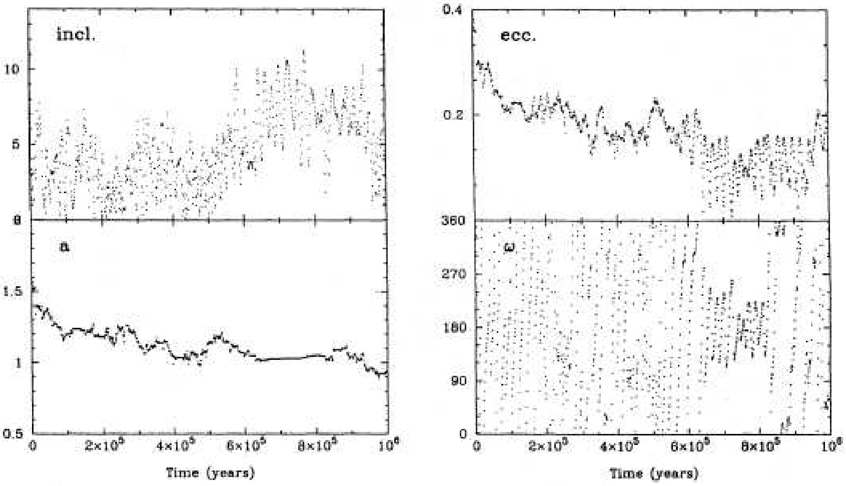

Figure 6: *The results of Michel & Thomas (1996) for Nereus*

Izhdubar Its inclination is 63.46° and the argument of pericenter librate around 90° over 1 Myr. The eccentricity and the inclination are coupled oscillation, e being minimum, when i is maximum and vice versa.

DV24 Its inclination is 55.89° and the ω only precess. The inclination and the eccentricity are coupled oscillation, but the period is shorter.

JW6 Its inclination is 51.31° and the ω first librate around 90°, after one of the periods it start librate around 270° for a long time and after that again start librate around 90°.

PT42 The orbital elements of this asteroid show an interesting behaviour. When the precess of the ω turn to librating, the amplitude of the eccentricity and the inclination is higher.

I examined 104 asteroids which has high inclination and 50 asteroids which has low inclination. From the previous 59 asteroids' ω show the Kozai-libration and from the latter only 9. When I calculated the orbital elements of 4 asteroids with high inclination to 5 Myr, two of them show that the ω librate or precess over 5 Myr, the other two asteroids show both behaviour.

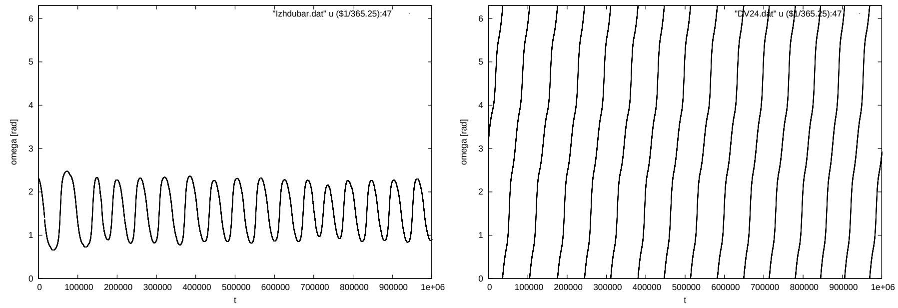

Figure 7: *The results of the calculation for the Izhdubar and the DV24.*

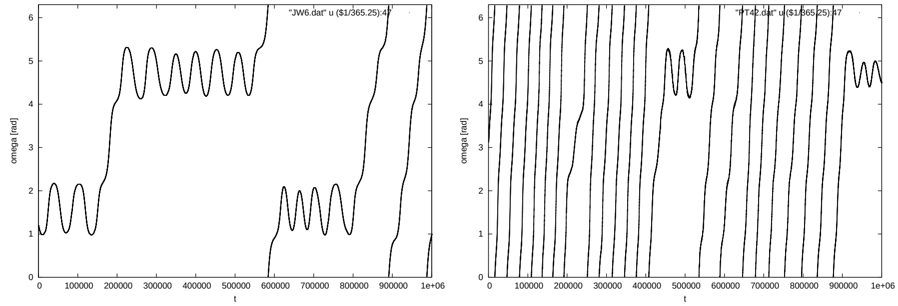

Figure 8: *The results of the calculation for the JW6 and the PT42.*

4 Summary

I examined 104 high inclination NEAs and 50 low inclination NEAs. From the 104 asteroids 59 show the Kozai-libration and from the 50 asteroids only 9 show this and 7 impact to the Sun. My results show that the Kozai-libration is quite common phenomenon within the NEAs with high inclination. The ω librate around 90° or 270°, but NEAs with low inclination don't show this regular behaviour quite often, instead they show chaotic behaviour. The omega changes chaoticaly because the perturbations of other planets are much stronger than when the asteroids which have high inclination. When we want to say that the NEA is potentially hazardous for an impact with the Earth, we have to do more calculations with several initial value especially when we examine a low inclination asteroids.

References

Y. Kozai, 1962, AJ. 67, 591
P. Michel, F. Thomas, 1996, A&A 307, 310

PADEU PADEU **20**, 67 (2011)
ISBN 963 463 557
© Published by the Astron. Dept. of the Eötvös Univ.

Frequencies of librational motions around the Lagrange point L_4

Renáta Rajnai[1], **Imre Nagy**[2], **Bálint Érdi**[1]

[1] Eötvös University, Department of Astronomy, H-1518 Budapest, Pf. 32, Hungary
[2] MTA Research Group for Physical Geodesy and Geodynamics Műegyetem rakpart 3, 1111 Budapest, Hungary

E-mail: `R.Rajnai@astro.elte.hu`

Abstract
Frequencies and resonances of librational motions in the elliptic restricted three-body problem around the point L_4 were determined and examined. We integrated the equations of motion of a fictitious Trojan body by changing the eccentricity e and mass parameter μ of the system. Using Fourier transform we determined the frequencies and resonances of the Trojan's motion. The numerically found frequencies are in good agreement with the analytical frequencies, and the determined resonances fit the resonance curves of Érdi et al. (2007) considering secondary resonances at co-orbital motions.

Keywords: *elliptic restricted three-body problem, librational motions, Trojans, frequencies, resonances*

1 Introduction

The elliptic restricted three-body problem (ERTBP) is a classical field of celestial mechanics that has been studied for a long time by many authors. This problem describes a system that contains three bodies, two of them moving in elliptic orbits, and the third one has negligible mass, compared to the others. The two larger bodies can be a star (with mass m_1) and a planet (m_2), and the one with negligible mass an asteroid (m_3). The most known example for the

ERTBP is the Sun-Jupiter-asteroid system, where Trojan asteroids are librating around the L_4 and L_5 points of Jupiter. To date we know more than 4000 Trojan bodies in the Solar system, as asteroids and also Trojan moons.

The stability of motions near the Lagrangian triangular solutions is an interesting question and has an extensive scientific literature (Danby, 1964; Bennett, 1965; Skokos & Dokoumetzidis, 2001; Marzari & Scholl, 2002; Érdi & Sándor, 2005; Freistetter, 2006; Érdi et al., 2007). Danby (1964) in his study on the stability of the triangular points in the elliptic restricted problem of three bodies applied the Floquet theory to the first variational equations of motion for small mass parameter ($\mu = m_2/(m_1 + m_2)$) and eccentricity, to obtain the transition curves for stability of L_4. He found that the transition curves form a *"V"* - like shape in the mass parameter - eccentricity plane. Below these curves the triangular points are positions of stable equilibrium. The characteristic roots of the variational equations were determined by Bennett (1965). He found that the unstable region of L_4 in the $\mu - e$ plane is divided into three parts, according to the types of the four characteristic roots (2 real roots and 2 complex roots of unit modulus; 4 real roots; 4 complex roots of non-unit modulus, respectively). In the paper of Érdi et al. (2009) and Rajnai et al. (2010) escape times from L_4 are discussed. We note that in the unstable region of L_4 the escape time - the time until libration exists - increases along a curve which fits the transition curve between the 4 real and the 4 complex roots.

The recent paper deals with the frequencies and resonances in the stable region of L_4. Motions around L_4 were investigated, but due to symmetry the results can be applied for L_5 also. For the numerical computations we used the equations of motion of the planar ERTBP, so considered only the effect of Jupiter and the Sun on the Trojan's motion.

2 Frequencies of motions

To study the problem we made the integration of the equations of motion for several hypothetical systems, with different mass parameters and eccentricities of the primaries for initial conditions corresponding to librational motions around L_4. We used a grid to change μ from 0.0001 to 0.1 with a step size of $\Delta\mu = 0.0001$, and e from 0.0 to 1.0 with a step size of $\Delta e = 0.002$. That means approximately 500 000 mass parameter - eccentricity pairs, so the results can be applied in general for several hypothetical and known Trojan systems.

To determine the librational frequencies we used Fast Fourier Transform (FFT) part of GSL (GNU Scientific Library). The paper of Temperton (1983) contains the description of the algorithm. The integrations of the equations of motion were made for 1250 periods of the primaries to get practicable Fourier spectra, thus we could obtain the frequencies. In the stable region of L_4 we determined the four frequencies, normalized with the mean motion of the planet: $n_s, n_l, 1 - n_s$, and $1 - n_l$. Here n_s and n_l stands for the short and long periods of the libration, and $1 - n_s$, and $1 - n_l$ are the consequences of elliptic motion, because the Lagrange point L_4 is moving in an elliptic orbit too.

The exact frequencies of librational motions around L_4 in the circular restricted three-body problem have been determined analytically and for comparison with numerical methods. Table 1 contains this comparison for different mass parameters. The last column shows the difference between the frequencies obtained by the two methods, which appears only at the 4^{th} decimal digit. This indicates the precision of the numerical frequency determination.

Table 1: *Comparison of the frequencies determined by numerical and analytical methods for $e = 0$*

μ	n_s (analytical)	n_s (numerical)	Δn_s
0.0001	0.999662	0.999299	0.000363
0.0002	0.999324	0.998699	0.000625
0.006	0.978763	0.97811	0.000653
0.01	0.963322	0.962517	0.000805
0.02	0.918191	0.91794	0.000251
μ	n_l (analytical)	n_l (numerical)	Δn_l
0.0001	0.0259882	0.0257871	0.0002011
0.0002	0.0367635	0.0367816	-0.0000181
0.006	0.204995	0.204897	0.000098
0.01	0.268348	0.268066	0.000282
0.02	0.396138	0.396001	0.000137

Figure 1 shows the variation of the frequencies as a function of the mass parameter, for the eccentricities $e = 0.002$, 0.02, 0.08 and 0.14. It can be seen, that the variation is monotonous, and the change of the mass parameter affects the frequencies more, than the increase of the eccentricity. Features of the four figures in Figure 1 remain similar with the change of e, except the lack of data increasing. At $e = 0.02$, 0.08 and 0.14 there is a lack of data in n_s and $1 - n_s$, which is the consequence of the unstable region of L_4. Bennett (1965) determined the characteristic roots in the unstable region of L_4 and found that besides 2 real roots, 2 complex roots of unit modulus also exist. We could not

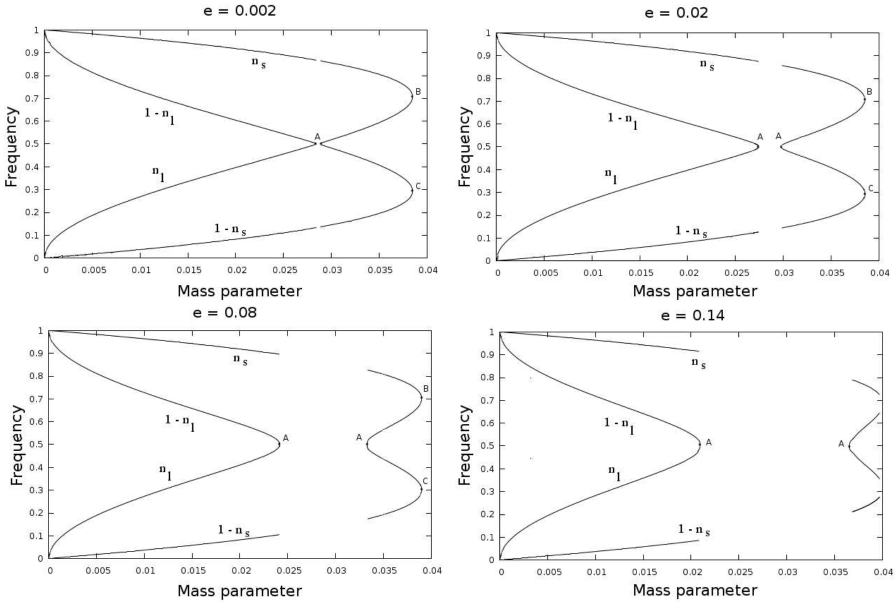

e = 0.002

e = 0.02

e = 0.08

e = 0.14

Figure 1: *The change of the four frequencies as a function of the mass parameter at given eccentricities.*

find the real roots in this region by the FFT, because the escape time of the asteroid is too short and we could not get practicable Fourier spectra.

3 Resonances

Knowing the frequencies of the librational motions we can determine the resonances. We used data in the surroundings of the resonances under study with a small radius ±0.001.

For the four frequencies of the ERTBP 6 types of resonances are possible (Érdi et al., 2007). In Figure 2 the so-called A-type resonances $[(1 - n_l) : n_l]$ are shown. These were computed by fixing the eccentricity and changing the mass parameter, and searching for a frequency which agreed with the prescribed resonant value within a tolerance 0.001, and then the eccentricity was increased

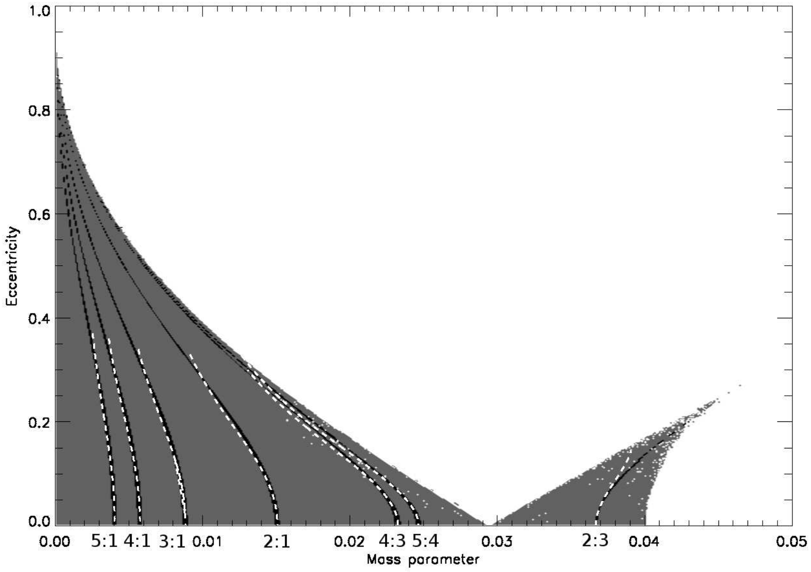

Figure 2: *A-type* $(1 - n_l) : n_l$ *resonances in the stable region.*

and the whole process repeated.The grey region indicates $(\mu; e)$ pairs for which librational motions around L_4 are stable during the integration time. The black thick lines marks the resonances obtained by numerical integration. The dashed white lines indicates resonances determined by Érdi et al. (2007) using Rabe's algebraic equation (Rabe, 1973) for the frequencies. The curves determined by the two different methods fit very well at small eccentricities, since Rabe's equation can be used only for small and moderate values of e. The turning points of the two kinds of resonance curves show the validity limit of Rabe's equation. Features of the other (B,C,D,E and F) types of resonances are similar, they also agree well with the analytically determined resonance curves.

4 Summary

Librational frequencies and resonances of hypothetical Trojan asteroids were determined using numerical methods, by changing the mass parameter and eccentricity of a star-planet-asteroid system. The results are in good agreement with earlier ones obtained by analytical methods. These can be applied to hypothetical and also for known Trojans. A future work could be to determine the frequencies in the unstable region of L_4 with other methods to fill the lack of data in Figure 2. It is also an interesting question what happens when the resonance curves have intersections, how does this affect the stability of the asteroid.

Acknowledgement

The European Union and the European Social Fund have provided financial support to the project under the grant agreement no. TÁMOP-4.2.1/B- 09/1/KMR-2010-0003.

References

Bennett, A., 1965, Icarus, 4, 177

Danby, J.M.A., 1964, AJ, 69, 165

Érdi, B., Sándor, Zs., 2005, CeMDA, 92, 113

Érdi, B., Nagy, I., Sándor, Zs., Süli, Á., Fröhlich, G., 2007, MNRAS, 381, 33

Érdi, B., Forgács-Dajka, E., Nagy, I., Rajnai, R., 2009, CeMDA, 104, 145

Freistetter, F., 2006, A&A, 453, 353

Marzari, F., Scholl, H., 2002, Icarus, 159, 328

Rabe, E., 1973, Recent Advances in Dynamical Astronomy, (D. Reidel Publ. Co., Dordrecht)

Rajnai, R., Nagy, I., Érdi, B., 2010, J. Phys. Conf. Ser., 218, 012018

Skokos, Ch., Dokoumetzidis, A., 2001, A&A, 367, 729

Temperton, C., 1983, JCoPh, 52, 340

PADEU
PADEU **20**, 73 (2011)
ISBN 963 463 557
© Published by the Astron. Dept. of the Eötvös Univ.

Dynamical investigation of Pluto's moon system

Zsuzsa Zsigmond and Áron Süli

Eötvös University, Department of Astronomy, H-1518 Budapest, Pf. 32, Hungary

E-mail: `Zs.Zsigmond@astro.elte.hu`

Abstract
We present a detailed survey of the dynamical structure of the phase space around the new moons of the Pluto-Charon system. We investigated the system in the framework of the spatial elliptic restricted three-body problem. Stability maps were created using chaos indicators both on the semi-major axis - eccentricity and semi-major axis - inclination plane. The structures related to the 4:1 and 6:1 mean motion resonances are clearly visible on the maps, but the detailed investigation of the resonant arguments shows no evidence of the resonances. We showed the possibility that Nix might be in the 4:1 resonance if its argument of pericenter or longitude of node falls in a certain range. Recently we improved our model to the general four-body problem, which can provide more accurate information about the stability, motion and possible resonances between the moons and Charon, which is relevant, since the 'New Horizons' mission will reach and study the system in 2015.

Keywords: *celestial mechanics - Pluto - moons*

1 Introduction

Pluto's first moon, Charon was found by Christy & Harrington (1978), which greatly facilitated the study of Pluto. The Pluto - Charon system is remarkable, since in the Solar system Charon is the largest moon relative to its primary, with the highest mass ratio of 0.1166 (Tholen 2008, hereafter referenced to as T08).

The discovery of Pluto's new moons (Weaver 2005, Weaver 2006), Nix and Hydra rendered the system even more interesting. They orbit the center of mass of the system, which is very close to the Pluto-Charon barycenter. Thank to this, in latter years numerous studies were devoted to the system. The most important results are the following:

In 2006 two-body orbit solutions for Nix and Hydra were computed by Buie using the Hubble Space Telescope (Buie 2006, hereafter referenced to as B06). According to the results, the orbital periods of Nix and Hydra are close to the ratio of 4:1 and 6:1 with that of Charon, respectively, indicating mean-motion resonances. In this paper two bodies are in mean-motion resonance, when $n/n' = p/(p+q)$, where n and n' are the mean motions, p and q are small integers, where q is the order of the resonance. Some of Buie's major conclusions are: (*i*) Nix and Hydra are in nearly circular orbits, with eccentricities of 0.0023 and 0.0052, respectively, (*ii*) the orbits of the small moons are almost coplanar with Charon's orbit, (*iii*) the orbital periods of Nix and Hydra are nearly commensurate with the period of Charon, but differ significantly from the exact ratios of 4:1 and 6:1, respectively. We note that in B06 the eccentricity of Charon was assumed to be zero. We demonstrated that the eccentricity of Charon substantially influences the phase space of the Pluto–Charon system; for details see Süli & Zsigmond (2009, hereafter referenced as S09).

In 2008 four-body orbit solution was computed by T08 fitting all the 22 parameters simultaneously. They studied whether the direct perturbations might be too strong to permit a sufficiently accurate extrapolation forward to the '2015 - New Horizons' spacecraft encounter with Pluto. Also, with adequate data, this four-body orbit solution should yield the mass for each member of the system. Their major conclusions are the follows: (*i*) Pluto's three moons are not quite coplanar, (*ii*) the new moons' orbit planes precess around the system's invariable plane with periods of ≈ 5 and ≈ 15 years, (*iii*) the orbital eccentricities are nonzero, but small for all three moons, (*iv*) there is no evidence of any mean motion resonances. Nagy et al. (2006) studied the phase space of the Pluto–Charon system in the framework of the spatial circular restricted problem. The moons were treated as test particles and their semi-major axes, eccentricities and inclinations were varied. Summarizing their results: (*i*) the region inside 42 000 km is unstable, thus no moon could exist there, (*ii*) both moons reside in the stable region and the upper limit for the eccentricities are 0.17 for Hydra and 0.31 for Nix, far greater, than the current values of the moons, (*iii*) in the semi-major axis–inclination plane the 4:1 and 6:1 resonances are clearly visible above ≈ 20° and ≈ 35°, respectively. Our main goal was to extend the previous investigations using the spatial elliptic restricted and general four body problems. Detailed analysis can be found in the work of S09. This paper is organized as follows: Section 2 describes the model and the initial conditions; Section 3 is devoted to the methods and in Section 4 we present the new results.

2 Models and initial conditions

Since the orbital radii of the moons are much smaller than the Hill radius ($\approx 8.0 \times 10^6$ km) of the Pluto-Charon system, the moons are deep in Pluto's gravitational well, so the perturbations by the Sun can be ignored, as did T08.

First we applied the model of the spatial elliptic restricted three-body and later the general four-body problem. We integrated the dimensionless equations of motion. An obvious advantage of using such equations is that the results are independent of the exact value of the semi-major axis of Charon. The unit of length was chosen such that the separation of Pluto and Charon (the primaries) is unity, i.e. the semi-major axis of Charon $a_1 = 1$ A in all computations.

Let the unit of mass be the sum of the primaries, and the unit of the time the orbital period of Charon. The orbital plane of the primaries was used as reference plane, in which the line connecting the primaries at $t = 0$ defines a reference x-axis. The initial orbital elements are given in S09.

We study the problem more generally by considering the effect of non-zero inclinations on the orbital stability. The mass parameter $\mu = 0.104424$ was chosen according to the mass ratio of 0.1166, published in T08. To examine the phase space in the vicinity of Nix and Hydra separately we varied the initial orbital elements of the test particles. Stability maps were created for the $(a - e)$ and $(a - i)$ orbital element space for both moons for different eccentricity e, inclination i, argument of pericenter ω and longitude of node Ω values. In total more than 14 million orbits were calculated, which resulted in $2 \times 80 = 160$ stability maps for each moon. Due to the very small step size in a and e, each $(a - e)$ stability map corresponds to more than 6×10^4 initial conditions, thus providing a very fine resolution.

3 The applied methods

To compute the stability maps, the method of the maximum eccentricity (ME), the Lyapunov characteristic indicator (LCI) and the relative Lyapunov indicator (RLI) were used as tools for stability investigations of the massless bodies representing the small moons.

Table 1: *The initial orbital elements for the test particles. In the upper part the intervals of the semi-major axes along with the step sizes* Δ *are listed for the stability maps* $(a-e)$ *and* $(a-i)$. *The lower part shows the intervals (I) for the orbital elements* $[e]_k$, $[\omega]_l$ *and* $[\Omega]_l$ *and the respective step sizes* (Δ'). *For details see S09.*

Map	a [A]	e	i [deg]	
Nix	[2.40,2.64]	[0,0.4]	[0,45]	
Hydra	[3.22,3.38]	[0,0.4]	[0,45]	
Δ	10^{-3}	10^{-3}	1	
	$[e]_k$	$[i]_k$ [deg]	$[\omega]_l$ [deg]	$[\Omega]_l$ [deg]
I	[0,0.4]	[0,40]	[22.9,337.9]	[0,315]
Δ'	0.1	10	45	45

The ME method uses as an indication of stability a straightforward check based on the eccentricity. This action-like variable shows the probability of orbital crossing and close encounter of two bodies and therefore its value provides information on the stability of orbits. This simple check was found to be a powerful indicator of the stability character of orbits in previous investigations (Dvorak et al. 2003; Süli et al. 2005; Nagy, Süli & Érdi 2006). In this work we define ME as follows:

$$\mathrm{ME} = \max_{t\in[0,10^4]T_{\mathrm{C}}}(e).$$

We plotted ME_{-}, where:

$$\mathrm{ME}_{-} = \begin{cases} 1 & \text{if ME} = 1 \\ \mathrm{ME} - e_0 & \text{otherwise} \end{cases},$$

where e_0 is the initial eccentricity of the test particle.

As a complementary tool, we computed also the RLI (Sándor et al. 2006) and the LCI (Froeschlé 1984), which are well-known chaos indicators.

4 Results

Here we show the ME_{-} stability maps, presenting one phase space structure for Nix. On Figure 1 white solid lines are contour lines: along them ME_{-} has a constant value, this way they can draw the approximate boundary of the most prominent structures. The white numbers are the corresponding ω values.

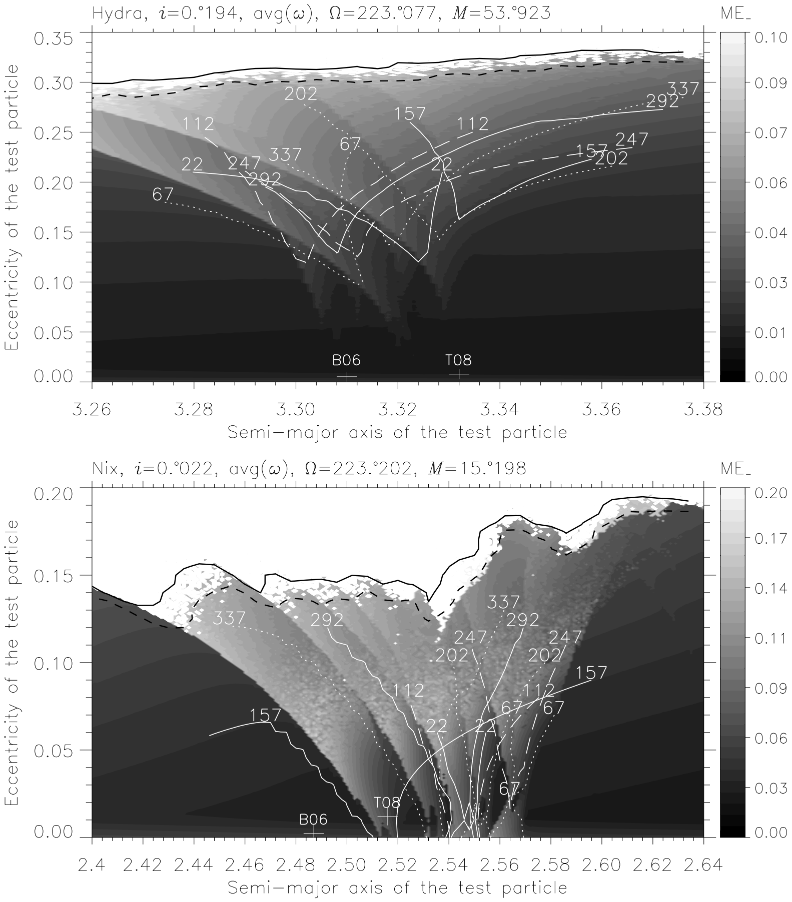

Figure 1: *The* $(a-e)$ *stability map for 8* ω *values for Hydra (upper) and Nix (lower). The white curves correspond to contour lines indicating the shape of the resonances as they would appear on individual maps for the* ω *displayed at the upper end of the curves. In the upper panel along the contour curves* $\mathrm{ME}_- = 0.025$*. In the case of Hydra along the contour curves* $\mathrm{ME}_- = 0.04$.

4.1 Mass parameter

We performed two different runs to estimate the effect of the different values of the mass parameter used by Nagy et al. (2006) and by T08. The structures for the two mass parameter are almost identical, for $\mu = 0.104424$ they are only shifted along the horizontal axis. This is a consequence of the changes in the coordinates of the barycenter. This shift could be important in the close vicinity of mean motion resonances.

4.2 Charon's eccentricity

In order to visualise the effect of the absence of the Jacobi-integral, we plotted also the circular and the elliptic case for both moons. The differences are: in the elliptic case the unstable zone is much larger and the center of the resonance is shifted to larger semi-major axis, and the 4:1 and 6:1 resonances became stronger for low eccentricities. The V-shape did not change significantly.

4.3 The stability maps

We investigated the orbits systematically by changing the initial orbital elements of the test particle. In Figure 1, the results are summarized for the 8 values of ω. The figure is dominated by a V-shaped gray structures, corresponding to the 4:1 mean motion resonance between Charon and Nix. These resonances can represent either ordered or weakly chaotic behaviour. The present positions of the moons are in stable region both on the $(a - e)$ and $(a - i)$ parameter spaces. On the maps the structures related to the 4:1 and 6:1 resonances are clearly visible, but none of them contains any of the moons. As you can see in Figure 1, in the case of $\omega = 157.9$ for Nix it can show the possibility of active resonance. But for Hydra we can not find any value, where the 6:1 resonance would appear, since it is very weak in the vicinity of the moon. The $\omega = 67$ seems the most strongest, because it approaches the axis the most, in this case the value of eccentricity goes underneath 0.05. Since the eccentricity is really small, it is hard to establish the ω values. More accurate orbit solutions could result in such data, that places the Nix in resonance. The $(a - i)$ maps give the same results. Mention must be made that the planar and spatial cases are almost identical, when the inclinations are very small (as they are for the moons).

4.4 Results using the general problem

Newly we started to investigate the system using the framework of the general four-body problem. The masses and their error limits were from work of T08. Using the maximal margin of error, our initial results show that the moons are on orbits those very hard to estimate for larger time. First we calculated the well-known Lyapunov-time (T_L). The Lyapunov time reflects the limits of the predictability of the system. By convention, it is measured as the time for nearby trajectories of the system to diverge by e (Euler-number). We found that for the new moons $T_L = 20$ day. Since the 'New Horizons' mission will reach and study the system in 2015 (Stern 2002), it is very relevant to know the precise positions of the system's members. This claims further investigations which are under way. Another plan is to calculate the resonant arguments for different orbits. These preliminary results are that there are no evidences of resonance in the measured positions of the moons. Accurate positions are needed to be measured to find an evidence of resonance.

Acknowledgement

The European Union and the European Social Fund have provided financial support to the project under the grant agreement no. TÁMOP-4.2.1/B-09/1/KMR-2010-0003.

References

Benettin, G., Vecchio, G.L., Tenenbaum, A. 1980, Phys. Rev. A, 22, 1709

Buie, M.W., Grundy, W.M., Young, E.F., Young, L.A. Stern, S.A. 2006 The Astr. J., 132, 290

Christy, J.W., Harrington, R.S. 1978, The Astr. J., 83, 1005

Dvorak, R., Pilat-Lohinger, E., Funk, B., Freistetter, F. 2003 Astr. & Astroph, 398, L1

Froeschlé, Cl. 1984 Cel. Mech., 34, 95

Nagy, I., Süli, Á., Érdi, B. 2006 MNRAS, 370, L19

Sándor, Zs., Süli, Á., Érdi, B., Pilat-Lohinger, E., Dvorak, R. 2006 MNRAS, 375, 1495

Süli, Á., Dvorak, R., Freistetter, F. 2005, MNRAS, 363, 241

Süli, Á., Zsigmond, Zs. 2009, MNRAS, 398, 2199

Stern, A., Cheng, A. 2002, 34th COSPAR Scientific Assembly The Second World Space Congress Houston, USA

Tholen, D.J., Buie, M.W., Grundy, W.M., Elliott, G.T. 2008, The Astr. J., 135, 777

Weaver, H.A. et al. 2005, IAU Circular, 8625

Weaver, H.A. et al. 2006, Nature, 439, 943

Part Two

Exoplanetary Systems

PADEU | PADEU **20**, 83 (2011)
ISBN 963 463 557

TRANSIT TIMING VARIATIONS IN ECCENTRIC HIERARCHICAL TRIPLE EXOPLANETARY SYSTEMS

Tamás Borkovits[1] **and Szilárd Csizmadia**[2]

[1] Baja Astronomical Observatory of Bács-Kiskun County, H-6500 Baja, Szegedi út, Kt. 766, Hungary
[2] Deutsches Zentrum für Luft- und Raumfahrt (DLR), Institut für Planetenforschung, Rutherfordstr. 2, 12489 Berlin, Germany

E-mail: [1]`borko@electra.bajaobs.hu`, [2]`szilard.csizmadia@dlr.de`

Abstract

The moments of the mid-transit times of a transiting exoplanet will deviate from a linear ephemeris due to mutual gravitational perturbations caused by a distant third companion (e.g. a planet, a brown dwarf or a star). Beyond this so-called transit timing variation (TTV), the duration as well as the depth of the consecutive transits can be varied, too. We investigate the motion of a transiting exoplanet perturbed by a third object, assuming that the planet is far enough from its host star that the tidal effects are negligible. We give direct analytical form of the TTV for this case and we study how it depends on different kind of dynamical and geometrical orbital elements. We carried out several numerical integrations which show that the analytical formula is well applicable in systems with extremely large eccentricity (even for $e > 0.9$), too. As an application, we illustrate how the formulae work for the weakly eccentric CoRoT-9b, and the highly eccentric HD 80606b. Finally, we illustrate the operation and effectiveness of Kozai cycles with tidal friction in the case of HD 80606b.

Keywords: *exoplanets – transit timing variations – CoRoT-9b – HD 80606b*

1 Introduction

The rapidly increasing number of exoplanetary systems, as well as the lengthening time interval of the observations naturally leads to the search for perturbations in the motion of the known planets which can give possibility to detect further planetary (or stellar) components in a given system, and/or can produce further information about the oblateness of the host star (or the planet), or even might refer to evolutionary effects.

The detection and the interpretation of such perturbations in the orbital revolution of the exoplanets usually depends on the TTV. Plotting the observed minus calculated mid-transit times with respect the cycle numbers we get the $O-C$ diagram which having been the main tool for period studies by the variable star observers (not only for eclipsing binaries) for more than a century. Consequently, the effect of the various types of period variations (being real or apparent ones) for the $O-C$ diagram were already wide-spreadly studied in the last one hundred years. Some of them are less relevant in the case of transiting exoplanets, but others are important. For example, the two classical ones are the simple geometrical light-time effect (LITE) (due to a further, distant companion), and the apsidal motion effect (due to both the stellar oblateness in eccentric binaries, and the relativistic effect).

The continuous long-term monitoring of several hundreds of stars with the CoRoT and Kepler satellites, as well as the long-term systematic terrestrial surveys give the excellent opportunity to discover transiting exoplanets (or as by-products: eclipsing binaries) with the period of months. Then continuous, long-term transit monitoring of such systems (combining the data with spectroscopy) give chance to detect the traces of dynamical evolutionary effects (i. e. orbital shrinking) already on the timescale of some decades. Furthermore, the larger the characteristic size of a multiple planetary, stellar (or mixed) system the greater the amplitude even the shorter period perturbations in the TTVs, as was shown in details in the discussion of Borkovits et al. (2003).

In the last years several papers were published in the topic of TTVs, both from theoretical aspects e.g. (without completeness) Agol et al. (2005); Holman & Murray (2005); Holman (2010); Cabrera (2010); Fabrycky (2010); and see further references thereins, and from observational aspects for individual transiting exoplanetary systems which papers now are so copious that we cannot list them. Nevertheless, most (but not all) of the theoretical papers above, mainly concentrate on simply the detectibility of further companions (especially super-Earths) from the TTVs.

In this paper we consider this question in greater details. We calculate the analytical form of the long-period (i. e. with a period in the order of the orbital period of the ternary component P_2) time-scale perturbations of the $O-C$ diagram for hierarchical (i.e. $P_2 >> P_1$) triple systems. (Note, as we mainly concentrated on transiting systems with a period of weeks or months, we omitted the possible tidal forces. However, our formulae practically can be applied even for the closest exoplanetary systems, too, because the tidal perturbations become effective usually on a notably longer time-scale.) This work is a continuation and extension of the previous paper of Borkovits et al. (2003). In that paper we formulated the long-period perturbations of an (arbitrarily eccentric and inclined) distant companion to the $O-C$ diagram for a circular inner orbit. (Note, that our formula is a generalized variation (in the relative inclination) of the one of Agol et al. (2005). For coplanar case the two results become identical.) Now we extend the results for the case of an eccentric inner binary (formed either a host-star with its planet, or two stars). As it will be shown, our formulae have a satisfactory accuracy even for such a high eccentricity, than $e_1 = 0.9$. Note, that in the period regime of some months the tidal forces are ineffective, so we expect eccentric orbits. This is especially valid in the case of the predecessor systems of hot-Jupiters, in which case some of the formation theories predict very high eccentricities.

In the next section we give a very brief summary of our calculations. (A somewhat detailed description can be found in Borkovits et al. (2003), Borkovits et al. (2007).) In Section. 2. we discuss our results, while in Section. 3 we illustrate the results with both analytical and numerical calculations on two individual systems, CoRoT-9b and HD 80606b.

2 Analytical investigations

As is well-known, at the moment of the mid-transit (which in case of an eccentric orbit usually does not coincide with the half-time of the whole transit event)

$$u \approx \pm\frac{\pi}{2} + 2k\pi, \tag{1}$$

where u is the true longitude measured from the intersection of the orbital plane and the plane of sky, and k is an integer. Due to its key role in the occurrence of the transits, instead of the usual variables, we use u as our independent time-like variable. It is known from the textbooks of celestial mechanics, that

$$\dot{u} \approx \mu^{1/2}a^{-3/2}(1-e^2)^{-3/2}(1+e\cos v)^2 - \dot{\Omega}\cos i, \tag{2}$$

consequently, the moment of the N-th primary minimum (transit) after an epoch t_0 can be calculated as

$$\int_{t_0}^{t_N} \mathrm{d}t = \int \frac{a^{3/2}}{\mu^{1/2}} \frac{(1-e^2)^{3/2}}{[1+e\cos(u-\omega)]^2} \left(1+\frac{\rho_1^2}{c_1}\dot{\Omega}\cos i\right) \mathrm{d}u. \tag{3}$$

In order to evaluate Eq. (3) first we have to express the perturbations in the orbital elements with respect to u. As far as we consider all the orbital elements (except of u) as constant, for the first term of the right hand side yield the following closed solution

$$\overline{P}_{I,II}{=}\frac{P}{2\pi}\left[2\mathrm{arctan}\left(\sqrt{\frac{1-e}{1+e}}\frac{\mp\cos\omega}{1\mp\sin\omega}\right)\pm(1-e^2)^{1/2}\frac{e\cos\omega}{1\mp e\sin\omega}\right],$$

for the two types of minima, respectively. (Here P denotes the anomalistic or Keplerian period which is considered to be constant.) Note, that instead of the exact forms above, naturally its expansion is used widely (as in this paper).

As a next step, we have to calculate the long-period and apse-node perturbations in u. A part of them practically come simply from the similar perturbations of the orbital elements (or directly of the $e\cos\omega$, $e\sin\omega$ functions), while others (we will refer them as direct perturbations in u) comes from the variations of the mean motion, i.e. with other words this means that in that case P no longer will be constant.

Averaging the perturbation equations for the short-period variable (u) we get the long-period ($\sim P_2$) variations of the orbital elements, and consequently, we get the analytical form of the long-period contribution of $O-C$. This can be written into the following two different forms:

$$\begin{aligned} O-C_{\mathrm{dyn}} &\approx \frac{P_1}{2\pi}\frac{A_{\mathrm{L}}}{\left(1-e_2^2\right)^{3/2}}\left[A_{\mathcal{M}}\mathcal{M}+A_{\mathcal{S}}\mathcal{S}\right], && (4)\\ &\approx \frac{P_1}{2\pi}A_{\mathrm{L}}\sum_n A_n\sin(nv_2+\phi_n), && (5) \end{aligned}$$

where the amplitudes are

$$\begin{aligned} A_{\mathrm{L}} &= \frac{15}{8}\frac{m_3}{m_1+m_2+m_3}\frac{P_1}{P_2}, && (6)\\ A_{\mathcal{M},\mathcal{S}} &= A_{\mathcal{M},\mathcal{S}}(e_1,g_1,\omega_1,i_{\mathrm{m}}), && (7)\\ A_{1,2,3} &= A_{1,2,3}(e_1,g_1,\omega_1,i_{\mathrm{m}};e_2,g_2), && (8)\\ A_{4,\ldots} &= A_{4,\ldots}(e_1,g_1,\omega_1,i_{\mathrm{m}};e_2), && (9) \end{aligned}$$

while for the phase-terms

$$\begin{aligned} \phi,\, \phi_1 &= \phi,\, \phi_1(e_1, g_1, \omega_1, i_\mathrm{m}; g_2), && (10)\\ \phi_{2,3} &= \phi_{2,3}(e_1, g_1, \omega_1, i_\mathrm{m}; e_2, g_2), && (11)\\ \phi_{4,\ldots} &= 0 + (0,1) \times \pi, && (12) \end{aligned}$$

and, furthermore,

$$\begin{aligned} \mathcal{M} &= \frac{1}{3}\left(v_2 - l_2 + e_2 \sin v_2\right), && (13)\\ \mathcal{S} &= \sin(2v_2 + \phi) + e_2 \sin(v_2 + \phi) + \frac{1}{3} e_2 \sin(3v_2 + \phi). && (14) \end{aligned}$$

Moreover, the pure geometric light-time effect gives a further contribution, as

$$O - C_\mathrm{LITE} = -\frac{m_3}{m_{123}} \frac{a_2 \sin i_2}{c} \frac{\left(1 - e_2^2\right) \sin(v_2 + \omega_2)}{1 + e_2 \cos v_2}, \qquad (15)$$

and its amplitude is

$$\begin{aligned} A_\mathrm{LITE} &= \frac{m_3}{m_{123}} \frac{a_2 \sin i_2}{c} \left(1 - e_2^2 \cos^2 \omega_2\right)^{1/2} \\ &\approx 1.1 \times 10^{-4} \frac{m_3}{m_{123}^{2/3}} \sin i_2 P_2^{2/3} \left(1 - e_2^2 \cos^2 \omega_2\right)^{1/2}, && (16) \end{aligned}$$

where masses are in solar mass, while P_2 is in days.

Note, the actual form of the above listed amplitude and phase terms (up to the sixth order in e_1 will be published very soon in Borkovits et al. (2010).

3 Discussion

The geometrical elements of the orbits, and the physical parameters, i.e. masses, and dimensions of the orbits (via periods and their ratios) are separated. Consequently, the properties of dynamical $O-C$ can be investigated independently from any particular system, the physical parameters form only a scaling parameter. We found, that the amplitudes above generally remain in one order of magnitude for a wide range of the orbital parameters. Furthermore, in case of a planet-mass third companion we can use the following simple, linear equation, $A_\mathrm{dyn} \approx \mathcal{A}\frac{m_3}{P_2}$, where $\mathcal{A} = \frac{1}{2\pi}\frac{P_1^2}{m_\mathrm{host-star}}$ is a known constant for any particular transiting planets.

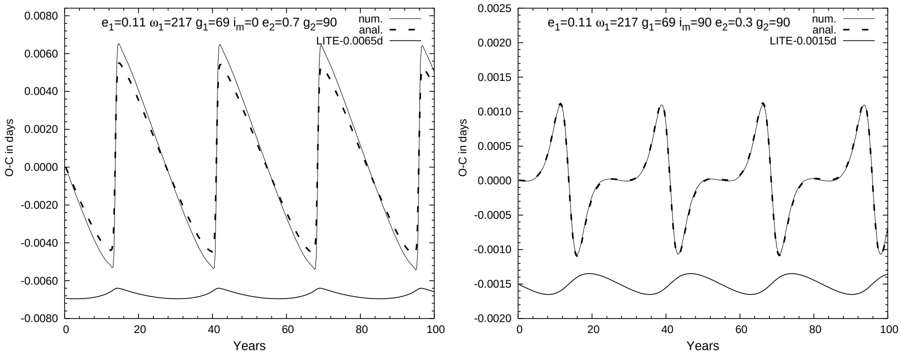

Figure 1: *Sample of TTVs caused by a hypothetical* $P_2 = 10\,000$ *day-period* $5\ M_J$ *mass third component for CoRoT-9b, at specific orbital parameters. (The pure, geometrical light-time contribution plotted also separately, below the combined curve.)*

Comparing the LITE amplitude to the dynamical one, keeping P_1 as constant, and increasing P_2, the $A_{\mathrm{LITE}}/A_{\mathrm{dyn}}$ ratio increases by $P_2^{5/3}$, i.e. for relatively more distant systems LITE tends to exceed the dynamical effect. Usually this is the case in almost the known eclipsing hierarchical triple stellar systems, but we can expect an opposite situation in many of the recently discovered transiting exoplanetary systems.

The $A_{\mathcal{M},\mathcal{S}}$ amplitudes depend only on the orbital elements of the transiting planet, with the exception of the mutual inclination (i_m) of the two orbits. Two of these four elements, namely inner eccentricity (e_1), and argument of periastron in the observational frame of reference (ω_1) can be determined from other sources (e.g. from radial velocity, as well as light-curves). Consequently, for a specific system only two parameters remain, the argument of periastron in the dynamical frame of reference (g_1), and the mutual inclination (i_m). Consequently, the expectable properties of the dynamical $O-C$ can be mapped easily, independently from the properties of the third body's orbit. Furthermore note, that for circular third orbit $A_2 = A_{\mathcal{S}}$, and for any other n-s $A_n = 0$, so, for not too highly eccentric third orbit simply $A_{\mathcal{S}}$ contain almost all information on the dynamical $O - C$.

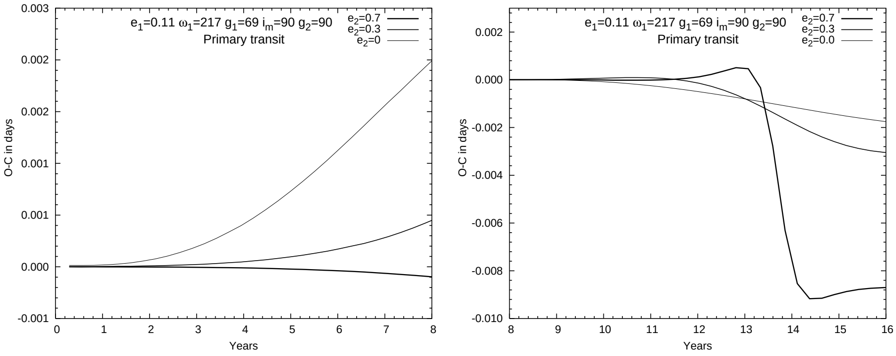

Figure 2: *The first and second 8 year-long intervals of some $O-C$ curves for CoRoT-9b. The medium thick line, denoted by $e_2 = 0.3$ belong to the curve shown in the right panel of Fig. 1. The other parameters are identical.*

4 Case studies

4.1 CoRoT-9b

CoRoT-9b is a transiting exoplanet which revolves around its Sun-like host star approx. in the distance of Mercury. Its important parameters from Deeg et al. (2010) are as follows: $m_1 = 0.99\,\mathrm{M}_\odot$, $m_2 = 0.0008\,\mathrm{M}_\odot$, $P_1 = 95.27$ d, $e_1 = 0.11$, $\omega_1 = 217^\mathrm{o}$, $i_1 = 89.99^\mathrm{o}$. According to the physical quantities, $\mathcal{A} \approx 1.39\ \mathrm{d}^2\mathrm{M}_\mathrm{J}^{-1}$, i.e. a Jupiter-mass further planet could produce 10^{-3} d half-amplitude variation already from the distance of Mars. Here we show the realization of some curves for different geometry of the third companion (Fig. 1). Note, we found a very specific case (which, for the limited space, is not shown here), i.e. at some specific relative orientations of the two orbits (g_1, g_2) the $O-C$ almost disappears around $i_\mathrm{m} \approx 45^\mathrm{o}$. Nevertheless, this is not typical. We illustrate also, that although the amplitude of the $O-C$ curve usually grows with the eccentricities (both inner and outer ones), the possible fastest detection of the dynamical perturbations from the $O-C$ strongly depends on the orbital phase of the outer perturber. As one can see in Fig. 2, we can find such configurations where the smaller full-amplitude variation can be detected much shorter. This is because the detection mainly depends on the actual curvature of an $O-C$ curve.

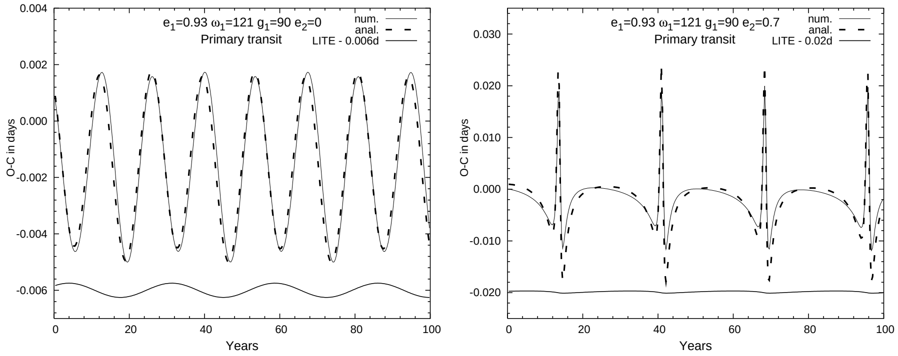

Figure 3: *Sample of TTVs caused by a hypothetical* $P_2 = 10\,000$ *day-period* $5\ M_J$ *mass third component for HD 80606b, at the maximum eccentricity phase of the induced Kozai-cycles.*

4.2 HD 80606b

The high-mass gas giant exoplanet HD 80606b revolving on an almost 4-month long period, extremely eccentric orbit around its solar-type host-star, was discovered by Naef et al. (2001) via radial velocity measurements. Recently both secondary occultation (with Spitzer space telescope, Laughlin et al. (2009)), and primary transit (Moutou et al. (2009); Fossey et al. (2009)) were detected. A thorough analysis of the collected data around the February 2009 primary transit led to the conclusion, that there is a significant spin-orbit misalignment in the system, i.e. the orbital plane of HD 80606b fails to coincide with the equatorial plane of its host star (Pont et al. (2009)). This result makes it plausible that we can observe this planet near the maximum eccentricity phase of a Kozai cycle induced by a distant, inclined third companion. In the maximum eccentricity phase for a wide range of the initial parameters $i_\mathrm{m} \approx 39.23^\mathrm{o}$, and $2g_1 = 180^\mathrm{o}$. We fixed this values, which together the spectroscopic $e_1 = 0.93$ and $\omega_1 = 121^\mathrm{o}$ makes the $A_{\mathcal{M},\mathcal{S}}$ amplitudes completely determined. Two of the $O-C$-s calculated such a way is plotted in Fig. 3. This illustrates, that our analytical formula (calculated up to sixth order in inner eccentricity) works relatively well even for such a high eccentricity, too. In Fig. 4 we show also the numerically integrated dynamical evolution of the system for 100 and 1 million years with and without tidal dissipation. The Q-parameters

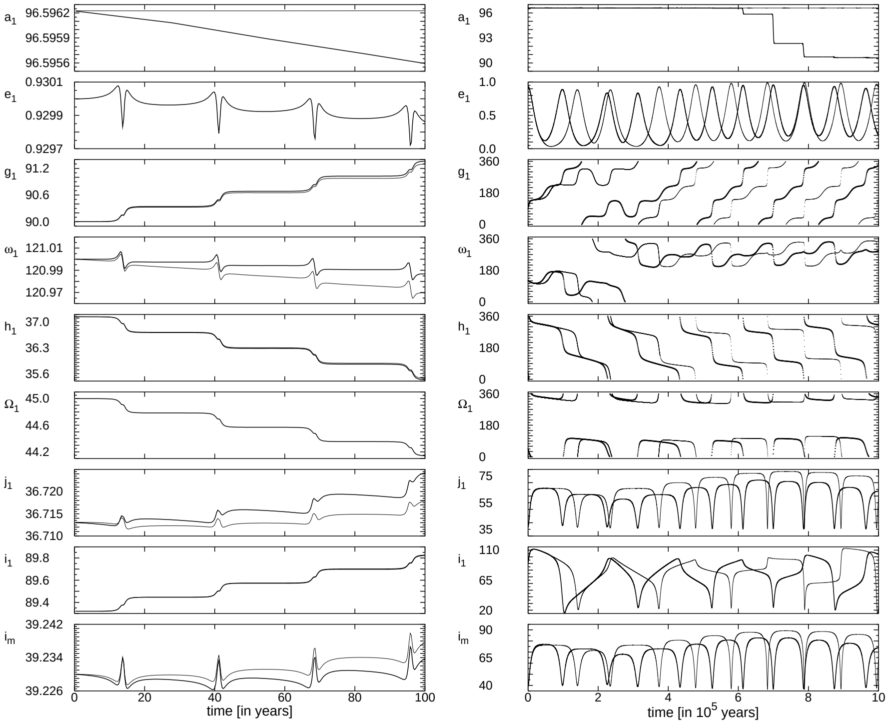

Figure 4: *Dynamical evolution of the orbital elements of HD 80606b in the presence of a hypothetical* $P_2 = 10\,000$ *day-period, 5* M_J *mass third companion. Thick curves: tidal effects and dissipation are considered; thin curves: three-mass-point model. (Relativistic contributions are omitted.) Note, semi-major axis* (a_1) *is given in* $R_\odot$.

were set to $Q_1 \approx 4.1 \times 10^7$, and $Q_2 \approx 1.7 \times 10^4$, for the host star, and its inner planet, respectively. The period variation caused by the orbital shrinking is $\Delta P_1 \approx 3 \times 10^{-6}\,\mathrm{day\,cycle}^{-1}$, which would produce 10^{-3} days departure in transit times during ~ 26 cycles, i.e. ~ 8 years.

References

Agol, E., Steffen, J., Sari, R., & Clarkson, W., 2005, MNRAS, 359, 567

Borkovits, T., Érdi, B., Forgács-Dajka, E., & Kovács, T., 2003, A&A, 398, 1091

Borkovits, T., Forgács-Dajka, E., & Regály, Zs., 2007, A&A, 473, 191

Borkovits, T., Csizmadia, Sz., Forgács-Dajka, E., & Hegedüs, T., 2010, A&A, to be submitted

Cabrera, J. 2010, EAS Publ. Ser. 42, 109

Deeg, H. J., Moutou, C., Erikson, A., Csizmadia, Sz., Tingley, B. et al. 2010, Nature, 464, 384

Fabrycky, D., 2010, arXiv:1006.3834

Fossey, S. J., Waldman, I. P., & Kipping, D. M. 2009, MNRAS, 369, L16

Holman, M.J., 2010, EAS Publ. Ser. 42, 39

Holman, M.J., & Murray, N.W., 2005, Science, 307, 1288

Laughlin, G., Deming, D., Langton, J., et al. 2009, Nature, 457, 562

Moutou, C., Hebrard, G., Bouchy, F., et al. 2009, A&A, 498, L5

Naef, D., Latham, D. W., Mayor, M., et al. 2001, A&A, 375, L27

Pont, F., Hébrard, G., Irwin, J. M., et al. 2009, A&A, 502, 695

PADEU | PADEU **20**, 93 (2011)
ISBN 963 463 557
© Published by the Astron. Dept. of the Eötvös Univ.

Habitability of planetary systems with two giant planets

Vera Dobos[1], Imre Nagy[2] and Judit Orgoványi[1]

[1]Eötvös University, Department of Astronomy, H-1518 Budapest, Pf. 32, Hungary
[2]MTA Research Group for Physical Geodesy and Geodynamics Műegyetem rakpart 3, 1111 Budapest, Hungary

E-mail: `vera.zs.dobos@gmail.com`

Abstract
Hypothetical planetary systems similar to our Solar System were studied in order to get a closer insight of habitability. The investigated systems consist of three inner rocky planets (Venus, Earth, Mars) and two outer gas giants. The stability of the orbits of the inner planets is discussed in the cases of different masses of the gas planets. It was found that Jupiter could be four times and Saturn could be three times more massive while the orbits of the inner planets stay stable. Similar calculations were made by changing the mass of the Sun. In this case the position of the rocky planets and the extension of the liquid water habitable and the UV habitable zones were studied for different masses of the Sun. It was found that the orbits of the planets were stable for values greater than 0.33 $M_\odot$ where $M_\odot$ is the mass of the Sun and at lower masses of the Sun (at about 0.8 $M_\odot$) only Venus, but for higher mass values (at about 1.2 $M_\odot$) Earth and also Mars are located in both habitable zones.

Keywords: *Exoplanets – habitable zone*

1 Introduction

New planetary systems containing one or more gas giants are discovered day by day. Present instruments and methods are, however, not ideal for detecting rocky planets, hence these discoveries are considered to be rare events. As instruments are getting more and more developed the number of known terrestrial-mass planets is expected to grow significantly.

Search for extraterrestrial life is also one of the main goals of ESA and NASA. New interferometers of these space agencies are to be launched in the next decade with the aim of discovering and characterizing new Earth-like planets. Therefore it is important to investigate the conditions within which the orbits of these planets are stable in the given system. Besides the dynamical stability, spectral distribution of the radiation of the central star also affects habitability of the system.

What would be the outcome in terms of the stability of the Solar System, if the masses of Jupiter and Saturn had been formed in a different way from the cloud envelope of the protostellar Sun? Is the Solar System unique? In this work we discuss different cases similar to the Solar System to investigate the conditions of habitability on rocky planets.

Our research program consists of two main parts. In the first part the stability of the rocky planets is investigated as a function of the masses of the gas giants and as a function of the mass of the Sun. This latter case is closely related to the second part of our work which is the calculation of the extension of the two kinds of habitable zones: the conventional liquid water habitable zone and the ultraviolet habitable zone.

2 Stability calculations

The studied planetary systems are built up from three inner rocky planets: Venus, Earth, Mars and two outer gas giants: P_1 and P_2, where P_1 is closer while P_2 is located farther from the Sun. M_1 and M_2 are the masses of P_1 and P_2, respectively. By changing the masses of the gas giants from 0 to 10 M_J where M_J is the mass of Jupiter the integration was made for 5000 P_S (P_S: period of Saturn) which is about 150000 years. Initial orbital elements were obtained for J.D. = 2415020.0 epoch where P_1 and P_2 were chosen for the parameters of Jupiter and Saturn, respectively. Stability of the inner planets is described by the maximum of eccentricities and close encounters. For the latter we investigated several parameters but finally chose the difference between the distance of the outer planet's pericentre and the distance of the inner planet's apocentre.

In the other case the planets' masses were constants and the mass of the Sun was altered between 0.1 $M_\odot$ and 10 $M_\odot$ where $M_\odot$ is the mass of the Sun. The integration time was the same as in the previous case that is 5000 P_S.

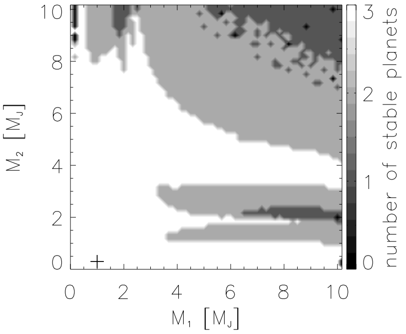

Figure 1: *Stability maps for the three inner planets in function of the masses of* M_1 *(axis x) and* M_2 *(axis y). The '+' mark indicates our Solar System. Colours indicate the number of stable planets: white - three, light gray - two, dark gray - one, black - zero.*

The stability was characterized by the pericentre and apocentre of the planets and both habitable zones were calculated for a few masses. For the latter the radius of the star was calculated from its mass using the formula constructed by Zaninetti (2008).

Stability is investigated by calculating the extrema of the orbital elements (semi-major axis, eccentricity, pericentre and apocentre distance). The planet is considered stable if the difference between its maximum and original eccentricity is less than 0.2. Fig. 1 shows the number of stable inner planets in function of the masses of the giant planets. Axis x corresponds to the mass M_1 while axis y to the mass M_2 (both in units of M_J). White colour means that all three planets are considered stable according to the above criterion while black indicates unstable regions (when all three planets are unstable). One can see the '+' mark at coordinates (1, 1/3) which corresponds to one Jupiter and one Saturn mass, so this is the case of our Solar System. The white region has a very large extension which means that the orbits of the inner planets are stable for a wide variety of the pairs of the gas giants.

Stability is not only determined by maximum eccentricities, but close encounters were also examined. To characterize the vicinity of neighbouring rocky planets the difference between the locations of these planets was calculated at every integration step. From these values the smallest was chosen as a measure of the encounter (D). To get comparable results for the two planet pairs (*Venus*

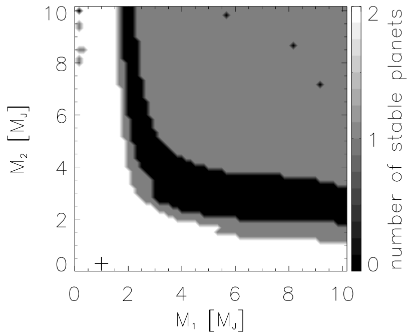

Figure 2: *Stability map by close encounters. Colours indicate the number of stable planet pairs: white - two, gray - one, black - zero. The '+' mark indicates our Solar System.*

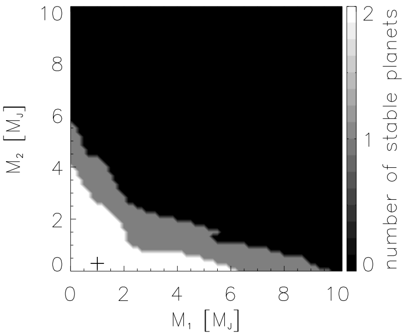

Figure 3: *Stability map made from the difference between the minimum pericentre of the outer planet and the maximum apocentre of the inner planet. Colours indicate the number of stable planet pairs.*

– *Earth* and *Earth – Mars*) these values were normalized by the mean of the original semi-major axes:

$$D = \frac{\texttt{min\{encounters\}}}{\frac{a_1+a_2}{2}},$$

where a_1 and a_2 are the semi-major axes of the closer and the farther planet from the Sun. The planet pair is considered stable if the ratio of the value of the encounter and the mean of the original semi-major axes is greater than 0.2. In Fig. 2 the number of stable planet pairs can be seen. White and black colours indicate the case when both and neither planet pairs are stable, respectively. To characterize the vicinity of the orbits of neighbouring rocky planets the difference between the outer planet's minimum pericentre distance and the inner planet's maximum apocentre distance was calculated as well. The orbits of the planet pairs are considered stable if the ratio of the difference mentioned above and the mean of original semi-major axes is greater than 0.01 (i.e. the planets come very close to each-other). In Fig. 3 the number of planet pairs with stable orbits can be seen. This is the worst case that can be imagined, when the outer and the inner planets are located in their pericentre

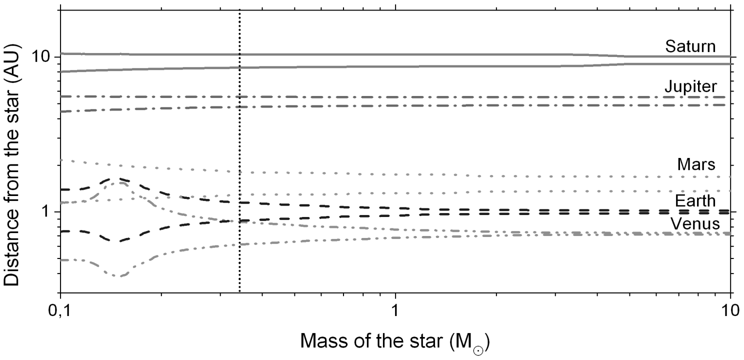

Figure 4: *The minimum pericentres and the maximum apocentres of the planets in function of the mass of the star. Different style of lines indicate different planets. The vertical spotted line at 0.33* $M_\odot$ *is a limit for the stability: for lower mass values the orbits of the planets are considered unstable and for greater values the orbits are considered stable.*

and apocentre, respectively, and these points and the Sun lie in a line. This may occur but the most probable case may be somewhere between the cases depicted in Fig. 2 and Fig. 3. In Fig. 3 white colour indicates that the orbits are surely stable while in Fig. 2 it indicates that they may be stable. Even in the worst case the stable (white) region is considerably large, hence Jupiter could be four times and Saturn could be three times more massive while the orbits of the inner planets stay stable.

The other problem that was investigated is also related to the stability of the inner planets but in this case the masses of the gas giants were constants while the mass of the Sun was altered between 0.1 $M_\odot$ and 10 $M_\odot$. The minimum pericentre and the maximum apocentre distances of the planets are plotted in Fig. 4 in function of the mass of the Sun. At low star masses the orbits of the inner planets can overlap each-other, hence two or even all three planets can encounter. From 0.33 $M_\odot$ (vertical spotted line on the figure) the orbits of the planets are considered stable regarding to the above-mentioned criterion (i.e. the ratio of the value of the encounter and the mean of the original semi-major axes of Venus and Earth is greater than 0.01).

In order to better understand the feature of habitability the two kinds of habitable zones were calculated. The results of these investigations are to be thoroughly discussed in the next chapter.

3 Habitable zones

The liquid water habitable zone (LW HZ) is a region around a star in which an Earth-like planet could support liquid water on its surface (Kasting et al. , 1993). In the equation that describes the boundaries of the LW HZ the Solar system the Earth is used as a reference for the calculations of other planetary systems.

An idea from Buccino et al. (2006) was borrowed that there must be both an inner and an outer boundary for sufficient and necessary UV radiation level respectively (UV HZ). It is well known that this radiation induces DNA[1] damage (especially UVB and UVC), inhibits photosynthesis (UVA) and causes lesion in a wide variety of proteins and lipids (Cockell , 1998). The action spectrum $B(\lambda)$ is commonly used as a measure of damage, quantifying the injurious effects of the UV radiation on the biological processes in function of the wavelength (Coohill , 1991; Horneck , 1995; Cockell , 1998). The action spectrum is determined by exponential functions given by Modos et al. (1999) who measured the spectrum by different dosimeters. The results of uracil dosimeter were chosen for the calculations as uracil is a compound that can be found within the RNA[2].

The biological effective spectrum for each value of wavelength can be obtained by multiplying the action spectrum with the incident radiation. To get a tractable expression for the calculation of the inner boundary, the Earth was used again as a reference. This way the following inequality was obtained:

$$\frac{d_{inner}^2}{d_\oplus^2} \geq \frac{\int\limits_{200nm}^{400nm} B(\lambda) \cdot R_*^2 \cdot E_*(\lambda)\, d\lambda}{x \cdot \int\limits_{200nm}^{400nm} B(\lambda) \cdot R_\odot^2 \cdot E_\odot(\lambda)\, d\lambda}, \tag{1}$$

where d_{inner} and $d_\oplus$ are the distances of the inner boundary and that of the Earth, R is the radius and $E(\lambda)$ is the emitted energy of the star and of the Sun at λ wavelength and x is the multiplicator of the terrestrial UV radiation that still can be tolerated by DNA, proteins and photosynthetic process. In other

---

[1] The deoxyribonucleic acid (DNA) contains the genetic instructions used in the development and functioning of all known living organisms.

[2] The ribonucleic acid (RNA) conveys genetic information and catalyzes important biochemical reactions.

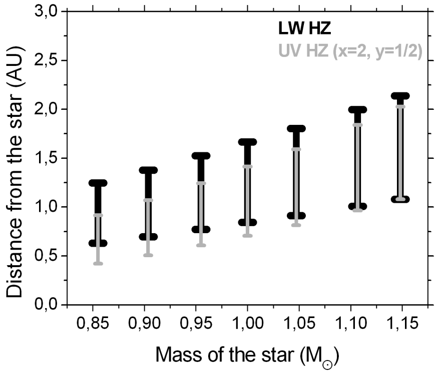

Figure 5: *The extension of the habitable zones in function of the mass of the star. Black and gray lines indicate the conventional and the UV habitable zone (x = 2, y = 1/2), respectively.*

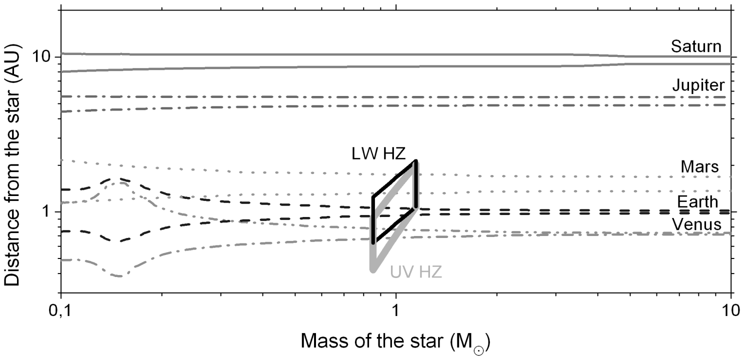

Figure 6: *The minimum pericentres and the maximum apocentres of the planets like in Fig. 4. Between 0.8 and 1.2 M$_\odot$ the extension of the habitable zones can be seen: black and light blue lines indicate the conventional and the UV habitable zone (x = 2, y = 1/2), respectively.*

words this means that these important compounds can bear even x times of the UV radiation on Earth.

On the other hand the UV radiation is an important energy source needed for chemical synthesis of complex molecules. An expression similar to Eq. (1) can be formulated to describe the outer boundary of the UV habitable zone:

$$\frac{d_{outer}^2}{d_{\oplus}^2} \leq \frac{\int\limits_{200nm}^{400nm} R_*^2 \cdot E_*(\lambda)\, d\lambda}{y \cdot \int\limits_{200nm}^{400nm} R_{\odot}^2 \cdot E_{\odot}(\lambda)\, d\lambda}, \tag{2}$$

where d_{outer} is the distance of the outer boundary and y is the multiplicator of the terrestrial UV radiation which is absolutely necessary for chemical reactions. Obviously y should be set to be less than 1.

The boundaries of habitable zones were calculated for seven values of mass in the $0.8 - 1.2\ M_{\odot}$ interval using the definition of the LW HZ given by Kasting et al. (1993) and equations (1) and (2) for the UV HZ. The values of x and y are difficult to estimate since different compounds and organisms have different level of tolerance (Cockell , 1998). For calculating the boundaries of the UV HZ $x = 2$ and $y = 1/2$ were used. The extension of both habitable zones for the seven masses of the star can be seen in Fig. 5. One can see that the UV HZ has a similar extension to the conventional HZ and they overlap each-other, but the UV HZ is located slightly closer to the Sun in the $0.8 - 1.2\ M_{\odot}$ interval. It can be seen that the Earth is located in both habitable zones even for lower and higher masses of the Sun.

For detailed results see Fig. 6, where black and gray colours indicate again the conventional and the UV ($x = 2$ and $y = 1/2$) habitable zones, respectively. At lower masses of the Sun only Venus, but for higher mass values Earth and also Mars are located in both HZ.

4 Summary

Stability of the orbits of the rocky planets was investigated for different masses of the two gas giants. The inner planetary system remained stable for several mass pairs, hence the fine-tune problem does not prevail. Yet, long-term investigation would be worthwhile because Batygin & Laughlin (2008) found that Mars can escape from the Solar System in $800 - 1200$ million years.

In the other case when the mass of the Sun was altered, the orbits of the planets were stable for values greater than $0.33\ M_{\odot}$. Between 0.8 and 1.2 AU the extensions of the two habitable zones were calculated and in almost all cases the Earth was located in both habitable zones. This result also suggests that the Solar System is not considered to be unique.

Acknowledgement

The European Union and the European Social Fund have provided financial support to the project under the grant agreement no. TÁMOP-4.2.1/B-09/1/KMR-2010-0003.

References

Batygin, K., Laughlin, G. 2008, ApJ 683, 1207

Buccino, A., Lemarchand, G., Mauas, P. 2006, Icarus 183, 491

Cockell, C. 1998, Theor. Biol. 193, 717

Coohill, T.P. 1991, Photochem. Photobiol., 54, 859

Horneck, G. 1995, J. Photochem. Photobiol. B: Biol. 31, 43

Kasting, J., Whitmire, D., Reynolds, R. 1993, Icarus 101, 108

Modos, K., Gáspar, S., Kirsch, P., Gay, M., Ronto, G. 1999, J. Photochem. Photobiol. B: Biol. 49, 171

Zaninetti, L. 2008, Serbian Astronomical Journal, 177, 73

PADEU PADEU **20**, 103 (2011)
ISBN 963 463 557
© Published by the Astron. Dept. of the Eötvös Univ.

Inclined orbits in the Habitable Zone of multiplanetary systems

Barbara Funk

Eötvös University, Department of Astronomy, H-1518 Budapest, Pf. 32, Hungary

E-mail: `funk@astro.univie.ac.at`

Abstract
Fifteen years after the first discovery of an extrasolar planet more than 450 are known. Most of them are massive gas giants like Jupiter due to the detection methods. Nevertheless more and more low-mass planets (Super-Earth) orbiting other stars were found with the help of various ground based and space missions (e.g. MOST, CoRoT, Kepler). The main goal of this work was an investigation of the dynamical stability of potential additional massless planets in nine nearby extrasolar multiplanetary systems. Although there exists many global stability studies, as well as detailed studies for some specific systems, up to now the influence of the inclination was not investigated in detail. All these investigations need extensive numerical integrations as well as sophisticated methods of analysis to study the stability of the orbits. The final output is a list of all systems indicating in which systems additional planets may be dynamically stable within the borders of the habitable zone. As well as a detailed description about the influence of highly inclined orbits on the dynamically stability.
Keywords: *dynamical astronomy, multiple exoplanetary systems, habitable zone*

1 Introduction

Since the discovery of the first extrasolar planet around a main-sequence star by Mayor & Queloz (1995) one of the primary goals of astronomers is the search of further extrasolar planetary systems (EPS). Today more than 450 extrasolar planets are known, but most of them are massive gas giants (GG) - mostly due to the detection methods. Thus in a next step scientists try to find terrestrial planets orbiting other stars. The detection of terrestrial planets is quite easier from space, than from the Earth. Therefore a lot of satellite missions, like MOST, CoRoT or Kepler have been or will be launched within the next years (for details see Fridlund (2008), ESA's and NASA's homepage).

Since most satellite missions can only observe a restricted sample of stars in a finite time span of operation it is quite important to choose this target systems very carefully. Up to now a major point of investigation, concerning extrasolar systems, is their dynamical stability when several planets or host stars (binaries) are involved. The literature on this type of studies is quite large and different groups are working on it. In our study we will concentrate on the dynamical stability of additional planets inside the habitable zone (HZ). A few EPSs were already investigated with special attention to their HZs (e.g. Gehman et al. (1996); Noble et al. (2002); Dvorak et al (2004); Schwarz et al. (2005); Menou & Tabachnik (2003); Schwarz et al. (2007); Érdi & Sándor (2005)).

The question of the existence of terrestrial planets in extrasolar planetary systems is a hot topic since the first discovery of planets outside our Solar system. One of the first studies was done by Jones et al. (2001), who investigated the stability of hypothetical additional planets in 4 known systems via numerical integrations (according to them Rho Vrb and 47 Uma could host additional terrestrial planets, Gliese 876 and Ups And were found to be unlikely to have additional planets in the HZ). Turnbull & Tarter (2003) applied Hill's definition of stability and compiled a catalogue of habitable systems for the SETI target selection. An extensive investigation was undertaken by Menou & Tabachnik (2003) concerning the orbital stability of terrestrial planets in all EPSs known at this time via numerical integrations. About half of the known systems turned out to possibly host additional planets in the HZs. Furthermore Jones et al. (2005) examined whether hypothetical terrestrial planets could stay long enough in the HZ to be able to develop a biosphere. By using the results of a detailed study of 7 systems as models, half of the investigated 111 systems were found to possibly host additional terrestrial planets.

The goal of this work is to investigate possible target systems, according to the Darwin All Sky Target Star Catalogue (DASSC) (see Kaltenegger et al. (2008)) of upcoming space missions. The DASSC contains about 75 systems in which at least one extrasolar planet have already been found. Among these systems we have investigated 9, which have two or more planets. Since such multiplanetary systems are extensively investigated, we focused our investigation on the influence of inclined orbits of the test-planets (TP) on the stability in the HZ, since the influence of inclined orbits on the stability is not well determined yet. Earlier theoretical studies (Funk et al. , 2009, 2010) have already shown, that highly inclined orbits ($i \approx 30^\circ - 40^\circ$) could - under certain circumstances - be very low eccentric and long term stable, which is one of the necessary conditions for habitability.

2 The dynamical model and the methods

In all cases, the motion of the planets will be considered in the framework of pure Newtonian forces and all the celestial bodies involved will be regarded as point masses. As a model we choose the restricted n-body problem, consisting of the star, the known planets and massless test planets within the HZ. For the TPs we will use a fine grid of initial conditions. We will vary the semi-major axis covering the complete HZ ($\Delta a = 0.01$ or 0.05 AU), but we will also perform computations with a certain range of initial inclinations ($0^\circ < i < 60^\circ$, $\Delta i = 5^\circ$) of the TPs. All initial conditions for the known planets are summarized in Table 1.

In order to study the dynamical evolution of extrasolar systems, efficient numerical integration methods are necessary. We used the Lie-Series Integration Method (Hanslmeier & Dvorak , 1984; Lichtenegger , 1984; Eggl & Dvorak , 2010) which is also capable of dealing with large eccentricities and close encounters between bodies. To analyze the data we used the maximum eccentricity method, which is a good tool for such investigations. It verifies the orbital eccentricities, which should not be too high to ensure that the distance to the host star and therefore the radiation on the TP does not change too much.

3 Results

In Fig. 1 we show the results of our calculations for all investigated systems. On the x-axis we plot the semi-major axes of the test-planets (covering the HZ) and on the y-axis there inclination. The color code corresponds to the maximum eccentricity values where red show low and violet high eccentricities. The name of the corresponding system is shown in the upper left corner of each plot. To estimate the amount of stable, low eccentric orbits we determined the percentage of orbits with maximum eccentricities below 0.2 for each system (results are given in Table 1, last column). Additional we give there also the total number of integrated orbits and the total amount of orbits with eccentricities

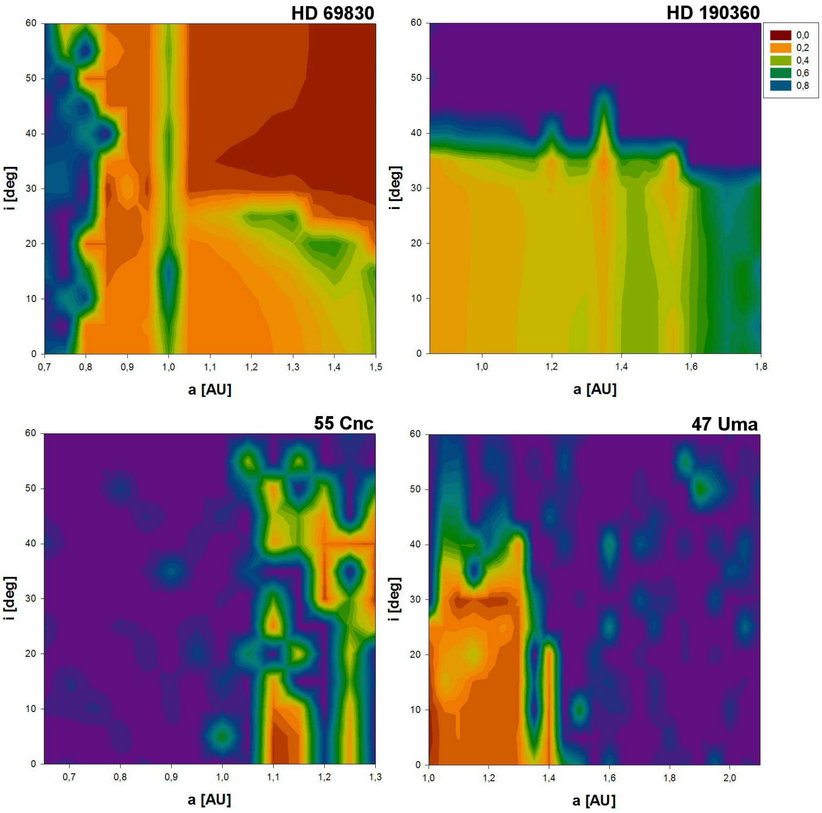

Figure 1: *Maximum eccentricity plots for all investigated systems: Upper left graph: HD 69830, upper right graph: HD 190360, lower left graph: 55 Cnc, lower right graph: 47 Uma. The inclination is plotted versus the semi-major axis of the test-planets. Red and orange corresponds to low eccentricity values, while dark blue and violet shows highly eccentric motion (see color code).*

Table 1: *Systems in the DASSC in which more than one planet has been found (multiple planetary systems). Columns 1 - 5 give the name of the system, informations about the host star and some orbital elements of the discovered planets. The number next to the systems name give the reference from which we took the orbital elements (1: Correia et al. (2010), 2: Mayor et al. (2009), 3: Lovis et al. (2006), 4: Vogt et al. (2010), 5: Fischer et al. (2008), 6: Pepe et al. (2010), 7: Mayor et al. (2009), 8: Gregory & Fischer (2010)). The last column gives the percentage of orbits with maximum eccentricities below 0.2 and in brackets the total number of orbits and the number of stable ones (for a detailed description see section 3).*

Name	SpType m [$M_\odot$]	a_{Planet} [AU]	e_{Planet}	m_{Planet} [M_{Jup}]	HZ [AU]	stable HZ? [%]
GJ 876 b	M4 V	0.208	0.025	1.935	0.14 - 0.28	0 (195-0)
GJ 876 c	0.32	0.13	0.27	0.560		
GJ 876 d^1		0.021	0	0.018		
GJ 581 b	M3	0.04	0	0.049	0.05 - 0.20	0 (208-0)
GJ 581 c	0.31	0.07	0.17	0.017		
GJ 581 d		0.22	0.38	0.022		
GJ 581 e^2		0.03	0	0.006		
HD 69830 b	K0 V	0.079	0.1	0.033	0.70 - 1.50	63 (221-140)
HD 69830 c	0.86	0.186	0.13	0.038		
HD 69830 d^3		0.63	0.07	0.058		
HD 128311 b	K0 V	1.099	0.25	2.180	0.50 - 1.05	0 (156-0)
HD 128311 c^4	0.84	1.76	0.17	3.210		
55 Cnc b	G8 V	0.115	0.014	0.824	0.65 - 1.30	11 (182-20)
55 Cnc c	0.94	0.24	0.086	0.169		
55 Cnc d		5.77	0.025	3.835		
55 Cnc e		0.038	0.07	0.034		
55 Cnc f^5		0.781	0.2	0.144		
HD 190360 b	G6 IV	3.92	0.36	1.502	0.85 - 1.80	1 (260-3)
HD 190360 c^4	0.96	0.128	0.01	0.057		
HD 160691 b	G3 IV-V	1.497	0.128	1.676	1.10 - 2.20	0 (299-0)
HD 160691 c	1.08	0.091	0.172	0.033		
HD 160691 d		0.921	0.067	0.522		
HD 160691 e^6		5.235	0.099	1.814		
HD 82943 b	G0	1.19	0.219	1.750	1.00 - 2.05	0 (286-0)
HD 82943 c^7	1.15	0.746	0.359	2.010		
47 Uma b	G0 V	2.1	0.032	2.530	1.00 - 2.10	17 (299-51)
47 Uma c	1.06	3.6	0.098	0.540		
47 Uma d^8		11.6	0.16	1.640		

below 0.2.

According to Table 1 it can be easily seen, that in 5 (GJ 876, GJ 581, HD 128311, HD 160691, HD 82943) of the investigated systems no additional planets can be expected within the borders of the HZ, because some of the known planets move inside or very close to the HZ and therefore will disturb any further planets. The other 4 show some quite interesting features, which we will discuss now in more detail:

- The system HD 69830 (Fig. 1 upper left) shows the largest stable region within the HZ. Furthermore the strong influence of the 1:2 mean motion resonance with the planet HD 69830 d is visible at 1 AU. Markable is also the very low-eccentric region around an inclination of approximately 35°. The arc-like structure in the lower right corner of the graph could be caused by the influence of a secular resonance. Similar structures have already been found by Pilat-Lohinger & Funk (2010) in the investigation of the stable region in the binary γ Cephei.

- In the system HD 190360 (Fig. 1 upper right) the stable region is still quite large, but the arising eccentricities are already higher (between 0.2 and 0.3). Additional one can see the stabilizing effect of the 4:1 (at 1.56 AU) and the 5:1 (at 1.34 AU) mean motion resonances with HD 190360 b.

- The systems 55 Cnc (Fig. 1 lower left) and 47 Uma (Fig. 1 lower right) show only very narrow stable regions inside the HZ. Particularly the system 55 Cnc has just a very small stable region for low inclinations around 1.1 AU (probably connected to the 5:3 mean motion resonance with the planet 55 Cnc f). Additional one can see a low eccentric region between 1.2 and 1.3 AU for higher ($30^\circ \leq i \leq 45^\circ$) inclinations. The system 47 Uma shows a quite stable region between 1.0 and 1.4 AU. Again one can see the perturbing influence of the 2:1 mean motion resonance with the planet 47 Uma b at 1.32 AU and a very low eccentric feature for an inclination of 30°.

3.1 The influence of the inclination

In all 4 cases one can find a region with lower eccentricities for high inclinations ($\approx$ between 30° and 40°). Since this low eccentric region have also been found in an earlier study by Funk et al. (2010), we investigated this region for two example systems (47 Uma and HD 190360) in more detail.

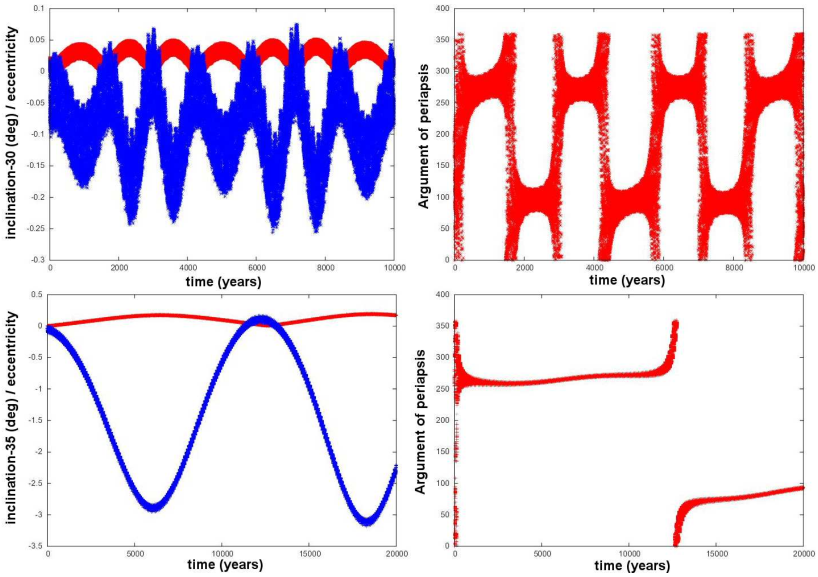

Figure 2: *The orbital elements e, i (left graphs) and* ω *(right graphs) of the systems 47 Uma (upper panels, a = 1.24 AU,* $i = 30°$*) and HD 190360 (lower panels, a = 1.36 AU,* $i = 35°$*). The eccentricity is given in red and the inclination in blue (For a better visibility we substracted here the initial inclination of* 30° *respectively* 35°*).*

Therefore we choose some single orbits in both systems. Fig. 2 shows the orbital elements (e, i, ω) of two of this orbits. In the upper line we give the results for an orbit in the HZ of the system 47 Uma and in the lower row for the system HD 190360. The initial conditions of both chosen orbits are summarized in Table 2.

Table 2: *Initial conditions for the two investigated orbits.*

System	a [AU]	e	i [◦]	ω [◦]	Ω [◦]	M [◦]
47 Uma	1.24	0	30	0	0	0
HD 190360	1.36	0	35	0	0	0

In Fig. 2 (upper left and lower left graph) we give the eccentricity (red) and the inclination (blue, note that we substracted the initial inclination of 30° respectively 35° for a better visibility) and in the upper right and lower right graph the argument of periastron (ω). For both orbits one can see, that the eccentricity and the inclination are coupled and that the argument of periastron circulates alternately around 90° and 270°. This behaviour, which shows similar characteristics like orbits in Kozai resonance, leads to very low eccentric long-term stable orbits for inclinations between approximately 30° and 40° (a detailed description in the restricted three body problem can be found in Funk et al. (2010)). Our study of TPs in multiplanetary systems showed, that this effect can still lead to low eccentric long-term stable orbits even if further perturbers (additional planets) are present. The presence of further planets just yields to a noise like structure in the orbital elements.

4 Conclusions

In the presented study we investigated the dynamical stability in the HZ of 9 multiplanetary systems, which are listed in the DASSC. Because almost all multiplanetary systems are already quite well investigated we focused our work on the influence of inclined orbits on the stability. Earlier studies have already shown, that highly inclined ($30° < i < 40°$) orbits could lead to low eccentric, long-term stable orbits.

Our investigations showed, that in 5 of the 9 systems no additional planets can move on regular orbits. Nevertheless it could be possible, that also in this systems some stable configurations (e.g. Moons or Trojan planets) might exist. We focused our further study on the 4 remaining systems, in which we could found at least some stable orbits. Within this 4 systems two (HD 69830 and HD 190360) show a quite large stable region in the HZ, while for the other two (55 Cnc and 47 Uma) just a relatively narrow stable region could be found. All 4 systems show the previous mentioned low eccentric region for inclinations between 30° and 40°

Thus in a next step we investigated exemplarily some single orbits in the systems 47 Uma and HD 190360. This test demonstrated, that orbits in the highly inclined, low eccentric region showed a coupling between the eccentricity and the inclination and the argument of periastron circulates alternately around 90° and 270°. Both behaviours have already been found in an earlier study in the restricted three body problem. So according to our results we can conclude, that this effect can lead to highly inclined, low eccentric, long-term stable orbits also if additional perturbers (planets) are present.

Acknowledgement

B. Funk wants to acknowledge the support by the Austrian FWF Erwin Schroedinger grant no. J2892-N16.

References

Correia, A.C.M., Couetdic, J., Laskar, J., Bonfils, X., Mayor, M., et al. 2010, A&A, 511, A21

Dvorak, R., Pilat-Lohinger, E., Schwarz, R, Freistetter, F. 2004, A&A, 426, L37

Eggl, S., Dvorak, R. 2010, LNP, 790, 431

Érdi, B., Sándor, Zs. 2005, CeMDA, 92, 113

Fischer, D.A., Marcy, G.W., Butler, R.P., Vogt, S.S., Laughlin, G., et al. 2008, ApJ, 675, 790

Fridlund, M.: 2008, Space Science Reviews, 355

Funk, B., Schwarz, R., Pilat-Lohinger, E., Süli, Á., Dvorak, R. 2009, P&SS, 57, 434

Funk, B., Libert, A.-S., Süli, Á., Pilat-Lohinger, E. 2011, A&A 526, A98

Gehman, C.S., Adams, F.C, Laughlin, G. 1996, PASP, 108, 1018

Gregory, P.C., Fischer, D.A. 2010, MNRAS, 403, 731

Hanslmeier, A., Dvorak, R. 1984, A&A, 132, 203

Jones, B.W., Sleep, P.N., Chambers J.E. 2001, A&A, 366, 254

Jones, B.W., Underwood, D.R., Sleep, P.N. 2005, ApJ, 622, 1091

Kaltenegger, L., Eiroa, C., Fridlund, M. 2008, submitted to A&A

Lichtenegger, H. 1984, CeMDA, 34, 357

Lovis, C., Mayor, M., Pepe, F., Alibert, Y., Benz, W., et al. 2006, Nature, 441, 305

Mayor, M., Queloz, D. 1995, Nature, 378, 355

Mayor, M., Udry, S., Naef, D., Pepe, F., Queloz, D., et al. 2004, A&A, 415, 391

Mayor, M., Bonfils, X., Forveille, T., Delfosse, X., Udry, S., et al. 2009, A&A, 507, 487

Menou, K., Tabachnik, S. 2003, ApJ, 583, 473

Noble, M., Musielak, Z.E., Cuntz, M. 2002, ApJ, 572, 1024

Pepe, F., Correia, A.C.M., Mayor, M., Tamuz, O., Couetdic, J., et al. 2007, A&A, 462, 769

Pilat-Lohinger, E., Funk, B. 2010, LNP, 790, 481

Schwarz, R., Pilat-Lohinger, E., Dvorak, R., Érdi, B., Sándor, Z. 2005, Asbio, 5, 579

Schwarz, R., Dvorak, R., Pilat-Lohinger, E., Süli, Á., Érdi, B. 2007, A&A, 462, 1165

Turnbull, M.C., Tarter, J.C. 2003, ApJS, 145, 181

Vogt, S.S., Butler, R.P., Marcy, G.W., Fischer, D.A., Henry, G.W., et al. 2005, ApJ, 632, 638

PADEU | PADEU **20**, 113 (2011)
ISBN 963 463 557

STABILITY OF EXOMOONS

Imre Nagy[1] **and András Pál**[2]

[1]MTA Research Group for Physical Geodesy and Geodynamics Műegyetem rakpart 3, 1111 Budapest, Hungary
[2] Konkoly Observatory of the Hungarian Academy of Sciences, Konkoly Thege M. út 15-17, Budapest H-1121, Hungary

E-mail: [1]`i.nagy@astro.elte.hu`, [2]`apal@szofi.elte.hu`

Abstract
The stability of exomoons was studied using theoretical and numerical methods. The results show that exomoon can exist in a wide range of the parameter space. However, a hot Jupiter-class planet cannot have any exomoons unless the exomoon has higher density than the Earth.
Keywords: *exoplanets, exomoons*

1 Introduction

The first exoplanet (HD 114762b) was discovered in 1989 using a ground-based spectrometer Latham et al. (1989). It was a so-called hot Jupiter: a Jupiter mass planet orbiting very close to its host star. Development of the observation technology allowed to discover several hundred exoplanets. Today 490 exoplanets are listed in The Extrasolar Planets Encyclopaedia (http://exoplanet.eu).

Most of the firstly discovered exoplanetary systems contained only one exoplanet. Using more developed instruments the number of multiple-planet systems increase. Number of planets in multiple-planet systems also increase. For example, Gliese 581, which contains four planets (Mayor et al. , 2009) or HD 10180 with seven possible planets (Lovis et al. , 2010). The rise of complexity will not stop. The next main stage is discovering of the first exomoon.

How can an exomoon be discovered? There is a problem. The mass and the diameter of exomoons are commonly supposed relatively small, maximum

Earth-size. The small mass causes small, almost invisible effects on radial velocity curve. The small diameter causes small effects on light curve, moreover these effects are not periodic, except in resonant systems. These make difficult to detect an exomoon. But planet and its moon orbit each other which causes transit timing effects. Detecting these effects seems to be the most hopeful method to discover exomoons (Kipping , 2009; Szabó et al. , 2006).

There are two variations in the transit. The first is the transit time variation (TTV). Its amplitude is proportional to the mass of the moon times its semi-major axis. The second is the transit duration variation (TDV). Its amplitude is proportional to the mass divided by the square root of the semi-major axis. Therefore, detecting TTV and TDV enable us to determine separately the mass of the moon and the semi-major axis of the orbit of the moon (Kipping , 2009). Current ground-based telescopes could detect an Earth-mass exomoon in the habitable zone around a Neptune-like exoplanet Kipping (2009).

We can detect exomoons using TTV and TDV methods. The next important question is where we should look for exomoons. In this paper, we study this question in a dynamic aspect.

2 Limitations: Roche limit and Hill sphere

In our Solar System the giant planets have the most moons, therefore it seems to be logical searching for exomoons around giant exoplanets. But if the planet and its moon orbit too close to the host star, the surface temperature of the planet and its moon is high. This circumstance restricts the composition of the moon. It is hard to imagine that there are 'hot icy' exomoon (hot Europa or hot Titan) around a hot Jupiter.

On the other hand, if the planet orbits too close to the star, the Roche limit can extend over the Hill sphere. An astronomical body's Hill sphere is the region in which it dominates the attraction of the satellites. The radius of this sphere can be calculated using the approximation

$$r_{Hill} \approx a(1-e)\sqrt[3]{\frac{m_{planet}}{3m_{star}}}, \tag{1}$$

where a, e and m_{planet} are the semi-major axis, eccentricity and mass of the planet, respectively, and m_{star} is the mass of the star.

The Roche limit is the distance within which a celestial body, held together only by its own gravity, will disintegrate due to a second celestial body's tidal

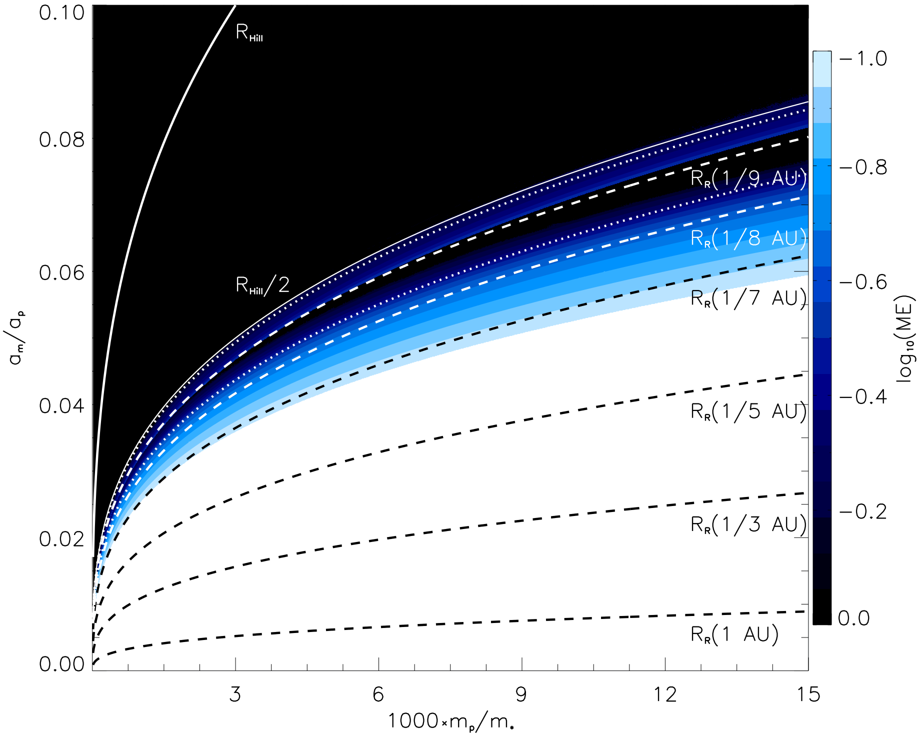

Figure 1: *Stability map of hypothetical exomoons on a planet mass vs. semi-major axis of the moon plane. The brighter gradients correspond to stable orbits while dark colours indicate instability.* R_{Hill} *denotes the Hill radius and* R_R *denotes the Roche limit at several planet's orbit semi-major axis. The upper dotted line denotes the main-motion resonance 1:5 while the lower dotted line indicates the main-motion resonance 1:6. One can see that if the semi-major axis is under 1/9 AU the moon's orbit can be just marginally stable. Here a Sun-like star was supposed, and the density of the moon was supposed 6000* g/cm^3

forces exceeding the first body's gravitational self-attraction. The Roche limit can be calculated:

$$R_{Roche} = R_{planet} \sqrt[3]{2\frac{\rho_{planet}}{\rho_{moon}}}, \tag{2}$$

where R_{planet} is the radius of the planet, ρ_{planet} is the density of the planet and ρ_{moon} is the density of the moon.

One can see, if the Roche limit extends beyond the Hill sphere, exomoons cannot exist further. We can calculate the semi-major axis of the planet's orbit, where the Roche limit and the Hill sphere are equal. It can occur

$$R_{R=H} \approx R_{moon} \frac{1}{1 - e_{planet}} \sqrt[3]{48 \frac{m_{star}}{m_{moon}}}, \tag{3}$$

which is equivalent with

$$R_{R=H} \approx \sqrt[3]{\frac{36}{\pi} \frac{1}{1 - e_{planet}} \frac{m_{star}}{\rho_{moon}}}, \tag{4}$$

where R_{moon} is the radius of the moon and m_{moon} is the mass of the moon.

In the case of the system Gliese 581, $R_{R=H}$ was found to be 7 $\times 10^{-3}$ AU, which is much smaller than the smallest semi-major axis in this system. Consequently, all known planets in the system Gliese 581 can have moons. Here we supposed that the density of the moon is equal to 6000 g/cm^3.

Exomoon can exist between the Hill sphere and the Roche limit. However, the stability of the orbit of the moon is not evident. In the following, we study the stability of the orbits of the moons using numerical methods.

3 Numerical investigations

A model of the restricted three body problem was used to calculate the stability of the moons' orbits. The three bodies orbit in the same plane, and their orbits are circular. The moon was massless. Our distance unit was the semi-major axis of the planet, and our mass unit was the mass of the star. Initially all orbits were circular, and the mean anomalies were zero. The semi-major axis of the moon ran from 0.0001 to 0.1 and the mass of the planet ran from 1.5×10^{-5} to 0.015.

Integrating the equations of motion we used the method of Lie-integration (Hanslmeier & Dvorak , 1984; Pál & Süli , 2007), and the maximum eccentricity (Dvorak et al. , 2003; Süli et al., 2005; Nagy et al., 2006) was calculated in order to characterize the stability.

The main concept of the Lie-integration is to provide the power series coefficients of the solution in the form of recurrence relations (Hanslmeier & Dvorak

, 1984; Pál & Süli , 2007). Although the actual equations forming these recurrence relations depend on the problem itself (this makes the Lie-integration not so widespread, since the derivation of these formulae are not always obvious), the integrator itself is very effective and there are several possibilities to make it adaptive. In addition, contrary to other methods, this method is capable to reach arbitrary precision without the loss of expensive computing time (Pál , 2010).

The values of maximum eccentricity were plotted on Fig. 1. Black colour marks the unstable systems and the yellow colour marks the most stable systems. One can see that exomoons can be stable until half of the Hill sphere. There is a gap in the stable domain. It is located at the 6:1 main motion resonance.

Calculating the Roche limit, we suppose an Earth-like moon with 6000 g/cm^3 density. The Roche limit extends over half of the Hill sphere, when the semi-major axis of the planet's orbit is less than 0.1 AU in the case of a Sun-like star. In this case, no moon can exist around the planet. However, a moon with two times higher density can exist up to 0.08 AU.

In the case of the Gliese 581 all of its planets are located in the stable region, consequently all of these planets can have moons.

4 Conclusions

The complexity of the discovered exoplanetary systems increases. The most complex system contains six planets. The next stage would be the discovering of an exomoon. Using TTV and TDV methods, an exomoon can be observed. An important question is the existence of exomoons. The question was studied using theoretical and numerical methods. Theoretically, a moon can exist if the Hill sphere is larger than the Roche limit. Numerical investigations show that an orbit can be stable until the half of the Hill sphere. Comparing the two results, we pointed out that exomoons can exist in a wide range of the parameter space. However, a hot Jupiter class planet cannot have any exomoons unless the moon has extremely high density, more than twice the Earth's.

References

Dvorak, R., Pilat-Lohinger, E., Funk, B., Freistetter, F. 2003, A& A, 398, L1

Hanslmeier, A., Dvorak, R. 1984, A& A, 132, 203

Kipping, D. M. 2009, MNRAS, 392, 181

Latham, D.W., Stefanik, R.P., Mazeh, T., Mayor, M., Burki, G. 1989, Nature, 339, 38L

Lovis, C., Segransan, D., Mayor, M., Udry, S., Benz, W., et al. 2010, Submitted to A&A

Mayor, M., Bonfils, X., Forveille, T., Delfosse, X., Udry, S., et al. 2009, A& A, 507, 487

Nagy, I., Süli, Á., Érdi, B. 2006, MNRAS, 370, L19

Pál, A., Süli, Á. 2007, MNRAS, 381, 1515

Pál, A. 2010, MNRAS, 409, 975

Süli, Á., Dvorak, R., Freistetter, F. 2005, MNRAS, 363, 241

Szabó, Gy.M., Szatmáry, K., Divóki, Zs., Simon, A. 2006, A& A, 450, 395

PADEU 20, 119 (2011)
ISBN 963 463 557
© Published by the Astron. Dept. of the Eötvös Univ.

ExoStab: A www-Tool to verify the Dynamical Stability of Extra-solar Planets

E. Pilat-Lohinger[1] **and S. Eggl**[2]

Institute for Astronomy, University of Vienna, Türkenschanzstrasse 17, A-1180 Vienna, Austria

E-mail: [1]`elke.pilat-lohinger@univie.ac.at`, [2]`siegfried.eggl@univie.ac.at`

Abstract
We present the www-tool "ExoStab", which aims to help verifying the stability of a terrestrial planet moving in a single star - single giant planet system. ExoStab uses results of the so-called Exocatalogue (Sándor et al. , 2007) to visualize the dynamical state of a certain region in a planetary system. Three options are available: (1) stability of an additional planet (2) stability of the habitable zone (HZ) (3) stability of an additional planet with respect to the HZ. Given some basic parameters of the planetary system, ExoStab displays a general stability map for the system and a zoom of the HZ or of the region where a new small planet is expected. For a brief walk-through of the functions of ExoStab, the extra-solar planetary systems HD121504, HD141937, HD145377 and HD48265 have been selected to serve as examples.

Keywords: *Extra-solar planetary systems, dynamical stability, terrestrial planets, habitable zones*

1 Introduction

The search of Earth-mass planets is currently a venture of great scientific and public interest, as it is an important step towards answering the question "Are we alone in the universe?" Since undertakings of such importance tend to lie on the brink of technological feasibility, terrestrial planets are hard to spot, let alone easy to have their orbital elements determined with sufficient accuracy. Therefore it is of utter importance, to make a check on the dynamical stability of suspected system configurations, as this might help narrowing the set of possible orbital parameters significantly, or rule out additional planets altogether. By now, about 500 extra-solar planets have been observed. Their host systems may be classified as: *single-star single-planet systems – single-star multi-planet systems – planets in double star systems.* As most of the observed extra-solar planetary systems (EPSs) are part of the first group (see e.g. http://exoplanet.eu), the *ExoStab* project's first priority was to set up and visualize stability conditions for additional small[1] planets such configurations may be hosting. The dynamical stability of planets can be established (1) by exploring the phase space of each EPS separately (see e.g. Rivera & Lissauer (2000); Laughlin & Chambers (2002); Menou & Tabachnik (2003); Dvorak et al. (2003); Barnes & Raymond (2004); Asghari et al. (2004); Érdi et al. (2004); Raymond et al. (2006); Rivera & Haghighipour (2007); Schwarz et al. (2007a,b); Pilat-Lohinger (2008) and many others), or (2) by using stability maps computed in advance for a large set of orbital parameters. Approach (1) has the disadvantage, that one has to re-explore the phase space of an individual EPS after each modification of the known planet's orbital parameters. This is not necessary when using method (2), since the stability properties of the investigated EPS can be re-established easily from existing stability maps. Sándor et al. (2007) compiled such a catalogue of stability maps which is implemented in *ExoStab*. Using the planar elliptic restricted three body problem (ERTBP), Sándor et al. (2007) examined the stability of an additional Earth-like planet in single-star single-planet systems. The ERTBP describes the motion of a third body of negligible mass in the gravitational field of a star and a giant planet (GP), without having any influence on the motion of the two massive bodies. Test-computations have shown that this model describes quite well the behavior of Earth-mass planets moving in low-eccentric orbits ($e < 0.2$) around their host-star. For larger masses of the third body the results of the ERTBP can be considered as a first approximation. The main advantage of using the ERTBP is to gain computation time. In order to determine the stable regions for an additional planet in a single-star single-planet system, it is necessary to study the orbital motion of the system for a sufficient number of revolutions and for a large set of orbital parameters. It is obvious that this will be very time con-

---

[1] The terms "small body" or "small planet" used in this paper include Earth-sized and even larger bodies respectively, as long as their mass is negligible compared to the system's giant planet's.

suming, so that alternative methods and simplification – allowing shorter and faster computational runs – are desirable. In order to be able to use a very fine grid for the stability maps, Sándor et al. (2007) applied chaos indicators – the Relative Lyapunov Indicator (RLI, see Sándor et al. (2000, 2004) and the Fast Lyapunov Indicator (FLI), Froeschlé (1997)) – in their study. The reason for integrating as many orbits as possible was the desire for detailed information on the stability of the so-called "habitable zone" (HZ) of a planetary system. The term "habitable zone" dates back to studies by Huang (1959, 1960) and denotes the region around a star where a planet could support carbon based life forms. There have been various ideas concerning its definition, varying from distinct surface temperatures (Dole , 1964) to sustaining liquid water for a substantial time-span. Following Kasting et al. (1993) we take the occurrence of liquid water as a guideline for the boundaries of the HZ, where the luminosity of the host star takes the dominant role in its determination.

However, *ExoStab* is not restricted to visualize the stability of the HZ of a planetary system only. Additionally, the user may define a region of interest, which will then be displayed by *ExoStab*. One can also verify whether a defined area overlaps partly or fully with the HZ in the respective system. The different options provided by ExoStab will be introduced in Section 2, where we describe in brief the implementation of stability maps and the architecture of our Internet tool. In Section 3 we show the application of ExoStab using the single-star single-planet systems HD121504, HD141937, HD145377 and HD48265 as examples. Finally we will sum up those cases for which ExoStab cannot be applied.

2 ExoStab

ExoStab is a www based application that is using data of the *Exocatalogue's* (Sándor et al. , 2007) stability maps in order to offer a quick overview of the dynamic state of additional, small planets in a single-star single-giant-planet system.

2.1 Stability Maps

The *Exocatalogue* (Sándor et al. , 2007) is a collection of 552 stability maps, where the motion of test-planets has been analyzed for 23 different mass-ratios[2] (μ) of the GP and the star, their mutual distance being normalized (set to unity).

---

[2] $\mu = m_2/(m_1 + m_2)$, where m_1 and m_2 are the masses of the star and the giant planet, respectively.

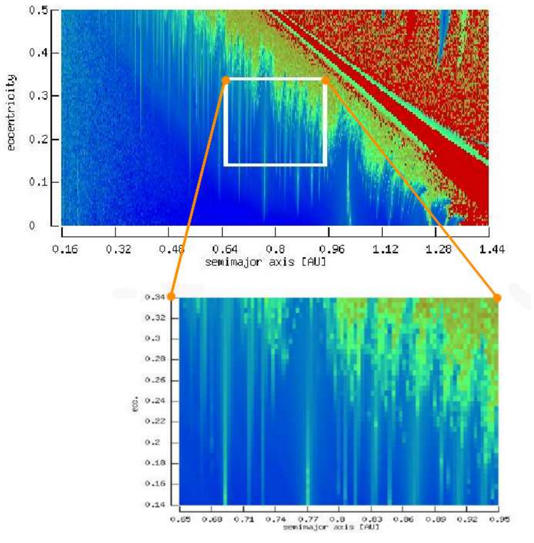

Figure 1: *Example for an additional planet in the inner region. The upper panel shows the stability map of HD48265, created by ExoStab. Blue indicates stable regions, green to red chaotic ones. The white rectangle delimits the region where the (fictitious) new planet is expected. The lower panel shows a zoom of this region.*

μ has been varied from 1×10^{-4} to 5×10^{-2}, and the eccentricity of the GP has been increased from 0 to 0.5 (= y-axis of the stability maps). Additionally the starting position of the GP has been modified (for details see Sándor et al. (2007)). For all mass-ratios μ the *inner region* (i.e. between the star and the GP) – where the distance to the star was varied from 0.1 to 0.9 – and the *outer region* (i.e. outside the GP) – from 1.1 to 4 – was studied concerning the stability of motion of the test-planet. To distinguish between stable and chaotic motion the chaos indicator, RLI (see e.g. Sándor et al. (2000, 2004) was used for the whole numerical study of the Exocatalogue. The FLI (see e.g. Froeschlé (1997), as well as the *Maximum Eccentricity Method (MEM)* (see e.g. Dvorak et al. (2003)) were used to verify the results of the RLI computations[3].

---

[3] The three methods have been applied successfully to several exo-planetary systems in order to determine the dynamical state of motion (see e.g. Érdi et al. (2004); Sándor et al. (2004); Dvorak et al. (2003); Funk et al. (2009); Pilat-Lohinger et al. (2008a,b) and many

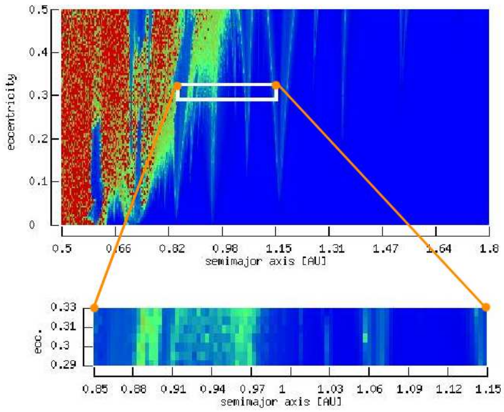

Figure 2: *Example for an additional planet in the outer region. The upper panel shows the stability map of HD145377, created by ExoStab. For details see Fig. 1.*

The results of these three methods were in good agreement, so that the fastest method (the RLI) was applied for the whole study.

Using the results of the Exocatalogue to investigate an EPS's stability requires a manual search for the appropriate stability map via calculation and matching of the corresponding μ values as well as a conversion of the system's dimensions into appropriate units. This will now be done by our tool *ExoStab*.

2.2 Web-Interface of ExoStab

The www-tool *ExoStab* is available at http://univie.ac.at/adg/exostab and provides the following options concerning a stability investigation of single-star single-giant-planet systems:

1. Stability of an additional planet

2. Stability of the habitable zone (HZ)

3. Stability of an additional planet with respect to the HZ

---

others).

Some basic information on the system in consideration is needed:

- mass of the host-star (M_{star})
- mass of the known GP (M_{GP})
- the distance of the GP from its host-star (a_{GP})
- the GP's eccentricity (e_{GP})
- the uncertainty in eccentricity[4] ($\pm\Delta e_{GP}$)

Details about the specific input for the different options of ExoStab are discussed in sections (3.1 - 3.3). Given the appropriate input, ExoStab determines the system's mass-ratio, filters the corresponding stability data from the Exocatalogue (Sándor et al. , 2007), converts the normalized units into system-units, and plots a stability map. In this stability map, stable regions are represented in blue color and the chaotic ones vary from green to red. By the term "stable" we mean, that trajectories of a system are located in an ordered region of the phase space, while chaotic regions are characterized by exponential divergence of initially neighbored phase space trajectories.

2.3 ExoStab: Programming and Architecture

ExoStab is implemented in PHP 5.0 and uses a MySQL database in conjunction with raw data files containing RLI values of the ERTBP for a given set of parameters as backend. The underlying data model consists of a table called *map* which stores the following attributes: mass of star, mass ratio between the GP and the star(μ), the boundaries of the stability analysis (inner or outer) concerning the distance of the test particle from the main bodies, and the path to the corresponding *Exocatalogue* data file. Within the application, the PHP class *StabilityMap* contains all methods used to generate a visual image showing color-coded RLI values plotted against user defined parameters, a so-called "Stability Map". The class also handles an interface to the database to search, store, delete or update Stability Maps. A short description of the most important methods contained in that class follows:

- *createStabilityMap*: Reads the data file corresponding to the user's requirements from the file system, stores the data into a vector and dynamically creates an image resource using GDlib (graphics library written in C). The

---

[4] If no uncertainty in e_{GP} is provided, a standard value of ±0.005 will be applied.

color of each pixel is calculated in the lookup_color method. In order to make the coloring of stability regions as intuitive as possible, the following color functions (RGB) have been chosen to represent the RLI-values given in the original Exocat data:

$$r = 0.8 - nRLI$$
$$g = \sin(3.4 * nRLI)$$
$$b = nRLI$$
$$0 \leq r, g, b \leq 1$$

with $nRLI$ denoting the normalized RLI Value:

$$nRLI = -\frac{\log_{10} RLI}{10}$$

The subsequent color-value vector in standard RGB code is then given by:

$$(R, G, B) = (r, g, b) \cdot 255$$

Therefore *highly chaotic regions* will be represented in *red*, and *stable regions* will tend to be *blue*.

- *addAxisToStabilityMap*: Draws axis and axis labels in actual system units for the newly generated image.

- *createHabitableZoneImage*: Builds the zoom-able Habitable Zone image based on the search criteria entered by the user.

- *drawZone*: Draws a rectangle in the specified color onto the current StabilityMap plot, in order to denote the stability region requested by the user.

The user interface is generated employing the Smarty template engine for a clear separation of application code and presentation layer. After the user entered the required parameters for a search in the *ExoStab* system, a validity check will be performed to avoid erroneous input. If all entered parameters are correct, they are passed and the calculations necessary to determine the matching Stability Map will be performed. In case that the user's requests are not represented in the available data, the application will return a corresponding error message. With the data from the chosen Stability Map, the methods described earlier are being executed.

	M_{star} $[M_\odot]$	M_{GP} $[M_J]$	a_{GP} $[AU]$	e_{GP}
HD 48265	0.93	1.2	1.6	0.24 (± 0.1)
HD 145377	1.12	5.76	0.45	0.307 (± 0.017)

Table 1: *Exemplary systems for the stability of an additional planet in a single-star single-giant-planet system. In the system HD48265 the discovery of small planet moving in the region between the host-star and the GP is assumed. HD145377 was used to show the stability of an additional planet moving outside the orbit of the known GP. M denotes respective masses, a semi-major axis and e eccentricity. The data was taken from http://exoplanet.eu.*

3 Application of ExoStab

3.1 Stability of an additional planet

In order to check for the stability of a newly discovered planet within a system, that is hosting a GP, some extra information on the additional planet is required: (i) its semi-major axis with respect to the host-star and (ii) the probable error in the semi-major axis.

According to the input ExoStab searches the appropriate result from the Exocatalogue and generates a stability map in coordinates of the EPS in consideration. Fig. 1 shows the system HD48265 as an example, in which a newly discovered small planet (which is fictitious in this case) moves in the region between the host-star and the known GP. The necessary input parameters for the use of ExoStab on HD48265 are given in Table 1.

The stability map for this system drawn from the appropriate result of the *Exocatalogue* – using a more intuitive color code[5]: here blue defines the zone of stable motion and green to red indicate chaoticity – is shown in the upper panel of Fig. 1. A decrease of the stable region when increasing the giant planet's eccentricity is clearly visible. Additionally, one recognizes vertical green lines that indicate perturbations within the stable region due to mean motion resonances (MMRs) with respect to the GP. The white rectangle marks the region, where the newly discovered (in this case fictitious) planet is expected according to observations. Its position and size are given by the semi-major axis of the terrestrial planet (a_{TP}) and its error (Δa_{TP}) on the x-axis. The

---

[5] In the *Exocatalogue* stable regions are yellow and orange and red to black colors mark chaotic motion.

GP's eccentricity (e_{GP}) and its corresponding error (Δe_{GP}) define the size of the rectangle in y-direction. The lower panel of Fig. 1 is a magnification of the area within this rectangle, which shows the perturbation due to the MMRs more clearly. In this context we have to point out that the data used to generate these stability maps contains aligned starting positions of the three celestial bodies only, with the GP being started from its pericenter in case of eccentric motion. The Exocatalogue encompasses stability maps for various starting configurations of every mass-ratio of the star and the GP. Therefore, in case of a possible dominance of MMRs in the stable region in question, we recommend users of ExoStab to check on changes of the dynamical behavior for various initial starting positions at MMRs in the Exocatalogue (the appropriate mass-ratio of the planetary system for the Exocatalogue will be provided by ExoStab).

In analogy to Fig. 1, Fig. 2 shows the generated stability maps for planetary system HD145377, where a fictitious planet is expected in the outer region, i.e. its orbit is beyond the GP's. The zone of chaotic motion increases again linearly with the eccentricity of the GP. Close to the border of regular and chaotic motion we see perturbations due to MMRs as well. The other features are similar to the first example.

3.2 Stability of the Habitable Zone

This topic requires many assumptions, e.g. on the mass of the planet, its overall composition, stage of planetary evolution, albedo, even on cloud formation. Experimenting with CO_2, N_2, H_2O atmospheric compositions Kasting et al. (1993) were able to derive HZ boundaries for spectral types M0,G2 and F0, and different planetary masses ranging between Mars-sized and about ten times the mass of the Earth, assuming different water-loss scenarios.

Among those, the most universally applicable - because least dependent on initial conditions - are:

- the *runaway greenhouse-effect* setting in after all surface water was vaporized, thus being a delimiter of a possible distance towards the star
- and the *"snowball-climate-collapse"* that, assuming a *maximum greenhouse effect*, denotes a sudden rise in the planet's albedo due to glaciation and CO_2 condensation and serves therefore as an outer boundary.

We incorporated these limits, that are valid for a roughly Earth sized planet around a ZAMS host star (see Table 2) into *ExoStab* as presets, presenting an alternative to a fully user-defined HZ. At this point, the authors would like to

spectral type	M0	G2	F0
HZ: inner limit [AU]	0.24	0.84	1.50
HZ: outer limit [AU]	0.47	1.67	3.06

Table 2: *Inner and outer limits of the HZ for ZAMS spectral types* $M0, G2, F0$ *(Kasting et al. , 1993)*

stress, that the HZ for the Solar System has been more rigorously shown to have a stretch between $0.95 - 1.37[AU]$, and a CHZ of $0.95 - 1.15[AU]$ (see Kasting et al. (1993)). Yet, for the sake of model consistency, we chose to implement the somewhat larger estimates based on runaway and maximum greenhouse effects. The fact, that there is a substantial number of assumptions involved in the process of calculating HZs may seem a little unsettling. Yet, as of now, there still is very little spectroscopic data of Exoplanets available, thus leaving lots of room for educated speculations. For recent developments in the field of determining HZs see e.g. Selsis et al. (2007); Lammer et al. (2003, 2007); Kaltenegger et al. (2007).

Having gracefully defined the borders of the HZ, one should not forget to check, whether the planet actually stays there long enough to qualify as biocompatible. After all, subtle changes in the planet's orbit or its obliquity may have massive effects on the solar radiation influx, and therefore the habitability, as can be seen from the example of Earth's glacial periods (see e.g. Milankovitch (1941); Laskar et al. (1993); Berger et al. (2005)). Changes in a planet's orbital elements require perturbing forces, which may arise from a companion star, other planets or even the galactic potential[6]. Thus it is essential to investigate the dynamical properties of any multi-planetary system where one body is suspected to be within the HZ. As *ExoStab* is - as of yet - designed to work specifically for single-star, single-giant-planet systems, we distinguish 3 types of HZ from a dynamical point of view:
I: the **inner HZ** stretching between the host-star and the GP (comparable to the Solar System)
II: the **outer HZ** which is outside the orbit of the GP, that will be the case for close-in planets and
III: the **giant planet HZ** when the GP was discovered in the HZ. However, the type III HZ cannot be studied via *ExoStab*.

---

[6] As the model for *ExoStab* was the ERTBP, no perturbation through the galactic potential has been included

	M_{star} $[M_\odot]$	M_{GP} $[M_J]$	a_{GP} $[AU]$	e_{GP}	spectral type
HD 121504	1	0.89	0.32	0.13	G2V
HD 141937	1	9.7	1.52	0.41 (± 0.01)	G2/G3V

Table 3: *Exemplary systems for different types of HZ. M denotes respective masses, a semi-major axis, e numeric eccentricity. The data was acquired from http://exoplanet.eu.*

In order to determine the type of HZ and the dynamical state of orbits in this region the following parameters have to be known:

- masses of star and GP
- semi-major axis of the GP
- GP's eccentricity and its corresponding uncertainty
- borders of the HZ or the stellar spectral type

If a predefined stellar spectral type option is chosen, and thus the HZ automatically generated, its borders will be set according to Kasting et al. (1993), as was explained previously. Systems HD 121504 and HD 141937 will serve as examples (see Table 3). Fig. 3 shows a stability map of HD121504 generated by *ExoStab* using the option of a predefined stellar spectral type of G2. One can see clearly, that the HZ of this system is of type II and dynamically stable. The picture was truncated at 1.28 AU, as nothing will interfere with the stability from there on to the outer border of the HZ at 1.67 AU. A zoom into the region of the HZ also provided by ExoStab, but not displayed here, since the whole HZ is stable in our example.

An obvious restriction poses the fact, that using the combination of the ERTBP for stability analysis and the HZ borders following Kasting et al. (1993) contains a trade-off. When the planetary masses become much smaller than Earth's mass, the stability model will become more reliable, whereas the assumptions on the planets atmosphere will no longer be consistent. Thus, the optimum configuration concerning the GP and the terrestrial planet would be somewhere around a Jupiter to Earth mass ratio.

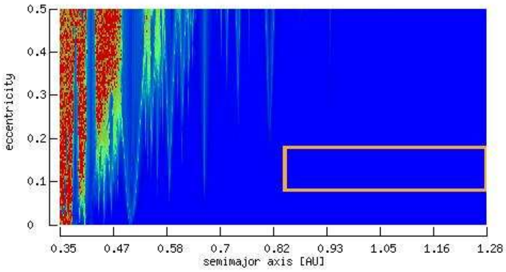

Figure 3: *Stability map for the HD121504 system created by ExoStab. Blue denotes stable regions and green and red the chaotic zone. The orange rectangle frames the HZ, which lies in the stable zone, so that HD121504 could host another minor planet according to the orbital dynamics. As there was no uncertainty in e_{GP} given, an error of* ± 0.05 *was assumed.*

3.3 Stability of an additional planet with respect to the Habitable Zone

One of the most interesting aspects of the *ExoStab* application is the option of checking whether a newly discovered terrestrial planet may be situated within the system's HZ, and if that configuration would be a stable one. Being a combination of the options described in sections 3.1 and 3.2 the input required encompasses - apart from standard data on the system (M_{star}, M_{GP}, a_{GP}, e_{GP}, $\pm\Delta e_{GP}$) - the extent of the HZ (see section 3.2 for details) plus the semi-major axis (a_{TP}) and its uncertainty ($\pm\Delta a_{TP}$) of the suspected, or confirmed minor planet. Please note, that the stability calculation's initial conditions were such as the minor planet was having no eccentricity. Initial eccentricity of the minor body is currently in progress, and cannot be accounted for until now, as are different relative starting positions and inclinations. The resulting plots will depict the planet's stability domain, the dynamical state of the HZ, as well as a zoom of their common overlap, should there be one. As an example, we assumed a fictitious minor planet in the system HD141937 (see Table 3) situated at $a_{TP} = 0.7$ with an uncertainty of $\pm\Delta a_{TP} = 0.2$. Fig. 4 shows, that, even though the minor planet may theoretically be situated within the HZ, dynamically it is more likely that its orbit resides at the border of the influence zone of the GP. Though, given the overall dynamical situation in the

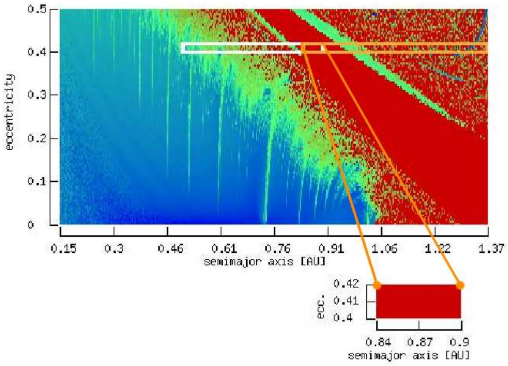

Figure 4: *Stability Map of a type I HZ around HD141937 (orange rectangle) plus a fictitious planet at* $a_{MP} = 0.7 \pm 0.2 AU$ *(white rectangle). In this case, there is a possibility that the planet resides within the HZ, but the overlapping area is highly chaotic (red).*

plot, one would recommend to revise this fictitious observation.

3.4 Caveats

Even if ExoStab is applicable to most of the EPS, there are some restrictions that are summarized as follows:

- Since the model used for ExoStab is the RTBP, the mass of the additional planet should remain negligible compared to the system's GP.
- ExoStab stability data contains cases only, in which all three bodies have been started aligned. This affects the terrestrial planet's behavior around MMRs, therefore we recommend, that users of ExoStab refer to the Exo-catalogue, if the system in question exhibits strong influences of MMRs.
- At the moment, ExoStab provides dynamical states for nearly circular initial conditions of the terrestrial planet only. Also the mutual inclination of the planet to the plane of the star and the GP should not be excessive. A study about eccentric and inclined motion of the additional planet is still in progress.

- ExoStab should not be used to investigate so-called "Hot Jupiter" systems, as physical properties of these systems, that have not been included in the Exocatalogue's models, become non-negligible (e.g. influence of radiation, gas-drag, etc.).

- The borders of the preset for the HZ of G2 stars have been chosen according to runaway and maximum greenhouse effects, and does not correspond to the commonly accepted values for the Solar System.

- From the viewpoint of dynamics, only two cases, namely the GP moving outside or inside the HZ, can be studied via *ExoStab*. Unfortunately, the data of the *Exocatalogue* does not contain stability maps of the GP orbiting within the HZ, therefore a possible stable Trojan motion can, up to now, not be accounted for. A detailed investigation on this topic was performed by Schwarz (see e.g. Schwarz et al. (2007a,b)) and some of the results can be obtained via the "catalogue of fictitious trojan planets in extrasolar systems" (http://www.univie.ac.at/adg/Research/exotro/exotro.html)

4 Conclusion

We introduced the world wide web application *ExoStab*, that provides a quick view on the dynamical behavior of additional, terrestrial planets in single-star single-giant-planet systems. Given a small set of parameters (like the masses of the host-star and the GP, semi-major axis and eccentricity of the GP) of the extra-solar planetary system a stability map can be generated, that denotes stable and chaotic regions inside and outside the GP's orbit. Since we know that there is a special interest in the stability of Earth-mass planets, especially if they are discovered in the HZ – where such a planet could support carbon based life forms – our tool *ExoStab* provides 3 types of stability checks: (i) a newly discovered, additional (Earth-mass) planet lies within a stable region; (ii) the presumed HZ of its host-star permits stable planetary motion and (iii) the new planet orbits within the presumed HZ. The resulting stability maps offer a detailed picture of the dynamical properties of the terrestrial planet in the user specified regions of interest. Further investigations, where the initial eccentricity of the terrestrial body, or relative inclinations between the two planets as well as different relative starting positions of the two planets are in progress and will be implemented as soon as possible.

Acknowledgement

This work was carried out within the framework of the FWF project no. P19569-N16. Siegfried Eggl would like to acknowledge the financial support from FWF project no. P20216.

References

Asghari, N., Broeg, C., Carone, L., Casas-Miranda, R., et al. 2004, A&A, 426, 353

Barnes, R., Quinn, T. 2001, ApJ, 550, 884

Barnes, R., Raymond S.N. 2004, ApJ, 617, 569

Berger, A., M??lice, J. L., Loutre, M. F. 2005, Paleoceanography, 20, 4

Dole, S. H.: 1964, Habitable Planets for Man. Blaisdell, New York.

Dvorak, R., Pilat-Lohinger, E., Funk, B., Freistetter, F. 2003, A&A, 410, L13

Érdi, B., Dvorak, R., Sándor, Zs., Pilat-Lohinger, E., Funk, B. 2004, MNRAS, 351, 1043

Funk, B., Schwarz, R., Pilat-Lohinger, E., Süli, Á., Dvorak, R. 2009, P&SS, 57, 434

Froeschlé, C., Lega, E., Gonczi, R. 1997, CMDA, 67, 41

Hart, M. H. 1978, Icarus, 33, 23

Huang, S.-S. 1959, Am. Sci., 47, 397

Huang, S.-S. 1960, Sci. Am., 202, 55-63

Kaltenegger, L., Traub, W. A., Jucks, K. W. 2007, ApJ, 658, 598-616

Kasting, J. F., Whitmire, D. P., Reynolds, R. T. 1993, Icarus, 101, 108

Lammer, H., Selsis, F., Ribas, I., Guinan, E. F., Bauer, S. J., Weiss, W. W. 2003, ApJ Letters, 598, L121

Lammer, H., Lichtenegger, H. I. M., Kulikov, Y. N., et al. 2007, Astrobiology, 7, 185

Laskar, J., Joutel, F., Robutel, P. 1993, Nature, 361, 6413, 615

Laughlin, G., Chambers, J., Fischer, D., 2002, ApJ, 579, 455

Menou, K., Tabachnik, S. 2003, ApJ, 583, 473

Milankovitch, M.: (1998) [1941], Canon of Insolation and the Ice Age Problem. Belgrade: Zavod za Udz?benike i Nastavna Sredstva. ISBN 8617066199

Pilat-Lohinger, E., Süli, Á., Robutel, P., Freistetter, F. 2008a, ApJ, 681, 1639

Pilat-Lohinger, E., Robutel, P., Süli, Á., Freistetter, F. 2008b, CeMDA, 102, 83

Pilat-Lohinger, Proceedings of the international conference "Extrasolar Planets in Multi-body Systems: Theory and Observations", Torun 2008, ed. Gozdziewski, submitted.

Raymond, S.N., Barnes, R., Kaib, N.A. 2006, ApJ, 644, 1223

Rivera, E., Haghighipour, N. 2007, MNRAS, 374, 599

Rivera, E., Lissauer, J. 2000, ApJ, 530, 454

Rivera, E., Lissauer, J. 2001, ApJ, 554, 1141L

Sándor, Zs., Érdi, B., Efthymiopoulos, C. 2000, CeMDA, 78, 113

Sándor, Z., Érdi, B., Széll, A., Funk B., 2004, CeMDA, 90, 127

Sándor, Zs., Süli, Á., Érdi, B., Pilat-Lohinger, E., Dvorak, R.: 2007, MNRAS, 375, 1495

Schwarz, R., Dvorak, R., Pilat Lohinger, E., Süli, Á.,Érdi,B. 2007a, A&A, 462, 1165

Schwarz, R., Dvorak, R., Süli, Á.,Érdi,B. 2007b, Astronomische Nachrichten, 328, 785

Selsis, F., Kasting, J.F., Levrard, B., Paillet, J., Ribas, I., Delfosse, X. 2007, A&A, 476, 1373

PADEU
PADEU **20**, 135 (2011)
ISBN 963 463 557
ⓒ Published by the Astron. Dept. of the Eötvös Univ.

DYNAMICS OF POSSIBLE TROJAN PLANETS IN BINARY SYSTEMS - THE 3 DIMENSIONAL CASE

R. Schwarz and S. Eggl

Institute for Astronomy, University of Vienna, Türkenschanzstrasse 17, A-1180 Vienna, Austria

E-mail: `schwarz@astro.univie.ac.at`

Abstract
This paper is devoted to the stability of possible, inclined Trojan planets in double star systems. We investigated the size of the stable region around the Lagrangian point L_4 by using numerical integrations, depending on the mass ratio and the eccentricity of the secondary star. The dynamical model we used was the spatial elliptic restricted three body problem. We created a catalogue of initial conditions where a Trojan planet can be stable. These results could be useful for future observations and help to detect such objects.

Keywords: *Trojan planets, celestial mechanics, double stars.*

1 Introduction

Today we know of more than 490 extra solar planets, but only 40 are in binary systems (see http://exoplanet.eu by Jean Schneider at). In future we will find many more planets in multiple stellar environments, because of the fact that seventy percent of all stars in the solar neighbourhood are members of binary or multiple-systems (67 % for G-M stars, Mayor et al. (2001), $\sim 75\%$ for O-B stars, Mason et al. (2001); Verschueren et al. (1996)).

When we speak of dynamical stability of planets in binaries, we categorize motion as follows:

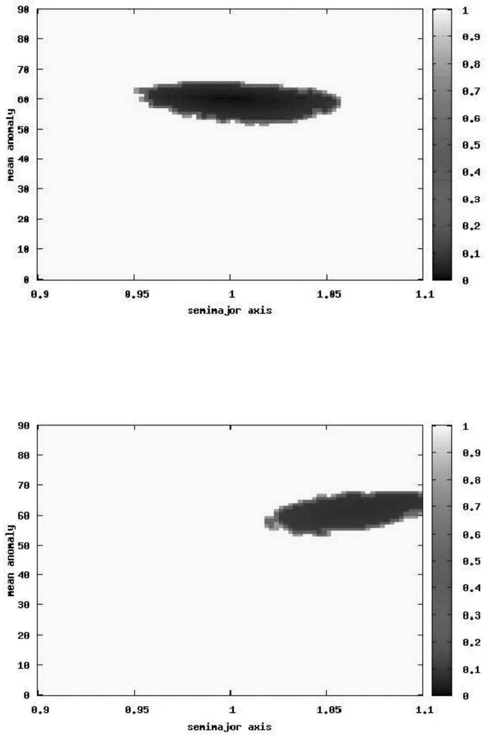

Figure 1: *Initial condition diagram (semi-major axis versus mean anomaly) for the CR3BP for the mass ratio* $\mu = 0.033$*, with different initial velocities:* v_T *(upper graph) and* v_{Kep} *(lower graph). Dark grey marks stable orbits (low* e_{max}*) and white denotes escapers.*

1. **S-Type:** The planet orbits one of the two stars.
2. **P-Type:** The planet maintains an orbit around both stars.
3. **T-Type:** A planet may move close to the equilibrium points L_4 and L_5.

As an example, our Solar System hosts a substantial asteroid population around L_4/L_5 of the Sun-Jupiter system. That means that the Jupiter's Trojans are

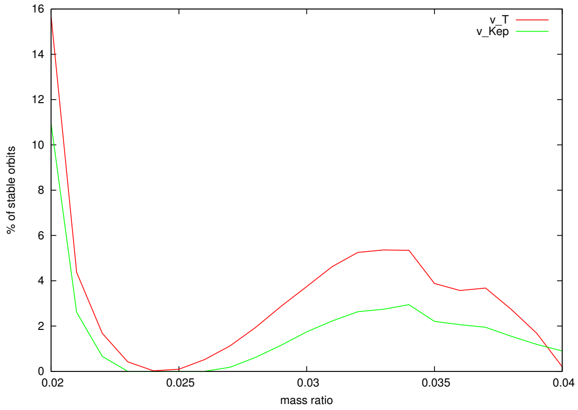

Figure 2: *Size of the stable region around L_4 in the CR3BP. The upper line shows the calculations for v_T whereas the lower line shows the one with v_{Kep}. The integrations were done for 10^6 years.*

Table 1: *Orbital elements of two binary systems, with a mass ratio μ smaller than 1/25.*

Name	Sp. type	mass $[M_{sun}]$	μ	a [AU]	e
51θ Vir A	A1lvs	2.98	0.26	–	–
51θ Vir B	?	0.08	0.26	9.91	?
53ξ Uma A	G0V	1.1	0.35	–	–
53ξ Uma B	?	0.04	0.35	15.99	0.39

moving either close to 60° ahead of or 60° trailing Jupiter sharing an almost identical semi-major axis.

In this paper we are investigating T-Type motion in binary star systems. Motion near the Lagrangian points (L_4 and L_5) only remains stable for a mass ratio $\mu < 1/25$ of the primary bodies. In our last article (Schwarz et al. , 2009a,b) we found, that there are 6 double stars with mass ratios below this stability limit, according to the catalogue of physical multiple stars (Tokovinin , 1996). Out of the 6 binaries 2 systems are well known binary systems with orbital elements, given in Table 1. Four candidates are registered without known orbital elements: HD223099 ($\mu = 0.03$), SB 152 ($\mu = 0.035$), SB 667 ($\mu = 0.03$), and SB 831 ($\mu = 0.03$).

Theoretical studies suggest that Trojans are a frequent by-product of planet formation and evolution processes. Hydrodynamic simulations of a proto-planetary disk have been undertaken by Laughlin & Chambers (2002); Chiang & Lithwick (2005); Beaugé et al. (2007); Ford & Gaudi (2006); Ford & Holman (2007) examined the sensitivity of transit timing observations for detecting Trojan companions of extra solar planets. They demonstrate that this method offers the potential to detect terrestrial-mass Trojans using existing ground-based observatories.

2 Numerical Setup

As shown in Schwarz et al. (2005) the restricted three-body problem (R3BP) provides valid approximations for up to Neptune mass Trojan planets, and is therefore the dynamical model of choice for our investigations. In order to perform a stability analysis we used the orbital escape of the Trojan planet on the one hand (planetary eccentricity $e_{max} = 1$) and the Lyapunov Characteristic Indicator (LCI) on the other hand. LCI denote the finite time approximations of the maximal Lyapunov Exponent (LCE).

For our test calculations we used N-body integrators contained in the *lie*-package (e.g. Hanslmeier & Dvorak (1985); Eggl & Dvorak (2010)) and our own Bulirsch-Stoer-based code that solves the equations of motion in the binary's co-rotating system.

3 Initial Conditions

A common simplification of the Trojan planet's initial conditions consists of the initialization on the secondary's orbit, starting the particle at the Lagrangian point without altering its initial, specific Keplerian velocity. This approach is valid for small mass ratios $\mu = m_{sec}/(m_{prim} + m_{sec})$, but it will yield considerable deviations from the analytical solutions of the circular R3BP (CR3BP) for μ as large as in the binary systems under investigation (see Fig. 1). The reason for this behavior lies in the trivial fact that velocities on Keplerian orbits are proportional to the square-root of the sum of the masses of the orbited primary and the orbiting particle. The Lagrangian equilibrium solutions - being at rest in the binary's co-moving frame - rotate with the secondaries' Keplerian velocity, which will be different from the Trojan's. A Trojan's purely Keplerian

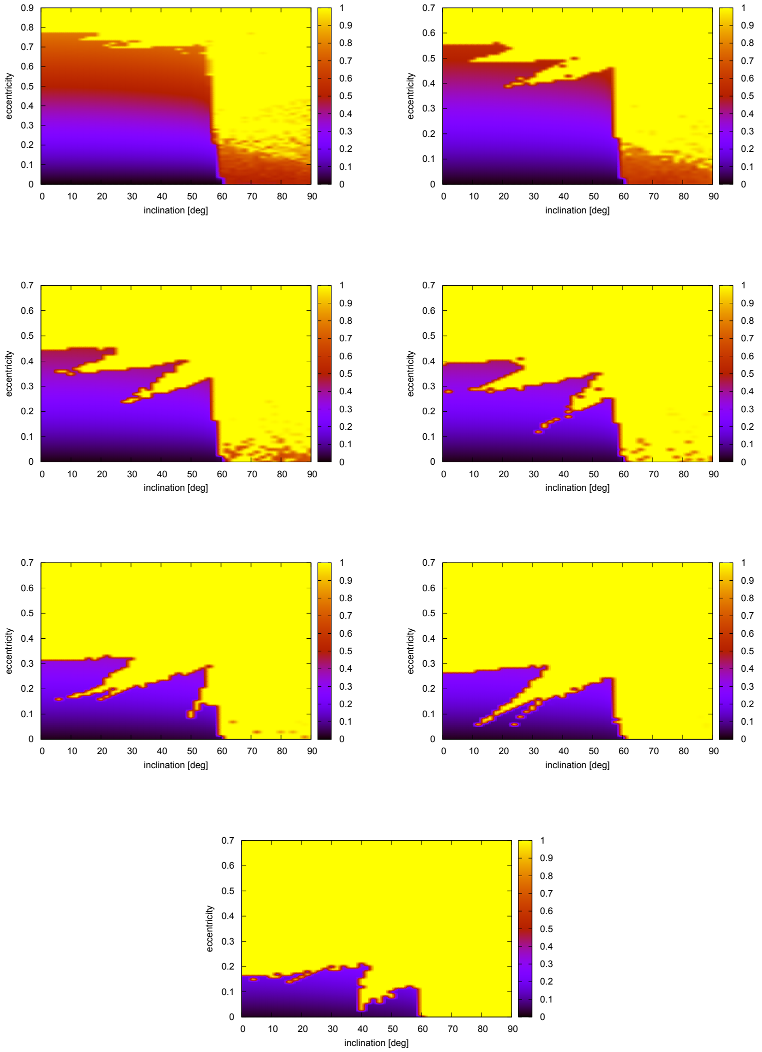

Figure 3: *Maximum eccentricity plots for* **upper two graphs***:* $\mu = 0.001$ *(left) and* $\mu = 0.005$ *(right);* **mid-upper two graphs***:* $\mu = 0.008$ *(left) and 0.01 (right);* **mid-lower two graphs***:* $\mu = 0.013$ *(left) and 0.015 (right);* **lowest graph***:* $\mu = 0.020$. *In all plots the initial inclination of the test-planets is plotted versus their eccentricity. Black and violet mark stable orbits (low eccentricity) and yellow denotes escapers. The integrations were done for* 10^4 *system revolutions.*

initial velocities (v_{Kep}) and the correctly scaled ones (v_T) are related via:

$$v_T = \sqrt{\frac{m_{prim} + m_{sec}}{m_{prim} + m_T}} v_{Kep} \tag{1}$$

where m_{prim},m_{sec} and m_T denote the masses of primary, secondary and Trojan respectively.

3.1 Different results for different initial velocities

In order to demonstrate the implications of an oversimplification of initial conditions, we created stability maps of the CR3BP and analyzed the size of the stability region around the Lagrangian point L_4. We varied the semi-major axis a between 0.9 and 1.1 and the mean anomaly M between 0° and 180° with the appropriate grid of initial conditions, with a step size of $\Delta a = 0.0025$ and $\Delta M = 2°$. We started the Trojan planet in the Lagrangian point L_4 ($M_{Trojan} = 60°$, $e_{Trojan} = e_{secondary} = 0$) and integrated for 10^3 periods. The mass ratio μ was varied between 0.02 and 0.045 with a step size of $\Delta\mu = 0.0005$. During our test computations with the initial v_{Kep}, we found that the stable region shifted from the $M = 60°, a = 1AU$ domain. An analytical determination of the location of the altered zero-force equilibrium point was performed using the equations of motion of the CR3BP including the Trojan's initial, relative velocity. Numerical results are in agreement with the analytically derived solutions and are presented in Fig. 1 for a mass ratio of $\mu = 0.033$. In addition we calculated the percentage of stable orbits in the stability maps - as shown in Fig. 2 - where we compare the two cases: purely Keplerian initial velocities and the correctly scaled ones. We can conclude, that carelessness concerning initial velocities does not only cause a shift of the stable region, but alters its critical mass ratio, too (see Fig. 2).

4 Results of the 3 dimensional case

Observations in the Solar System have shown, that Trojan asteroids can have very large inclinations. Therefore it is essential to study inclined orbits in the case of Trojan planets. We started the test-planets in the Lagrangian point[1] at a normalized distance of 1 AU from the central star, and constructed a grid of

---

[1] Trojan and gas giant share the same eccentricity

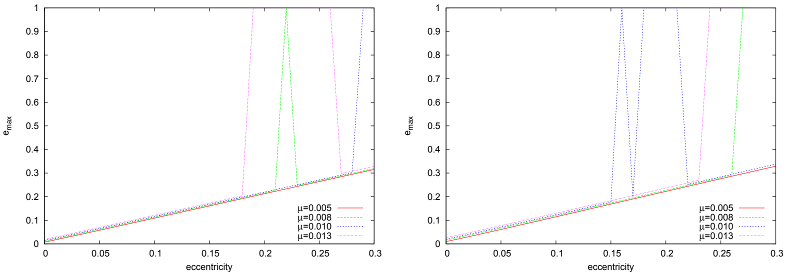

Figure 4: *Cuts related to the e_{max} plots (Fig. 3) for the following mass ratios:* $\mu = 0.005$, $\mu = 0.008$, $\mu = 0.010$ *and* $\mu = 0.013$. *The left graph show the cut for an initial inclination of* 25° *and the right one for* 40°. *The integrations were done for* 10^6 *system revolutions.*

initial conditions. The initial eccentricity of the Trojan e was set equal to the binary's e_{bin}. We varied the eccentricity $0 < e < 0.9$ (step $\Delta e = 0.01$) and the inclination $0^\circ < i < 90^\circ$ (step $\Delta i = 2^\circ$) of the Trojan planet. The mass ratio μ was altered from 0.001 to 0.02 with a stepping of $\Delta\mu = 0.001$. This study is an extension and correction of the former work by Funk et al. (2009) who were using oversimplified initial conditions as described earlier. We extended our investigation using a larger range of initial conditions: eccentricity (extension from $e = 0.3$ to $e = 0.9$) and μ (extension from $\mu = 0.015$ to $\mu = 0.020$). The different results due to initial velocities v_T and v_{Kep} are clearly visible for mass ratios down to $\mu = 0.005$ (Fig. 3 upper left graph). Our investigations showed that for a mass ratio of $\mu = 0.001$ Trojans are stable up to binary-eccentricities of $e = 0.77$.

The mass ratio $\mu = 0.005$ shows a finger-like unstable structure, which appears in the range of $10^\circ < i < 37^\circ$ and $e > 0.2$ of the stability map (Fig. 3 upper right graph). For $\mu = 0.008$ we see an increase of this unstable island to smaller eccentricities ($e \geq 0.2$). In the result of $\mu = 0.010$ the unstable, finger-like structure is shifted towards the large unstable region for $i > 60^\circ$.

For mass ratios of $\mu \geq 0.013$ we are close to the limit separating brown dwarfs from gas giants. This border is defined via the minimum mass required to cause substantial fusion (approximately 13 Jupiter masses, e.g. Basri & Brown (2006)). When we look at the results for $\mu = 0.013$, the unstable region is growing in size and shifted towards smaller eccentricities, and the finger-like structure disappears in the large unstable zone at $i < 60^\circ$. For the mass ratio $\mu = 0.015$ the stable region shrinks below an initial eccentricity of $e = 0.3$.

We also checked the long term validity of our results by choosing cuts in parameter space (for $i = 25°$ Fig. 4 left graph and $i = 40°$ Fig. 4 right graph), where we increased integration time up to 10^6 system revolutions. These test calculations showed, that there is no large difference between an integration time of 10^4 and 10^6 system years. The origin of the finger-like structure is unclear, but we suppose that secondary resonances play a major role (see also Érdi et al. (2007a,b); Robutel & Gabern (2006)). In contrast to the simulations with initial eccentricities ($e = e_{bin}$), the circular cases did not show escapes up to initial inclinations $i = 60°$ for all investigated mass ratios, shown in Fig. 3 (calculation time 10^6 years). Further investigations have to be done to identify the definitive origin of the finger-like structure.

Acknowledgement

R. Schwarz wants to acknowledge the support by the ÖFG (project MOEL 386) and the Austrian FWF project no. P18930. S. Eggl wants to acknowledge the support by the Austrian FWF project no. P20216.

References

Basri, G., Brown, M. E., 2006, AREPS 34, 193

Beaugé, C., Sándor, Zs., Érdi, B., Süli, Á., 2007, A&A, 463, 359

Chiang, E. I., & Lithwick, Y. 2005, ApJ, 628, 520.

Eggl, S., Dvorak, R., 2010, LNP, 790, 431

Érdi, B., Nagy, I., Sándor, Zs., Süli, Á., Fröhlich, G., 2007, MNRAS, 381, 33

Érdi, B., Fröhlich, G., Nagy, I., Sándor, Zs., 2007b, MNRAS, 381, 33

Fabricius, C., Hog, E., Makarov, V. V., Mason B. D., Wycoff, G. L., Urban, S. E., 2002, A&A, 384, 180

Hanslmeier, A., Dvorak, R., 1984, A&A, 132, 203

Ford, E. B., Gaudi, B. S., 2006, ApJ, 652, 137

Ford, E. B., Holman M. J., 2007, ApJ, 664, 51

Funk, B. Schwarz, R., Pilat-Lohinger, E., Süli, Á., Dvorak, R., 2009, P&SS, 57, 434

Laughlin, G., Chambers, J. E., 2002, AJ, 124, 592

Mason, B. D., Gies, D. R., Hartkopf, W. I., 2001, ASSL, 264, 37

Mayor, M., Udry, S., Halbwachs, J.-L., Arenou, F., 2001, Proceedings IAUS. 200, 45

Robutel, P., Gabern, F., 2006, MNRAS, 372, 1463

Schwarz, R., Pilat-Lohinger, E., Dvorak, R., Érdi, B., Sándor, Zs., 2005, AsBio, 5, 579

Schwarz, R., Süli, Á., Dvorak, R., 2009, MNRAS, 398, 2085

Schwarz, R., Süli, Á., Dvorak, R., E. Pilat-Lohinger, 2009, CeMDA, 104, 69

Tokovinin, A. A., 1996, A&A, 124, 75

Verschueren, W., David, M., Brown, A. G. A., 1996, Proceedings of an international symposium, Calgary, ASP Conf., 90, 131

PADEU PADEU **20**, 145 (2011)
ISBN 963 463 557

PLANET FORMATION

Áron Süli

Eötvös University, Department of Astronomy, H-1518 Budapest, Pf. 32, Hungary

E-mail: `a.suli@astro.elte.hu`

Abstract
Models of planetary formation are developed based on the observation of our Solar System, star-forming regions and circumstellar disks and on an the ever increasing number of exoplanetary systems. The solar nebula theory and the planetesimal hypothesis are discussed. The latter is found to provide a viable theory of the growth of the terrestrial planets, the cores of the giant planets, and the smaller bodies present in the Solar System. The formation of solid bodies of planetary size should be a common event, at least around young stars which do not have binary companions orbiting at planetary distances. Stochastic impacts of large bodies provide sufficient angular momentum to produce the obliquities of the planets. The masses and bulk compositions of the planets can be understood in a gross sense as resulting from planetary growth within a disk whose temperature and surface density decreased with distance from the growing sun.
Keywords: *planet formation – solar system*

1 Introduction

The origin of the Solar System is one of the most intriguing problem of science. For more than two centuries, scientific ideas about how the planets came to be were based almost entirely upon theory. There were few constraints on such speculations: astronomers knew that stars rotated and that the Sun's planet are in almost circular orbits. But beyond these meager knowledge, those who speculated on the Solar System's origin had nowhere to turn except to their own fantasy of how a gigantic amount of cosmic matter might have organized itself into a Sun and planetary system. Astronomers, using the laws of physics as then understood, offered variations on the same answer: the Sun and the planets were born form a rotating disk of cosmic gas and dust. The flattened form of the disk constrained the planets that formed from it to have orbits lying in more or less the same plane, all moving in the same direction the disk had turned. This hypothetical disk, the *solar nebula*, is where any discussion of the origin of our Solar System must begin.

The idea of the solar nebula was first proposed by Emanuel Swedenborg (1734), and further developed in the course of the 18th century by the Prussian philosopher and physicist Immanuel Kant (1755). Although his treatment of the problem was only qualitative, its precepts were remarkably similar to those considered fundamental today. Kant pictured an early universe evenly filled with thin gas. He thought such a configuration would have been gravitationally unstable, so it must have drawn itself together into many large dense clumps of gas. Kant correctly assumed that these clumps of gas were rotating and also recognized the importance of this rotation: as they shrank the rotation spun them out into flattened disks. From one of these disks was our Solar System forged.

The first indirect evidence for disks came from studies of *T Tauri stars*, which are similar in mass to our Sun but very young - roughly a million years old. In the 1980s astronomers realized that about a third of T Tauri stars have "infrared excesses", that is, the amount of infrared radiation they emit is too great to be consistent with their output at visible wavelengths. This can be understood if the stars in question are surrounded by halos of dust kept warm by short-wavelength radiation from the stars; the dust then reradiates the energy it receives at longer (infrared and radio) wavelengths. However, the strong infrared signatures implied the presence of enough dust, if distributed evenly in a sphere, to completely block our view of such a star at visible wavelengths. Only if the dust were arranged in a flattened disk, tilted somewhat to our line of sight, could we expect to see the star itself.

The observational evidence of disks around young stars that were first directly observed in the mid 1980s, initially in the form of dusty debris disks such as those seen around Vega (Aumann et al. , 1984) and β Pic (Smith & Terrile , 1984), and later in the form of the gas-rich disks that we now term "protoplanetary" (Sargent & Beckwith , 1987). Advances in telescope technology in the intervening two decades has resulted in the detection, both directly and indirectly, of many more disks around young stars, and these protoplanetary disks, or *proplyds*, are now understood to be commonplace. The Hubble Space

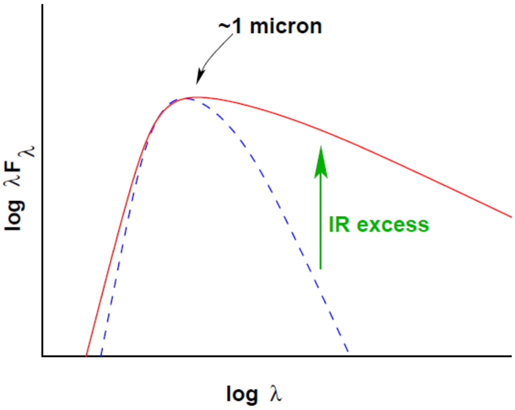

Figure 1: *Spectral energy distribution of the dust around a solar-type star.*

Figure 2: *Examples of "proplyds" (protoplanetary disks) observed by Hubble Space Telescope in the Orion Nebula. At the center of each is a young, energetic T Tauri star. The disks surrounding them are two to eight times the diameter of our Solar System.*

Telescope could capture such disks at visible wavelengths in the Orion nebula, an active stellar forming region (Fig. 1). The Orion disks are far larger than the Solar System, and the available material in them are more than enough for planetary systems. The host stars of these disks are very young, at most a few million years old.

Today we realize that Kant, by and large, got it right, and the widely accepted model, the *Solar Nebula Disk Model*, also known as the *Planetesimal Hypothesis* roots in the same fundamentals as Kant's theory. The development of the Solar Nebula Disk Model (hereafter SNDM) has interwoven a variety of scientific disciplines including astronomy, physics, geology, and planetary science. Since the dawn of the space age in the 1950s and the discovery of proplyds and extrasolar planets in the 1990s, the models have been both challenged and refined to account for new observations.

The first unambiguous discovery of an exoplanet around a main sequence star 51 Peg was announced on October 6, 1995 by Mayor & Queloz (1995). In order to better understand the physical processes involved in the formation of planetary system it is inevitable to observe and study a large sample of extrasolar system. By now this is exactly the situation: since the detection of the planetary companion of 51 Peg the number of exosystems has exceeded 300 providing several constraints and a striking variety of planetary systems for scientist to formulate a general theory for planet formation. On the other hand theoretical studies of planetary formation have become another front line research in the field of astronomy.

2 Stages of planet formation

The process of planetary growth is generally divided for convenience into several distinct stages. The currently accepted sequence of planetary formation is outlined in the following sections.

2.1 Early stage: from dust to planetesimals

In what follows I shortly discuss how dust grains grow from sub-μm sizes to $\sim$ km-size bodies. As the temperature T decreases various chemical compounds condense into microscopic grains ($\leq 10^{-6}$ m). Preexisting condensates from the interstellar matter may also be present. Growth of particles then proceeds by collision.

Observations of dusty disks around T-Tauri stars imply that $\geq 1\%$ of the condensed matter remain in dust phase, which may indicate that collision of particles do not by all means lead to agglomeration of the solid particles. Alternatively it may result from the disruptive collisions between planetesimals, when large amount of dust are ejected.

The motions of small grains in a proplyd are strongly influenced by the gas. The coupling between the gas and the solids with diameter $\leq$ 1 cm is well described by Epstein's drag law, whereas larger bodies are subject to Stokes drag (Adachi et al. , 1976).

The gaseous component of the proplyd is partially supported against the stellar gravity by a pressure gradient in the radial direction, so gas rotates around the star slower than the local Keplerian velocity.

Larger particles (≥ 10 cm) moving at nearly Keplerian speed thus encounter a headwind, which removes part of their angular momentum and causes them to spiral towards the star. Inward drift is greatest for mid-sized particles, which have large surface area to mass ratios and orbit with approximately Keplerian velocities. This inward migration effect is hardly relevant for (*i*) small particles (≤ 1 mm), which are so strongly coupled to the gas that the headwind they experience is very weak and for (*ii*) large bodies (≥ 1 km) whose angular momentum is much larger than that of the gas they collide during one revolution. Peak rates for inward drift occur for particles that collide with roughly their own mass of gas in one orbital period. These bodies have radius approximately 1 meter and drift in the terrestrial region of the solar nebula at a rate of up to $\sim 10^6$ km/yr, i.e. a body with mass in the range between 10^2 g and 10^8 g has a decay time at 1 AU as short as 10^2 or 10^3 years! Thus, the material that survives to form the planets must complete the transition from cm size to km size rather quickly.

This problem is the "crux" of the SNDM: How to form planetesimals remains the biggest challenge for modern research in planet formation, and many of the details of this problem still elude us. More recently, several authors have proposed different mechanisms (e.g. aggregation of dust can occur within turbulent eddies) that may provide solutions to the *meter-size problem*. Once this meter-size barrier is passed, continued growth via binary accretion leads to the formation the so called *planetesimals*. In what follows it is supposed that at the end of the early stage a large number of planetesimals orbit the Sun. The settling time of the disk dictates the formation timescale for planetesimals. Most models predict a few 10^4 years.

2.2 Middle stage: from planetesimals to protoplanets

The star's gravity is the dominant force upon planetesimals. The largest perturbation to the orbit of a planetesimal is the gravitational interaction with other solid bodies. The most important non-gravitational forces experienced by a planetesimal is the mutual inelastic collision (kinetic energy is not conserved) and gas drag. Gravitational torques may lead to significant orbital evolution of bodies larger than a typical planetesimal.

2.2.1 Runaway growth

While gas is still present in the disk eccentricities and inclinations of planetesimals are damped due to aerodynamic gas drag. This counteracts the net effect of collision and scattering and as a result velocities remain low. The simplest accretion picture was first quantified by Safronov (1969). Consider a sphere of radius R moving with velocity v through a uniform medium of density ρ. Then the accretion rate is

$$\frac{dm}{dt} = \pi R^2 \rho v. \tag{1}$$

This rate is the geometrical accretion limit, and $\dot{m} \sim m^{2/3}$. However, the gravity of the body plays an important rôle by gravitationally enhancing the cross-section of the body. This effect was first recognized by Safronov: bodies that are larger than the typical size can accelerate their growth rate due to *gravitational focusing* (i.e. gravitationally enhancing the cross-section) (Safronov , 1969; Greeberg et al. , 1978):

$$\frac{dM}{dt} = \pi R^2 \left(1 + \left(\frac{v_{\rm esc}}{v_{\rm rand}}\right)^2\right), \tag{2}$$

where R is the body's physical radius, $v_{\rm esc} = k\sqrt{2M/R}$ is the escape velocity from the body's surface, and $v_{\rm rand}$ represents the velocity dispersion of planetesimals. The second term in the parentheses represent the gravitational enhancement of the accretion cross-section. The quantity $2\theta = v_{\rm esc}/v_{\rm rand}$ is known as the *Safronov number*, and $1 + 2\theta$ is referred to as the *gravitational enhancement factor*.

The runaway growth phenomenon has been seen in numerical simulations (cf. **?**Kokubo & Ida (2000)). Their results show that the most massive bodies have significantly smaller eccentricities than the remainder of the population, presumably they have been damped by dynamical friction (equipartition of the kinetic energy). With runaway accretion the timescale for growth reduce to $\leq 10^5$ years. The simulations indicate that the typical separation between protoplanets formed in this phase is $\approx 4 - 10$ mutual Hill-radii.

The mass of the protoplanets depends on the assumption of planetesimal sizes. In a swarm of $m = 10^{23} - 10^{24}$g (radius 200 - 400 km) planetesimals, Ida & Makino (1992a,b) calculated $\sim 10^{-3} - 10^{-2} M_\oplus$, where the mass of the Earth, $M_\oplus \approx 6 \times 10^{27}$g. Considering a perhaps more realistic population of planetesimals with mass $\approx 10^{19}$g, for the protoplanets $\sim 10^{-5} - 10^{-6} M_\oplus$ are obtained. Thus, although runaway accretion is much more rapid than other modes of accretion (see oligarchic growth below), it ceases long before protoplanets approaching an Earth mass can form.

2.2.2 Oligarchic growth

As it was discussed above the initial growth mode in a disk of accreting planetesimals is runaway growth, where the mass doubling time for the largest bodies is the shortest. Runaway growth allows relatively short formation times and it is followed by a more lengthy phase of oligarchic growth mode when the largest bodies are still orders of magnitude below an Earth mass. The timescale of oligarchic growth dominates over that of runaway growth.

The oligarchic growth phase begins when the dynamical friction of the planetesimals is insufficient to keep the eccentricities and inclinations of the protoplanets very low. In such a configuration protoplanets are not sufficiently isolated from one another to be dynamically stable for a long period of time. Mutual gravitational scattering eventually pump up the relative velocities of the protoplanets which decreases the collisional cross-sections and hence increases the accumulation time. During the oligarchic growth the protoplanets clear their feeding zone by either agglomerating the remaining planetesimals or ejecting them out of the zone.

The final mass of the protoplanets can be approximated by the mass available within the feeding zone. For the case of a protoplanet on a circular orbit the standard theory of the restricted three body problem places an upper bound on the initial semi-major axis separation b_H, that may lead to collision. It is convenient to introduce Hill-scaled units for planetesimal with mass m, eccentricity e, inclination i, separation in semi-major axis a from the protoplanet:

$$e_H \equiv \frac{ea}{h}, \quad i_H \equiv \frac{ia}{h}, \quad b_H \equiv \frac{\Delta a}{h}, \tag{3}$$

where $h = (m/3M_*)^{1/3}a$ is the Hill sphere of the protoplanet and M_* is the mass of the star in solar units. Neglecting gas drag and interactions with other planetesimals, a planetesimal whose orbital elements satisfy the inequality:

$$\frac{3}{4}b_H^2 - e_H^2 - i_H^2 \geq 9 \tag{4}$$

cannot enter the protoplanet's Hill sphere. For $e_H = 0$ and $i_H = 0$ this inequality gives $b_H \geq 2\sqrt{3} \approx 3.46$. Planetesimals on circular orbit and with zero inclination with initial separation b_H less than $2\sqrt{3}$ will suffer a close encounter and eventually merge with the protoplanet. Thus the accretion zone, often referred to as the *feeding zone* embedded in a disk of low random velocity extends over the region

$$b_H \leq B, \tag{5}$$

where B depends on the magnitude of other perturbations on the planetesimals, and typically is $\sim 3.5 - 4$ in a quiescent disk.

Assuming that a protoplanet at astrocentric distance r has accreted all the solid material within an annulus of width $2\Delta r$ is

$$M = \int_{r-\Delta r}^{r-\Delta r} 2\pi r' \sigma(r') dr' \approx 4\pi r \Delta r \sigma(r). \tag{6}$$

Setting $\Delta r = Bh = Br(m/3M_*)^{1/3}$, one obtains from Eq. (5) the isolation mass to which a protoplanet during the oligarchic growth phase may grow:

$$M = \frac{\left(4\pi B r^2 \sigma\right)^{3/2}}{\left(3M_*\right)^{1/2}} = 2.1 \times 10^{-3} \left(\frac{Br^2\sigma}{2\sqrt{3}}\right) \left(\frac{M_\odot}{M_*}\right) M_\oplus \tag{7}$$

For example, assuming $B = 2\sqrt{3}$, a minimum mass solar nebula with $\sigma = 10$ gcm^{-2} at 1 AU implies protoplanet isolation at 0.066 $M_\oplus$; whereas $\sigma = 3$ gcm^{-2} at 5 AU implies protoplanet isolation at 1.36 $M_\oplus$.

Therefore at the end of this phase only such protoplanets are formed, whose masses are a few percent of the Earth mass in the terrestrial region, and roughly an Earth mass at Jupiter. One possibility to get larger mass is to start with more than the minimum mass solar nebula. In this case the excess material must be clear away. This can easily happen in the vicinity of Jupiter as that planet is large enough to eject the bodies, but in the terrestrial region, where material resides deep in the potential well of the Sun, it is not evident how the extra material would be lost.

2.3 Late stage: from protoplanets to terrestrial planets

At the end of the middle stage we have a regular distribution in a of the protoplanets with roughly constant mass. There is also a swarm of smaller planetesimals, which may or may not be relevant. At the beginning of the late stage a.k.a *giant impact* phase, most of the mass is contained in protoplanets, so dynamical friction is no longer playing an important rôle in their orbital evolution. Even if protoplanets form in circular orbits, mutual gravitational perturbations among several bodies can induce eccentricities of ~ 0.01, which is sufficient to enable their orbits to cross so the bodies can suffer close encounters. These are the initial conditions for the last stage of planet formation.

In this stage there are to few bodies to use statistical methods, therefore to track the evolution of the system one must use direct N-body integration methods. Once the protoplanets have perturbed one another into crossing orbits, their subsequent orbital evolution is determined by close encounters and collisions. Almost all simulations performed to date assume that the collisions are inelastic and all the material in the colliding bodies end up in the resulting body of the collision. However, giant collisions between protoplanets may not always be accretionary: high-speed or off center collisions can actually erode the body.

For dynamical environments typical of late-stage accretion models Agnor & Asphaug (2004) estimated that more than half of all collisions between same-sized planetary embryos do not result in accumulation into a larger body. While their initial results are limited to a single mass ratio, they suggest that non-accretionary collisions are typical during the end of terrestrial planet formation. The collisional and dynamical accretion of planets are coupled. For example, the reduced accretion efficiency appears to lengthen the timescale of planet formation by a factor of 2 or more, relative to perfect mergers. The production of significant erosional debris, however, might alter the dynamical environment in ways that remain largely unexplored - for instance, damping the system to lower relative velocities.

Benz et al. (1988) simulated giant collision between a proto-Mercury and a planet one-sixth its size. According to the results it would lead to the loss of most of the silicate mantle of Mercury and thereby account for its anomalously high density. Other simulations in the field lend support to the giant impact hypothesis for the origin of Earth's Moon; during the final stage of accumulation, an Earth-size planet is typically happen to collide with several objects as large as the Moon and often as massive as Mars. The obliquities of the rotation axes of the planets also provide evidence of the giant impacts during this epoch.

This stage of formation was pioneered by Chambers & Wetherill (1998), who simulated the terrestrial-planet formation using N-body integrations, in three dimensions, of disks of up to 56 initially isolated, nearly coplanar planetary embryos, plus Jupiter and Saturn. Gravitational perturbations between embryos until their orbits become crossing, allowing collisions to occur. Further interactions produce large-amplitude oscillations in e and the i and prevent objects from becoming re-isolated during the simulations. The largest objects tend to maintain smaller e and i than low-mass bodies, suggesting some equipartition of random orbital energy, but accretion proceeds by orderly growth. The simulations typically produce two large planets interior to 2 AU, whose time-averaged e and i are significantly larger than Earth and Venus. The accretion rate falls off rapidly with heliocentric distance, and embryos in the "Mars zone" ($1.2 < a < 2$ AU) are usually scattered inward and accreted by "Earth" or "Venus," or scattered outward and removed by resonances, before they can accrete one another. The asteroid belt ($a > 2$ AU) is efficiently cleared as objects scatter one another into resonances, where they are lost via encounters with Jupiter or collisions with the Sun, leaving, at most, one surviving object. Accretional evolution is complete after 3×10^8 years in all simulations that include Jupiter and Saturn. The number and spacing of the final planets, in the simulations, is determined by the embryos' eccentricities, and the amplitude of secular oscillations in e, prior to the last few collision events.

A large number of simulations were conducted in recent years exploring a wide range of initial conditions. In general the end result of all these simulations is the formation a few (2 - 5) terrestrial planets on a timescale of about 10^8 years. An important feature is that planetesimal orbits execute a random walk in semi-major axis due to successive gravitational encounters. The resulting widespread mixing of material throughout the terrestrial planet region greatly diminishes any chemical gradients that may have existed in the early stages of planetesimal formation.

The above described planet formation mechanism is unlikely to be as purely sequential as layed out. Grain growth and even the accretion of large planetesimals may well begin during the epoch when a proplyd is still accreting and redistributing material. Given that the theories of each of these epochs are still rather primitive, a sequential study of each stage is probably adequate. However, to the extent that planetary growth depends on, e.g. the initial size distribution of planetesimals, one must recognize that various processes currently being treated as separate events occur simultaneously and may effect one another.

3 Conclusions

The planetesimal hypothesis provides a viable theory of the growth of the terrestrial planets, the cores of the giant planets, and the smaller bodies in the Solar System. The formation of giant planets, which contains significant amounts of H_2 and He, requires a rapid growth of planetary cores so that gravitational trapping of gas can occur prior to the dispersal of the gas from the proplyd.

The summarized theory of planet formation provides excellent or acceptable explanations of the causes of several of the 14 observed Solar System properties listed in the Introduction, but less complete or satisfactory for several others. Many issues remain to be solved: the details of planetesimal formation are still poorly understand, although recent results suggest that several process including turbulence and migration of meter-sized bodies acting simultaneously might be the solution. The details and consequences of giant impacts are not well known, in terms of the fate of collisional debris and compositional changes induced by the impacts. Moreover, a number of the effects of the external parameters could be much more decisive in the formation process than we think it now.

An important challenge in the field of observation is that of directly imaging a planet orbiting a solar-type star. The development of a new generation of adaptive-optics systems, promises a great improvement in this field. All these elements will permit us to better understand the mechanisms leading to the formation of planetary systems like our own, and will thus represent an important step toward the search for life in the Universe. Once earth-like planets orbiting in the habitable zone are known, the search for life in these systems will undoubtedly follow. In the very near future, humanity has to prepare itself to find out that the whole Universe may be teeming with life.

Acknowledgement

Á. Süli wants to acknowledge the support by the Hungarian Scientific Research Fund PD-75508. The European Union and the European Social Fund have provided financial support to the project under the grant agreement no. TÁMOP-4.2.1/B-09/1/KMR-2010-0003.

References

Adachi, I., Hayashi, C., Nakazawa, K. 1976, Prog. Theor. Phys., 56, 1756

Aumann, H.H., Beichman, C.A., Gillett, F.C., et al. 1984, ApJ, 278, L23

Agnor, C., Asphaug, E. 2004, ApJ, 613, L157

Benz, W., Slattery, W.L., Cameron, A.G.W. 1988, Icarus, 74, 516

Chambers, J.E., Wetherill, G.W. 1998, Icarus, 136, 304

Greeberg, R., Hartmann, W.K., Chapman, C.R., Wacker, J.F. 1978, Icarus, 35, 1

Ida, S., Makino, J. 1992a, Icarus, 96, 107

Ida, S., Makino, J. 1992b, Icarus, 98, 28

Kokubo, E., Ida, S. 2000, Icarus, 143, 15

Mayor, M., Queloz, D. 1995, Nature, 378, 355

Safronov, V.D. 1969, Evolution of the Protoplanetary Cloud and Formation of the Earth and Planets, Moscow: Nauka. Engl. Transl. NASA TTf-677, 1972

Sargent, A.I., Beckwith, S., 1987, ApJ, 323, 294

Smith, B.A., Terrile, R.J. 1984, Science, 226, 1421

PADEU | PADEU **20**, 157 (2011)
ISBN 963 463 557

Stability of an additional planet in the Gliese 581 exoplanetary system

Zsuzsanna Tóth[1], **Imre Nagy**[2] **and Vera Dobos**[1]

[1]Eötvös University, Department of Astronomy, H-1518 Budapest, Pf. 32, Hungary
[2]Physical Geodesy and Geodesical Research Group of the HAS, Technical University, Műegyetem rakpart 3, 1111 Budapest, Hungary

E-mail: `zsuzsanna.toth@gmail.com`

Abstract

The Gliese 581 planetary system is known to harbour four planets: a Neptune-sized planet, two super-Earths, and a small rocky planet. Using the maximum eccentricity and the minimum distance between the planets, we examine the long-term dynamical stability of this 4-planet system and then, adding a 1-10 M_{Earth} test planet within 0.3 AU, we look for possible stable regions for another planet. The present 4-planet system, over the time span of the 10 Myr integration, does not remain entirely stable. The eccentricity of planet *e* increases significantly and its stability could only be secured in mean motion resonance with planet *b*. The addition of a fifth planet, independently of its mass, introduces instability to the system. As predicted by the Titius-Bode law and a similar but revised formula by Ragnarsson (1995), another planetary body would be expected between planet *c* and *d* or beyond them. The instability in these regions, however, is caused by the highly eccentric orbits of the two super-Earths.

Keywords: *Gliese 581, planetary systems, N-body simulations*

1 Introduction

In the last few years four exoplanets were discovered around Gliese 581[1], all of them based on precise radial velocity (RV) measurements with the HARPS

---

[1] A recent combination of the HARPS data set with measurements of the HIRES spectrograph at the Keck Observatory recorded over an 11 year time period led to the discovery

vacuum spectrograph at La Silla Observatory in Chile (Bonfils et al., 2005; Udry et al., 2007; Mayor et al., 2009). The observations indicate a 5.37-day hot-Neptune (*b*), a 12.9-day and a 67-day super-Earth planet (*c* and *d*) and a 3.15-day small rocky planet previously announced by Bonfils et al. (2005); Udry et al. (2007); Mayor et al. (2009). See their parameters in Table 2. The dynamical stability of the Gliese 581 planetary system has been the subject of recent stability investigations and was found to be stable (Beust et al., 2008; Mayor et al., 2009).

Due the inherent uncertainty in the RV measurements and that the contribution of a yet unseen planet to the RV signal might be just below the actual measurement uncertainty, we address the possible existence of a fifth planet. Using the maximum eccentricity and the minimum distance between the planets as indicators of dynamical stability, first we investigate the stability of the known 4-planet system, then we add a hypothetical lower mass planet inside the 0.3 AU region from the star, and varying the mass of the test planet, we look for potentially stable configurations.

1.1 Titius-Bode law

In addition to the stability investigations, we also calculated the distances of all planets from the star in the Gliese 581 planetary system based on the Titius-Bode law and a revised formula by Ragnarsson (1995). Although no physically relevant explanation of these empirical formulas has been found, they may nevertheless serve as a tool to predict not yet discovered planetary bodies in exoplanetary systems.

The Titius-Bode law (TBL) states that the semi-major axis of the planets are given, in astronomical units, by the formula $a_n = 0.4 + 0.3 \cdot 2^n,\ n = -\infty, 0, 1, 2, \ldots$ Adjusted to the Gliese 581 planetary system it can be written:

$$a_n = 0.03 + 0.01 \cdot 2^n,\ n = -\infty, 0, 1, 2, \ldots \tag{1}$$

Ragnarsson's new empirical formula (RF) is more accurate in describing the Solar System, and is based on the symmetry in the logarithms of the semi-major axes around Jupiter. Assuming that the hot Neptune in the Gliese 581 system may play the same dominating role as Jupiter in our Solar System, RF can be written:

---

of two more planets (*f* and *g*) in the Gliese 581 planetary system (Vogt et al., 2010). The discovery of Gliese 581g was soon questioned by the HARPS team claiming that their latest report including an additional 60 RV measurements can not confirm the presence of a planet in an orbit of 37 days (Pepe et al., 2010).

$$a_m = a_b \left[(5/2)^{2/3} |m| \right]^{sign(m)}, \; m = n-1, n = 1, 2, \ldots \tag{2}$$

where a_b is the semi-major axis of Gliese 581b, parameter $m = n - 1$ is the "jovicentric" planet number and m is negative for the inner planets (in this case for planet e).

Table 1: *Distances of the planets in the Gliese 581 planetary system based on the Titius-Bode law and Ragnarsson's formula (Ragnarsson, 1995).*

Planet	a [*AU*]	a_{TBL} [*AU*]		a_{RF} [*AU*]	
e	0.03	$n = -\infty$	0.03	$m = -1$	0.0217
b	0.04	$n = 0$	0.04	$m = 0$	0.04
		$n = 1$	0.05		–
c	0.07	$n = 2$	0.07	$m = 1$	0.0737
		$n = 3$	0.11	$m = 2$	0.1474
		$n = 4$	0.19		–
d	0.22	$n = 5$	0.35	$m = 3$	0.221

The distances of the planets calculated from Eq.(1) and Eq.(2) are listed in Table 1. Neither of these formulas seem to give back the actual values perfectly, although both work for three out of the four planets relatively well, in fact, it is remarkable how well RF fits for planet c and d. The TBL predicts three more possible planets, but it is unlikely that at 0.05 AU, very close to the most massive planet, another stable orbit would exist. From the other two predicted planets between planet c and d, the planet at 0.11 AU is indicated by RF as well. Because of this agreement and the overall better fit of RF, the region at 0.14 AU seems to be worth investigating further[2].

2 Model parameters and methods

The 4-planet model of Gliese 581 and the initial orbital elements were taken from Mayor et al. (2009) and are explained in Table 2. Unknown orbital elements were set to zero, and we made the assumptions of coplanarity and $\sin i = 1$ (an edge-on system). For the mass of Gliese 581 we took $0.31 M_\odot$. The integrations were performed using Bulirsch-Stoer integrator, which accurately yields orbital

---

[2] Gliese 581g, the (yet unconfirmed) sixth planet discovered by Vogt et al. (2010) is orbiting at a distance of 0.146 AU from its parent star with an orbital period of 37 days.

positions. In case of the long-term stability investigation, the 4-planet system was numerically integrated over 10 000 000 P_d, where P_d is the orbital period of planet *d*. Instead of fixed time steps, adaptive step-size control was applied: the integrations stopped when the integrator could not reduce the estimated relative error of the next step below a certain accuracy (10^{-10}) in case of the smallest permitted time step, which was set to 1/2000 of the orbital period of the innermost planet.

Table 2: *Parameters of the Gliese 581 planetary system, after Mayor et al. (2009). P: orbital period,* $m_{min} = m \sin i$, *minimum mass, where i is the orbital inclination, a: semi-major axis, e: eccentricity,* ω*: argument of pericentre.*

Planet	P [*days*]	m_{min} [M_{Earth}]	a [*AU*]	e	ω [*deg*]
e	3.15	1.94	0.03	0	0
b	5.36	15.65	0.041	0.02	0
c	12.9	5.36	0.073	0.17	−110
d	66.8	7.09	0.22	0.38	−33

For an indication of stability we used the maximum eccentricity method (e.g. Dvorak (1993); Süli et al. (2005)). The behaviour of eccentricity shows the probability of orbital crossings and close encounters of two planets, therefore its maximum value provides information about the stability of the orbit. Moreover, close encounters were also taken into account through the determination of the distances between the adjacent planets and the relations between their pericentre and apocentre distances. These values indicate whether collision or very close encounter happens, which may significantly alter the orbits of the planets or may also eventually lead to the ejection of the less massive body.

With the addition of the fifth planet, we confined our study area between 0.01 and 0.3 AU. The semi-major axis of the hypothetical planet in this range was varied with steps of 0.01 AU and its mass from 0 to 10 Earth-masses with steps of 0.25, which resulted in altogether 1271 configurations. The integrations were carried out over 50 000 P_d, but we introduced another constraint here: the integrations stopped when the test planet approached the planets within 5% of the mean of their semi-major axes.

3 Results

3.1 Long-term stability (4-planet system)

In Table 3 we list the maximum evolution range of the semi-major axis, the maximum eccentricity, the minimum pericentre and maximum apocentre distances of the four planets from the 10 000 000 P_d integration. To further characterize the long-term stability, the distance between the positions of the planets was calculated at every integration step and from these values the smallest was chosen as a measure of the encounter (D). To describe the vicinity of the adjacent planets' orbits, for each planet pair, the difference between the minimum pericentre of the outer planet and the maximum apocentre of the inner planet was calculated as well (K). To get comparable results these values were normalized by the mean of the original semi-major axes. D, K and the normalized values are listed in Table 4.

Table 3: *Variation ranges for some orbital elements of the Gliese 581 system over the 10 million P_d integration. a_{max}: maximum of the semi-major axis, a_{min}: minimum of the semi-major axis, e_{max}: maximum eccentricity, r_{min}: minimum pericentre distance, r_{max}: maximum apocentre distance.*

Planet	a_{max} $[AU]$	a_{min} $[AU]$	e_{max}	r_{min} $[AU]$	r_{max} $[AU]$
e	0.0313	0.0299	0.2503	0.0231	0.0388
b	0.0408	0.0405	0.1214	0.0357	0.0457
c	0.0731	0.0726	0.1840	0.0595	0.0864
d	0.2200	0.2194	0.3821	0.1357	0.3036

Table 4: *Calculated values characterizing the close encounters of the adjacent planets. See text for details.*

Planet pair	D	K	$\frac{D}{\frac{a_1+a_2}{2}}$	$\frac{K}{\frac{a_1+a_2}{2}}$
$e - b$	0.0081	-0.0031	0.2290	-0.0865
$b - c$	0.0212	0.0139	0.3712	0.2439
$c - d$	0.0512	0.0493	0.3492	0.3362

Stability of the 4-planet system is examined via the following criteria as defined in Dobos et al. (2010). First, the orbit of a planet is considered stable if the difference between its maximum and initial eccentricity is less than 0.2. This criterion is fulfilled for all planets except planet e, for which the difference is slightly more, 0.2203. The second stability condition regards the stability of the orbits of the adjacent planets. A planet pair is considered stable if the ratio of D and the mean of the original semi-major axes (see Table 4 third column) is greater than 0.2. All planet pairs meet this criterion, meaning that there is no such close encounter, which would affect the stability of the orbits. The third criterion also concerns planet pairs, but applies a stronger restriction: the orbits of the planet pairs are considered stable if the the ratio of K and the mean of the original semi-major axes is greater than 0.01. For the e – b planet pair this ratio is less than zero, because the minimum of the semi-major axis of planet b is less than the maximum of the semi-major axis of planet e. This questions the long-term stability of the two inner planets. The other two planet pairs fulfill this condition.

3.2 Stability with an additional planet (5-planet system)

The aim of this investigation was to find regions of possible orbital stability for an additional planet within 0.3 AU. Before analyzing the results of the integrations, because of the applied constraint, we checked the duration of these integrations. This is plotted using a logarithmic scale on Fig.1a as a function of the mass and the semi-major axis of the test planet. It is clearly visible that only a small number of the configurations (for given mass and semi-major axis) could be integrated over the whole time period, this is indicated by the white end of the color scale. Most of the integrations were stopped before (as shown by grey and black), either because the integrator could only have ensured the permitted error with a too small time step, or because a close encounter occured. The orbit of the test planet, independently of its mass, quickly became unstable near the inner planets, planet e and b; it survived only in a few cases with higher masses, mostly between 0.10 and 0.14 AU, but an extensive stable region did not appear. This means that the lifetime of the 5-planet system rarely reaches 50000 P_d and it is unstable.

To check whether this instability is an artifact showing up because of the applied constraint or simply a characteristic of these 5-planet systems, we made two other test runs: one without the additional restriction in the integration concerning the close encounters and the other one with setting the initial eccentricity to zero for all of the planets. Leaving out the additional constraint did not increase the number of the stable configurations significantly. The duration of the integrations for the system with initial $e = 0$ is plotted on Fig.1b. In this case the integrations reached 50000 P_d for most of the configurations: broad stable regions exist for the fifth planet almost independently of its mass, except

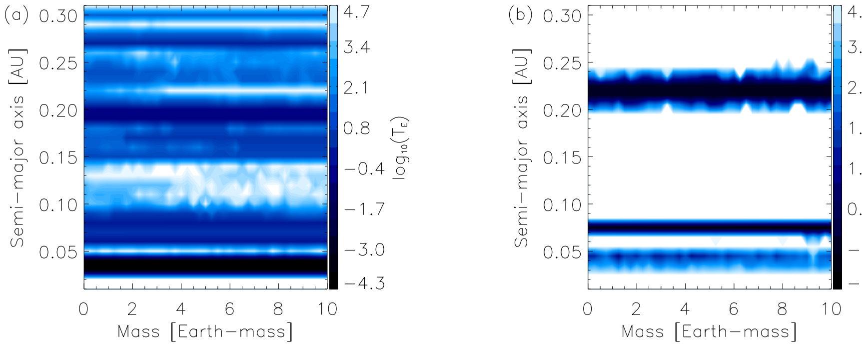

Figure 1: *Duration of the integrations for the different configurations of the 5-planet system, (a) showing the nominal case with $e \neq 0$ and (b) the test run with initial $e = 0$ for all of the planets. The greyscale indicates the lifetime of the different 5-planet systems as a function of the mass and semi-major axis of the fifth planet. White illustrates configurations which survived the longest, while for grey and black the integrations stopped soon after the start.*

only the very close vicinity of the original four planets. These proved that the instability is indeed the characteristic of the 5-planet system.

4 Discussion

The long-term stability investigation with the present 4-planet model showed that the Gliese 581 planetary system does not remain entirely stable over the 10 Myr time period: the eccentricity of planet e increases considerably, and it can cross the orbit of planet b. This can lead to collision or ejection of the lower mass planet e. Mayor et al. (2009) found that the 4-planet system is only stable for sufficiently high inclinations ($i \geq 40°$), otherwise planet e is ejected after a few Myr. Our results show that assuming $i = 90°$ and a coplanar system, which means the use of minimum masses and consequently even the overestimation of stability, stability of the system could only be ensured if the lowest mass innermost planet would orbit the star in mean motion resonance with planet b.

With the addition of a $1 - 10\ M_{Earth}$ planet inside 0.3 AU, the system appears to be extremely unstable and only configurations with a few a, m pairs sporadically remained stable, even during the relatively short time of the integration. Based on the distribution of the planets from their star and as supported by the TBL and RF as well, the possible existence of a fifth planet would be expected between planet c and d or beyond them. The lack of more stable orbits in these regions, however, might be a consequence of the highly eccentric orbits of the two outer super-Earth planets. The apocentre distance of planet c is $r_{max} = 0.0819AU$, while the pericentre distance of planet d is $r_{min} = 0.1364AU$, hence there is only a narrow region between them where another planetary body could longer occupy a stable orbit. The possibility of another planet is not ruled out completely, but it must have special orbital elements or it must be in resonance to avoid collision or ejection by the adjacent planets. This naturally raises the question whether we see the Gliese 581 planetary system in its original state – although this would require planetary formation and evolution theories to support the existence of such highly eccentric orbits – or we see a perturbed planetary system, presumably after distortion caused by the gravity of a passing star nearby.

Eccentricities also might be lower for planet c and d, since planet searches in RV data yield only a best approximate solution by fitting a number of planets and some of their assumed orbital elements. The best fitted solution may improve with the incorporation of newly acquired data: the present 4-planet solution for the Gliese 581 RV data may not describe the planetary system perfectly and the orbital elements of the planets may be different from the presently known values[3].

Acknowledgement

We thank Áron Süli for the BS integrator. The European Union and the European Social Fund have provided financial support to the project under the grant agreement no. TÁMOP-4.2.1/B-09/1/KMR-2010-0003.

References

Beust, H., Bonfils, X., Delfosse, X., Udry, S. 2008, A&A, 479, 277

von Bloh, W., Bounama, C., Cuntz, M., Franck, S. 2007, A&A 476, 1365

Bonfils, X., Forveille, T., Delfosse, X., Udry, S., et al. 2005, A&A, 443, 15

---

[3] The 6-planet solution of Vogt et al. (2010) assumes circular orbits for all of the planets and allowing eccentricities to vary did not significantly improve the fit. This indicates that there is potentially a different interpretation for the RV data that does not require the assumption of such highly eccentric orbits.

Dobos, V., Nagy, I., Orgoványi, J. 2010, J. Phys. Conf. Ser. 218, 012019

Dvorak, R., Pilat-Lohinger, E., Funk, B., Freistetter, F. 2003, A&A, 410, L13

Mayor, M., Bonfils, X., Forveille, T., Delfosse, X., Udry, S., et al. 2009, A&A, 507, 487

Pepe, F., Benz, W., Bouchy, F., Lovis, C., Mayor, M., et al. 2010, IAU Symposium 276, The Astrophysics of Planetary Systems: Formation, structure, and dynamical evolution. Torino, Italy, 11-15 October 2010.

Ragnarsson, S.I. 1995, A&A, 301, 609

Selsis, F., Kasting, J. F., Levrard, B., Paillet, J., Ribas, I., Delfosse, X. 2007, A&A, 476, 1373

Süli, Á., Dvorak, R., Freistetter, F. 2005, MNRAS, 363, 241

Udry, S., Bonfils, X., Delfosse, X., Forveille, T., Mayor, et al. 2007, A&A, 469, 43

Vogt, S. S., Butler R. P., Rivera, E. J., Haghighipour, N., Henry, G. W., et al. 2010, ApJ, 723, 954

Zollinger, R., Armstrong, J.C. 2009, A&A, 497, 583

Part Three

Miscellaneous

PADEU | PADEU **20**, 169 (2011)
ISBN 963 463 557
© Published by the Astron. Dept. of the Eötvös Univ.

Chaos in open Hamiltonian systems

Tamás Kovács and Holger Kantz

Max Planck Institute for the Physics of Complex Systems, Noethntizer str. 38. D-01187, Dresden, Germany

E-mail: `tkovacs@pks.mpg.de`

Abstract

In this study we show a complex structure of the Hamiltonian phase space taking into account the phenomena of chaotic scattering, i.e. when the system is open. This extended investigation gives us a qualitative overview about the invariant chaotic saddle which is responsible for finite time irregular behavior. Numerical results confirm that an invariant fractal set can be found in the phase space of these systems. Moreover, due to the mixed phase space structure two different part of the chaotic saddle can be identified. The first, where the number of non-escaping trajectories decreases exponentially, corresponds to the hyperbolic part of the saddle. The other one includes the trajectories that may come close to the KAM islands, number of such orbits follow power law decay.

Keywords: *Escape times, chaotic scattering, stable and unstable manifolds, invariant saddle*

1 Introduction

Since the middle of 1980s when it was shown (Kantz & Grassberger , 1985) that the chaotic transients play an important role in various dynamical systems, a huge number of studies appeared dealing with this phenomenon. Nowadays it is an established fact that the manifestation of transient effects in conservative systems is the chaotic scattering (Ott & Tél, 1993). Escapes from open Hamiltonian systems, stickiness trajectories around the last KAM tori (Dvorak , 1993), stable and unstable manifolds are common concepts in studies related to conservative mechanics (Ott , 2002; Contopoulos et al. , 2002). One can also find many papers in celestial mechanics dealing with finite time chaotic behavior, however, only few of them mention the chaotic saddle which plays a crucial role in the transient chaos.

In this paper we have investigated three well-known simple dynamical systems. The first one, the Sitnikov problem (Sitnikov , 1960), is an excited system with a time dependent potential. Strictly speaking this configuration yields the "exact" scattering process, since the test particle can come far from binaries plane along a straight line and it interacts with the scatterer objects close to their common barycenter. This interaction almost results in an escape after several oscillations around the barycenter. Nevertheless, it can happen that the test particle being trapped and does not leave the system anymore but in this case the initial conditions of the motion have to be on the stable manifold of the chaotic saddle (Kovács & Érdi, 2009), we will see this in latter sections. The other two systems are described by autonomous Hamiltonian; the planar Hill problem (Simó & Stuchi , 2000) and the motion of an individual star in a potential close to the center of a galaxy (Contopoulos & Efstathiou , 2004). In these systems escape can occur when the energy is above the escape energy. This means that the test particle can leave the system sooner or later. One can imagine this process as a "half scattering" similar to the ionization of an atom (Uzer et al. , 2006). Our aim is to show, using numerical methods, that the scattering processes in conservative systems are related to chaotic saddles and their manifolds.

2 The model systems

First we give the Hamiltonian of the Sitnikov problem which describes the motion of a mass-less particle along a straight line. This line is perpendicular to the primaries plane and cross it at the common barycenter of the primaries. The primaries are massive bodies with equal masses gravitating each other on Keplerian ellipses. The Hamiltonian reads

$$H(z,\dot{z},t) = \frac{\dot{z}^2}{2} - \frac{2}{\sqrt{z^2 + r(t)^2}}, \tag{1}$$

where z and $\dot{z}$ are the distance to the barycenter and the velocity of test particle, respectively, $r(t)$ is the relative distance between the primaries. If the eccentricity is zero $r(t)$ is constant and the motion is integrable. Allowing eccentric orbits various type of chaotic motion appear in the system. The phase space structure of the Sitnikov problem is well-mapped (Dvorak , 1993). In the present work we have investigated the scattering of the test particle. As it is mentioned in the previous section, the third body can oscillate around the barycenter of the primaries. These oscillations can be periodic, quasi-periodic, or aperiodic corresponding to the elliptic fixed points, KAM curves, and chaotic bands in the phase plane, respectively. If we chose arbitrary initial conditions outside the stable islands, the mass-less body comes close to the primaries plane, makes some oscillations and then escapes to infinity. The motion during these oscillations is aperiodic, i.e. chaotic for finite time, after leaving the system the complex motion ceases.

Our second example is the planar Hill problem. In this particular case of the restricted three-body problem we use Hill's variables, a transformation which allows us to investigate the neighborhood of secondary planet in detail. The Levi-Civita regularization brings the Hamiltonian into the form of two uncoupled harmonic oscillators perturbed by the Coriolis force and the Sun action (Simó & Stuchi , 2000).

$$H(q_1, q_2, \dot{q_1}, \dot{q_2}) = \frac{1}{2}(\dot{q}_1^2 + \dot{q}_2^2 + q_1^2 + q_2^2) - 6(q_1^2 + q_2^2)(q_1^2 - q_2^2)^2. \tag{2}$$

Here q_i are the regularized coordinates and $\dot{q_i}$ are the conjugated momenta. At lower energies one can distinguish two different type of motion, the direct Moon-like motion and the retrograde lunar motion. When the energy increases, the region corresponding to direct motion becomes more and more chaotic. Beyond a critical value of energy zero velocity curves open and trajectories from previous chaotic domain can escape. A detailed study of dynamics and center manifolds can be found in Simó & Stuchi (2000).

Escapes have been studied by Contopoulos & Efstathiou (2004), for the Hamiltonian:

$$H(x, y, p_x, p_y) = \frac{1}{2}(p_x^2 + p_y^2 + A_x^2 + B_y^2) - \epsilon xy^2, \tag{3}$$

with $A = \omega_1^2 = 1.6$, $B = \omega_2^2 = 0.9$, and $\epsilon = 0.08$. Eq. (3) describes a simple approximation of the central region of a galaxy. As it is expected, regular and chaotic orbits also exist below the escape energy. When the energy goes just beyond the escape value almost all chaotic orbits escape to infinity. The higher the energy the larger the escape region becomes and beyond some critical value of energy the islands of stability disappear.

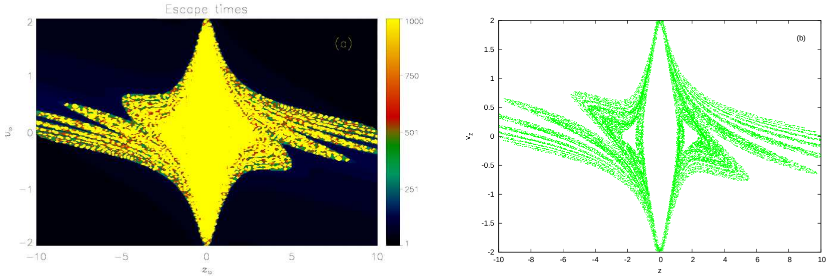

Figure 1: *(a) Escape times in Sitnikov problem. The brighter the color the higher is the escape time. Filamentary structure of the stable manifold is well-visible far from the stability islands. The preselected box is* $-10 < z < 10$. *Time units on colorbar mean the revolutions of primaries. (b) The stable manifold of the chaotic saddle in Sitnikov problem. Trajectories that leave the system backward in time trace out the stable manifold in domain* $-8 < z < 8$. *The two relatively large white islands around* $z \pm 1.8$ *correspond to the 2:1 resonance. The eccentricity is* $e = 0.2$.

3 Chaotic scattering

In this Section we determine the chaotic saddle and its manifolds numerically. The chaotic saddle can be considered as the union of all the hyperbolic periodic orbits on the saddle and of all the homoclinic and heteroclinic points formed among their manifold (for the precise definition see Tél & Gruiz (2006)). One will see that we can identify the fractal set in phase space which is responsible for finite time chaotic behavior in all three systems. We have not focused on the quantitative description of saddles (escape rate, average chaotic lifetime, Ljapunov exponents), we give just a qualitative picture about the structure of these objects.

In hyperbolic systems where transversality holds, i.e. the manifolds of the hyperbolic periodic orbits do not touch each other or cross near tangently, the number of non-escaping trajectories from a predefined region of the phase space decreases exponentially. However, this is not the case in systems with mixed phase space. In such systems the exponential decrease also exists far from the

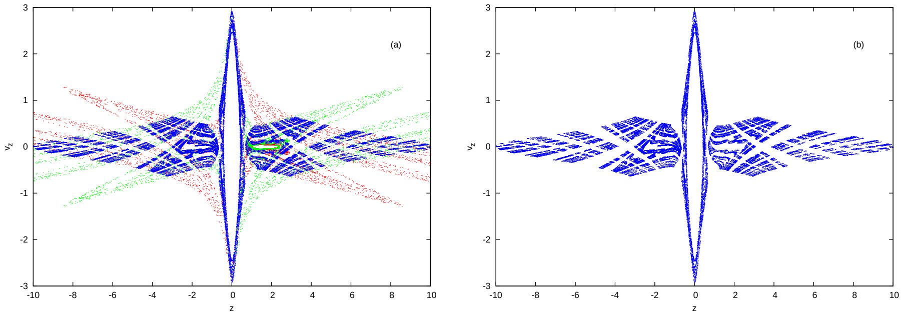

Figure 2: *(a) The stable (red) and the unstable (green) manifold of the chaotic saddle in Sitnikov problem. Corresponding to the definition, the chaotic saddle (blue) can be considered as a common part of its manifolds. (b) Chaotic saddle determined numerically. The accordance is perfect. The eccentricity is* $e = 0.57$.

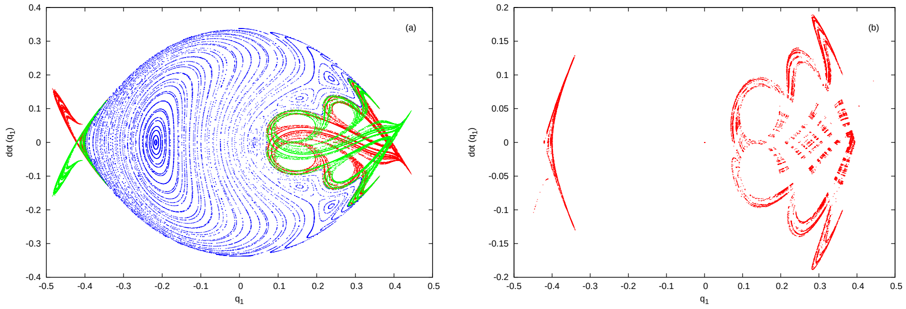

Figure 3: *Poincaré sections of Hill's problem. (a) Above the escape energy, the retrograde motion is more resistant against the perturbation than the direct Moon-like motion (later located previously around* $q \approx 0.2$ *and* $\dot{q} = 0$*). Stable (green) and unstable (red) manifolds of the saddle can be identified in the escape region. (b) The chaotic saddle has the double fractal structure away from the edge of regular motion. The regularized Jacobian constant is* $h = 0.057$.

stable regions but in the vicinity of the regular islands a power-law decay can be observed (Cristadoro & Ketzmerick , 2008). This different behavior is due to the Cantori situated around the stable islands. The very dense debris of destroyed KAM tori can be found in this region. It is clear that these objects are responsible for the stickiness effect in conservative systems (Efthymiopoulos et al. , 1999). Additionally, we notice that Cantori belong to the chaotic saddle.

In fact the chaotic saddle has two different parts. One of them, the hyperbolic part, can be found far away from regular islands. Its fractal dimension is between 1 and 2 corresponding to the partial dimensions along the stable and unstable manifolds (Hsu et al. , 1988). Trajectories that escape from the system after a short time evolve chaotically on this part of the set. The other part of the saddle, the non-hyperbolic one, is located close around the quasi-periodic islands. The structure of this part of the saddle is very similar to chaotic bands located between the invariant curves around a stable periodic orbit. Both are formed from the remnants of destroyed KAM tori. However the difference is that trajectories wandering chaotically outside around the last KAM torus can escape after some time to infinity, contrary to those which are located between two invariant tori and cannot cross them, therefore cannot escape from the system although the motion is chaotic forever.

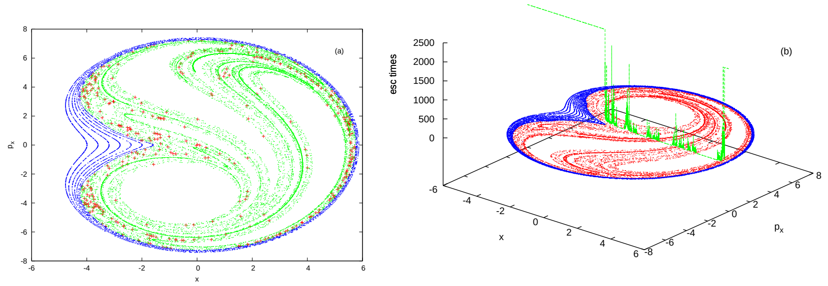

Figure 4: *(a) Invariant curves around the chaotic domain at the center of a galaxy. Red crosses represents 2000 trajectories slightly before leaving the system. Each cross is located on the unstable manifold (green) of the chaotic saddle. (b) The stable manifold surrounded by KAM curves (blue). One can identify the large escape times (green line) "above" the stable manifold (red curve). Parameters can be found in the text.*

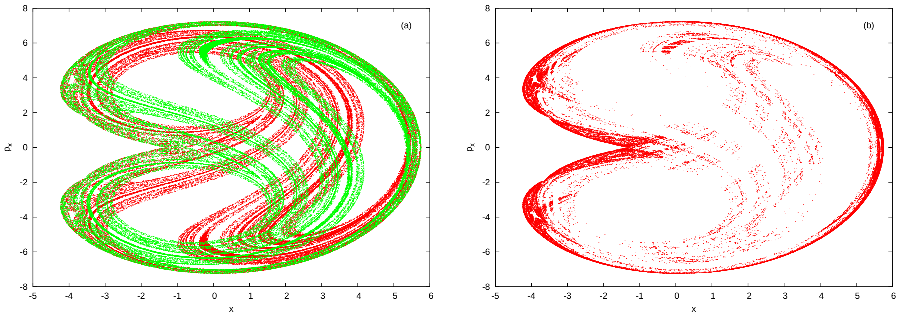

Figure 5: *Poincaré surfaces of section of Hamiltonian (3) for Jacobian constant* $h = 29$. *(a) The stable and the unstable manifold of the chaotic saddle. (b) Numerically determined chaotic set.*

3.1 Escape times, invariant manifolds, and chaotic saddles

First we demonstrate the relationship between escape times and the stable manifold. Let us consider the Sitnikov problem. We can make a contour plot that contains initial conditions and corresponding escape times (Fig. 1). Initial conditions have been chosen from a preselected domain of the phase space ($-10 < z < 10$). If the test particle leaves this area, the calculation stops and the actual time is stored, we regard this time as the escape time. In fact, a trajectory escapes when its energy becomes larger than zero. In Fig. 1a the bright regions correspond to higher escape times. Obviously, the inner part of the phase portrait contains invariant curves, trajectories originating from these initial conditions never escape the system. Trajectories in chaotic band cannot cross the KAM tori neither inward, nor outward, therefore, these initial conditions are also colored with brighter colors. Surprisingly, bright filaments can be found far from inner region. For instance at $z = 8$ we cannot identify any KAM curves but there are several trajectories remaining in the system up to 1000 revolution of primaries.

The escaping trajectories actually leave the system along the unstable manifold of the hyperbolic periodic orbits (Contopoulos & Patsis , 2006). We know that the union of the unstable manifolds form the unstable manifold of the saddle. Hence integrating backward in time, due to the conservative nature of the dynamics, one can have trajectories that follow the stable manifold of the saddle and escape from the system when $t < 0$. We plotted in Fig. 1b the escaping trajectories slightly before they leave the preselected region backward in time.

Note that the correspondence with Fig. 1a is not perfect because the stable (and also the unstable) manifold does not contain the regular islands. Correctly, the escape times trace out the stable manifold and the regular domains in phase space, however, trajectories located in ordered region are not involved in scattering process.

Determining the stable and unstable manifolds numerically is not a hard task. It is worth having first the manifolds because then we can identify much more faster the chaotic saddle. A quite convenient procedure to compute the saddle can be found in Tél & Gruiz (2006). We are not going into the details only give a brief overview of the required steps:

1. (a) We have to find the suitable initial conditions covering a part of the saddle. One can be sure being on the saddle when the number of non-escaping trajectories decreases exponentially, in this case the dynamics is hyperbolic.
2. (b) The average lifetime of chaos can be determined from the escape rate. The escape rate is the slope of the straight line fitted to the half logarithmic plot of the exponential decay.
3. (c) Choosing the integration time (t_0) 3-4 times the average lifetime of chaos should be enough to construct the saddle.

If the first step comes true, this necessarily implies that the initial conditions were in the vicinity of the stable manifold of the saddle. Simultaneously, the end-points must be close to the unstable manifold of the saddle. The mid-points of these trajectories ($t \approx t_0/2$) are then certainly in the vicinity of the saddle.

After the stable and unstable manifolds are identified, we are able to choose initial conditions from the region where they cross each other. Accordingly to the definition, the intersections of the manifolds are good starting points to determine the entire saddle numerically, as it is shown below.

Fig. 2a and 2b show the invariant manifolds and the saddle in the Sitnikov problem. One can compare the intersection points on the panel (a) with the fractal structure plotted on panel (b). The accordance is well-visible. The islands of 2:1 resonance are marked on panel (b). When we magnify the object close to the regular islands we can see that the saddle becomes denser than in outer regions. This phenomena is related to the power-law decay of trajectories and also to the stickiness of Cantori surrounding the islands (Efthymiopoulos et al. , 1999; Kovács & Érdi, 2009).

In Hill's problem for Jacobian larger than the escape value, the zero velocity curves open up and trajectories can leave the system. Fig. 3a shows KAM tori and the escape region with the manifolds. Where the stable and unstable manifold intersect transversely a clear double fractal structure has been traced out (Fig. 3b). This domain corresponds to purely hyperbolic dynamics far from regular islands. Close to resonances the manifolds are tangent, the exponential decay of trajectories is not valid anymore, and the saddle becomes a dense fractal set with fractal dimension close to 2. Therefore, this area around the stability islands contains sticky trajectories.

Finally we present how escapes are organized in system (3). Beyond the escaping energy in system (3) trajectories escape the system from the central region. Fig. 4a shows the invariant KAM curves and 2000 trajectories (crosses) which intersect the Poincaré surface before leaving. One can realize that the pall-mall points on the surface of section lie on the unstable manifold. The unstable manifold has been determined by 200000 initial conditions. Fig. 4b shows the stable manifold on (x, p_x) Poincaré sections and the escape times along the line $p_x = 0$. The results are in good agreement with the Sitnikov problem, i.e. the higher escape times belong to the stable manifold.

The stable and unstable manifolds are plotted in Fig. 5a. At the edge of the stable and unstable manifolds KAM tori are situated (not plotted here, see Fig. 4). As it is expected the saddle has a dense structure in this region. However, the inner part of the scattering region provides the hyperbolic part of the saddle (Fig. 5b).

4 Summary

In this paper we presented three simple models of celestial mechanics. It was shown that for certain energies escape can occur in the systems. Trajectories joining in the scattering process can escape the system sooner or later. Our numerical simulations show that there is a well-defined fractal set in the phase space which is responsible for irregular scattering dynamics. Qualitative investigations support the conception that chaotic saddle has two distinguished part, the hyperbolic and the non-hyperbolic one. The later is related to Cantori located at the borders of stable islands. In other words, the non-hyperbolic part is responsible for sticky orbits and it is denser than the hyperbolic part of saddle. The models were investigated for some particular parameter values by choosing other parameter values the shape of the manifolds and the saddle may change significantly, but in general chaotic scattering appears and in this case chaotic saddle can be identified in the phase space as the backbone of finite time chaotic dynamics.

Acknowledgement

The authors thank to Dr. Tamás Tél his useful comments and discussions and also wish to acknowledge the stimulating discussions with Dr. Charalampos Skokos whose encouragement and suggestions have improved the paper.

References

Contopoulos, G.: *"Order and chaos in dynamical astronomy."* Springer, Berlin, Heidelberg, New York, pp. 237-251 (2002)

Contopoulos, G., Efstathiou, K.. 2004, Celest. Mech. Dyn. Astron., 88, 163

Contopoulos, G., Patsis, P.A. 2006, Mon. Not. R. Astron. Soc. 369, 1039

Cristadoro, G., Ketzmerick, R.. 2008, Phys. Rev. Lett. 100

Dvorak, R., Contopoulos, G., Efthymiopoulos, Ch., Voglis, N. 1998, Planetary and Space Science 46, 1567

Dvorak, R.. 1993, Celest. Mech. Dyn. Astron. 56, 71

Eckhardt, B. 1988, Physica D, 33, 89

Efthymiopoulos, Ch., Contopoulos, G., Voglis, N. 1999, Celest. Mech. Dyn. Astron., 73, 221

Hsu, G., Ott, E., Grebogi, C. 1988, Phys. Lett. A, 127, 199

Kantz, H., Grassberger, P. 1985, Physica D, 17, 75

Kovács, T., Érdi, B. 2009, Cel. Mech. and Dyn. Asron., 105, 289

Ott, E.: *"Chaos in dynamical systems."* 2nd Ed., Cambridge Univ. Press, Cambridge, pp. 192-199 (2002)

Ott, E., Tél, T. 1993, Chaos, 3, 417

Simó, C., Stuchi, T.J. 2000, Physica D, 140, 1

Sitnikov, K. 1960, Dokl. Akad. Nauk. USSR, 133, 303

Tél, T., Gruiz, M.: *"Chaotic dynamics."* Cambridge Univ. Press, Cambridge, pp. 201-202, 338 (2006)

Uzer, T., Lee, E., Farrelly, D.: *"Chaotic dynamics."* Cambridge Univ. Press, Cambridge, pp. 201-202, 338 (2006)

PADEU | PADEU **20**, 179 (2011)
ISBN 963 463 557

BIRKHOFF NORMAL FORM AND REMAINDER OF THE SITNIKOV PROBLEM

Christoph Lhotka

Dipartimento di Matematica, Università di Roma Tor Vergata, Via della Ricerca Scientifica 1, I-00133 Roma (Italy)

E-mail: `lhotka@mat.uniroma2.it`

Abstract
We investigate the Birkhoff normal form of the Sitnikov problem up to normalization order 12 in the small parameters, the eccentricity e of the primaries and the initial distance η of the third body from the common barycentre. We derive the main frequencies of the massless body within the parameter range $e \leq 0.2$ and $\eta \leq 0.1$ and compare the results with direct numerical integration of the original equation of motion. We investigate the influence of the remainder on the normal form solution and give local stability estimates close to the central equilibrium configuration based on it.
Keywords: *Normal form, remainder, normalized solution, normal frequencies*

1 Introduction

We consider a subsystem of the spatial restricted three body problem, with special system parameters and geometrical configuration (Fig. 1). Two primary bodies with masses $m_1 = m_2$ are moving on Keplerian orbits around their common barycentre. We set the invariant plane of motion, formed by the primaries to be the (x, y)-plane in Cartesian coordinates and let a third massless body m moving perpendicular to that plane. We label by $r(t), z(t)$ the distance from the origin of the primaries and the third body respectively for given time t and label by $v_z(t)$ the velocity of the massless body. Starting the third body along the z-axis with given initial position $z(0)$ and velocity $v_z(0)$ the body performs oscillatory type motion through the barycentre only.

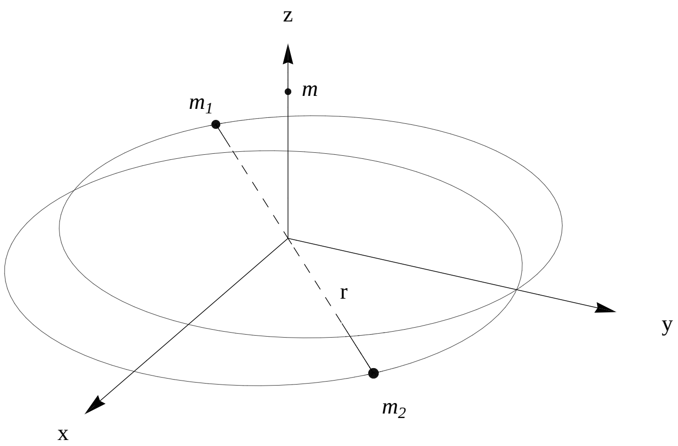

Figure 1: *Geometry of the Sitnikov problem. Two primaries* $m_1 = m_2$ *move on Keplerian orbits around their common barycentre with distance* $r = r(t)$*. A massless third body* m *moves perpendicular to the plane along the* z*-axis only.*

The system was investigated by Sitnikov to show the existence of oscillatory motion in the 3–body problem (Sitnikov , 1960). It is as much as simple without loosing the main qualitative features of more realistic models found in Celestial mechanics. The system can be seen as a generalization of the integrable MacMillan problem, where the eccentricity is equal to zero and the 2-center problem, in which the positions of the primary masses are kept constant and the third body can move arbitrarily in the plane formed by the primary bodies. Although the Sitnikov problem is one dimensional the motion of the small mass can not be written in terms of quadratures. Therefore it allows stable and unstable motion as well quasiperiodic and chaotic phase space trajectories.

The problem was investigated in great detail in Moser's book (Moser , 1973). From that time on, the system served as the basic model for various numerical and analytical investigations (e.g. Dvorak (1993), Hagel & Lhotka (2005)). The problem was further generalized, so that the third body can move off the z-axis (Soulis et al. , 2007) as well to the case when the third body has a finite mass (Hagel , 2009). More recent investigations have been performed by (Bountis & Papadakis , 2009) who extended the problem to an arbitrary number of primary masses as well by (Érdi & Kovács , 2009) who investigated transient chaos in the Sitnikov problem.

The outline of the present note is as follows: we setup the mathematical formulation and derive an approximate Hamiltonian flow of the system in action angle variables in Section 2. For this reason we expand the potential of the original Hamiltonian around the central equilibrium and introduce the eccentricity e and the initial distance η as small parameters. In Section 3 we summarize the main steps behind the normalization algorithm. Using a sequence of canonical transformations, close to identity, we remove the dependency on the angles to higher orders. The Birkhoff normal form of the Sitnikov problem of order 12 in the small parameters is given at the end of this Section. We use it to derive the normalized frequencies of the problem and compare them with the dominant frequencies found in the time series of direct numerical integrations of the equations of motion. To this end we analyze the influence of the remainder, not in normal form, in Section 4 and give a kind of local stability estimate. The summary of the present study together with the conclusions and an outlook on ongoing investigations is put at the end of this Section.

2 The approximate Hamiltonian flow

If we set the gravitational constant G, the total mass of the system $m_1 + m_2$ as well the unit distance equal to unity the revolution period of the primaries is given by $P = 2\pi$. In this setting the Hamiltonian system of the third body, derived from the kinetic and potential energy reads:

$$H(z, v, t) = \frac{{v_z}^2}{2} - \frac{1}{\sqrt{z^2 + r(t)^2}}, \tag{1}$$

$$\frac{dz}{dt} = \frac{\partial H}{\partial v_z}, \quad \frac{dv_z}{dt} = -\frac{\partial H}{\partial z},$$

leading to the equation of motion in the Newtonian framework:

$$\ddot{z} = -\frac{z}{\left(r(t)^2 + z^2\right)^{3/2}}.$$

The system depends on time through $r(t)$, itself being a function of the eccentricity e and mean anomaly M of the primary bodies respectively. Setting

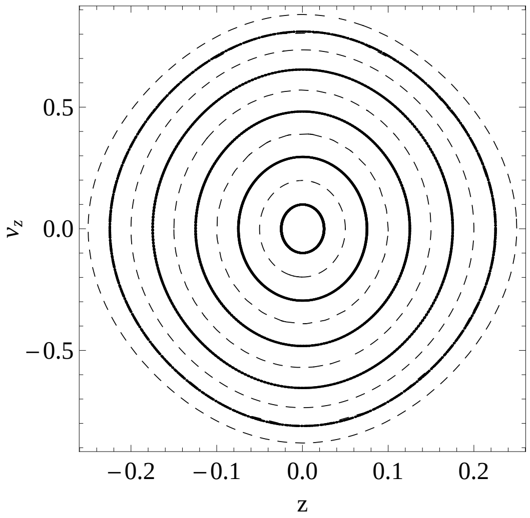

Figure 2: *Comparison of the time evolution of initial conditions obtained from the approximate Hamiltonian flow (dashed) with direct numerical integrations (thick) for* $e = 0.2$*. The present approach is valid only in the limited domain of the phase space around the central equilibrium point.*

$t_0 = 0$ together with $n = 1$ in $M = nt + t_0$ the two primaries pass the pericentre at $t = 2\pi k, k \in \mathbb{Z}$. In elliptic motion of the primary bodies and for small values of e we may expand $r(t)$ into:

$$r(t) = \frac{1}{2}\left(1 + \frac{e^2}{2} - 2e\sum_{\gamma=1}^{\infty}\frac{\partial J_\gamma(\gamma e)}{\partial e}\frac{\cos(\gamma t)}{\gamma^2}\right),$$

where J_γ are Bessel functions of the 2nd kind (Stumpff , 1959). Furthermore we restrict our investigation to small oscillations of the third body, $z(t)/r(t) \to 0$, and may expand the potential in the Hamiltonian accordingly:

$$-\frac{1}{\sqrt{z^2 + r(t)^2}} = -\sum_{k=0}^{\infty}\begin{pmatrix} -1/2 \\ k \end{pmatrix}\frac{z^{2k}}{r(t)^{2k+1}}.$$

The approximate system is integrable for $e = 0$ and reduces to a harmonic oscillator with frequency $\omega_0 = 2\sqrt{2}$. It is natural to introduce rescaled action angle variables of the form:

$$\begin{aligned} z &= \sqrt{{\omega_0}^{-1}\eta J_1}\sin(\phi_1), \\ v_z &= \sqrt{\omega_0 \eta J_1}\cos(\phi_1), \end{aligned}$$

where η labels the (small) distance from the equilibrium and (J_1, ϕ_1) is the pair of conjugated variables of order unity. Replacing the time t by ϕ_2 and extending the phase space via its conjugated action variable J_2 we find the approximate Hamiltonian, valid near the origin in phase space in the form:

$$H_* = \omega_0 J_1 + J_2 + \sum_{k=1}^{N} q_k\left(J_1; e, \eta\right) + \sum_{(k_1,k_2)\in\mathbb{Z}^2} p_{k_1,k_2}\left(J_1; e, \eta\right)\cdot\cos\left(k_1\phi_1 + k_2\phi_2\right). \tag{2}$$

where p, q are polynomial functions in e and η. A comparison of the phase space region close to the center of the approximate Hamiltonian flow and the original equations of motion is shown in Fig. 2. The Hamiltonian model is only valid close to the central equilibrium point.

3 Birkhoff normal form

By means of successive Lie-transformations we seek for a sequence of canonical transformations $\{w_s\}_{s=1,\dots,r}$ from intermediate $\left({J_m}^{(s)}, {\varphi_m}^{(s)}\right)$ to new variables $\left({J_m}^{(s+1)}, {\varphi_m}^{(s+1)}\right)$ such that in the final variables $J'_m \equiv {J_m}^{(r)}$ and $\varphi'_m \equiv {\varphi_m}^{(r)}$ with $m = 1, 2$ we get the normalized Hamiltonian flow (Birkhoff normal form):

$$H'\left(J'_1, J'_2, \phi'_1, \phi'_2; e, \eta\right) = Z^{(r)}\left(J'_1, J'_2; e, \eta\right) + R^{(r+1)}\left(J'_1, \phi'_1, \phi'_2; e, \eta\right)$$

$$\begin{aligned} \frac{d\phi'_m}{dt} &= \frac{\partial H'}{\partial J'_m} = \frac{\partial Z^{(r)}}{\partial J'_m} + \frac{\partial R^{(r+1)}}{\partial J'_m}, \\ \frac{dJ'_m}{dt} &= -\frac{\partial H'}{\partial \phi'_m} = -\frac{\partial R^{(r+1)}}{\partial \phi'_m}, \end{aligned}$$

where r is the order of normalization and $Z^{(r)}$ and $R^{(r+1)}$ are called the normal form and remainder respectively. Note, that the non resonant normal form does not depend on the angles. Assuming the remainder small the normal form solution to the system is therefore given by $(m = 1, 2)$:

$$\begin{aligned} \phi'_m(t) &= \omega'_m\left(J'_1(0), J'_2(0)\right)t + \phi'_m(0), \\ J'_m(t) &= J'_m(0) \end{aligned} \tag{3}$$

which implies linear motion on the $\mathbb{T}^2$-torus with conserved actions and fixed frequencies for all times, where the shifted frequency in terms of the normalized variables reads ($m = 1, 2$):

$$\omega'_m \left(J'_1, J'_2\right) = \frac{\partial Z^{(r)}}{\partial J'_m}.$$

For the determination of the sequence of generating functions $\{w_s\}$ it suffices to solve the homological equations of the form (Efthymiopoulos et al. , 2004):

$$\langle h_0, w_s \rangle + \tilde{h}_s = 0$$

where at normalization order s the function $\tilde{h}_s$ is the oscillating part in $h_s = \bar{h}_s \left(J_1, J_2\right) + \tilde{h}_s \left(J_1, J_2, \phi_1, \phi_2\right)$, $\langle\cdot\rangle$ are the Poisson brackets and $h_0 = h_0 \left(J_1, J_2\right)$ is the integrable approximation of the original Hamiltonian. In the case of the Sitnikov problem we have:

$$\begin{aligned} h_0 &= \omega_0 J_1 + J_2, \\ \tilde{h}_s &= \sum_{(k_1,k_2)\in\mathbb{K}\backslash\{0\}} \hat{h}_{s,k_1,k_2} \left(J_1, \phi_1, \phi_2\right) e^{i(k_1\cdot\phi_1 + k_2\cdot\phi_2)} \end{aligned}$$

therefore using the form

$$w_s = \sum_{(k_1,k_2)\in\mathbb{K}\backslash\{0\}} \hat{w}_{s,k_1,k_2} \left(J_1, \phi_1, \phi_2\right) e^{i\cdot(k_1\cdot\phi_1 + k_2\cdot\phi_2)}$$

for the generating functions we immediately find

$$w_{s,k_1,k_2} = \frac{\hat{h}_{s,k_1,k_2}}{i\left(k_1\cdot\omega_1 + k_2\cdot\omega_2\right)} \quad \forall\left(k_1, k_2\right) \in \mathbb{K}\backslash\{0\}$$

to be left with the normal form contributions $\bar{h}_s \left(J_1, J_2\right)$ at normalization order s only.

Remark: The index set $\mathbb{K}\backslash\{0\}$ is strongly connected to the normalization order s and therefore to the oscillating parts $\tilde{h}_s$, stemming from the approximate Hamiltonian flow of the Sitnikov problem proportional to $p_{k_1,k_2}\left(J_1; e, \eta\right)$ in Eq. (2). Moreover, the normal form terms $\bar{h}_s$ are related to the contributions of order s in the functions $q_k\left(J_1; e, \eta\right)$ in the same equation. The role of s is to group terms of same orders of magnitude in H_* and to ensure that the inequality

$h_s < h_{s+1}$ is fulfilled for $s = 1, \ldots, r$. The norm of the terms is connected with the size of the parameters e and η. We checked numerically by use of d' Alembert´s criterion that the convergence of the series expansion in the space of parameters $(e \times \eta)$ is given by identifying h_s with terms proportional to $e^a {J_1}^{2b}$, where $a + 2b = s$, motivated due to the fact, that $\eta J_1 \propto z^2$. The region of convergence for this choice of the book keeping parameter s is bounded by $e \leq 0.2, \eta \leq 0.2$. The normal form for the approximate Hamiltonian at order $r = 12$ of the third body for parameters (e, η) within the domain of convergence turns out to be:

$$
\begin{aligned}
Z^{(12)}_{e,\eta} = {}& 2\sqrt{2} J_1' + J_2 + \frac{21 e^2 J_1'}{31\sqrt{2}} + \frac{89607 e^4 J_1'}{238328\sqrt{2}} + \frac{2772153831 e^6 J_1'}{34657504\sqrt{2}} - \\
& \frac{895725 e^8 J_1'}{9982\sqrt{2}} + \frac{693 e^{10} J_1'}{128\sqrt{2}} - \frac{9\eta J_1'^2}{4} - \frac{8919 e^2 \eta J_1'^2}{7688} - \frac{139122171 e^4 \eta J_1'^2}{753424} + \\
& \frac{6145605 e^6 \eta J_1'^2}{9982} - \frac{51975}{512} e^8 \eta J_1'^2 + \frac{47 \eta^2 J_1'^3}{32\sqrt{2}} + \frac{1605986985 e^2 \eta^2 J_1'^3}{15622016\sqrt{2}} - \\
& \frac{7096897485 e^4 \eta^2 J_1'^3}{3527552\sqrt{2}} + \frac{28875 e^6 \eta^2 J_1'^3}{32\sqrt{2}} - \frac{125 \eta^3 J_1'^4}{1024} + \frac{777503175 e^2 \eta^3 J_1'^4}{1007872} - \\
& \frac{606375}{512} e^4 \eta^3 J_1'^4 - \frac{5433 \eta^4 J_1'^5}{64\sqrt{2}} + \frac{218295 e^2 \eta^4 J_1'^5}{256\sqrt{2}} - \frac{53361 \eta^5 J_1'^6}{1024}
\end{aligned}
$$

We compare the frequency, derived from the normal form (Fig. 3, left) with the frequency, obtained by frequency analysis of the orbit obtained by direct numerical integration of the original equation of motion (Fig. 3, right). The former is obtained by substituting the values for e and η into the derivative of the normal form with respect to J_1', the latter by a fast Fourier transform method. The small differences in the frequencies is i) due to the approximate Hamiltonian model, only valid close to small parameters in e and η, ii) due to the shift of the frequencies along the normal form construction and iii) due to the fact, that we neglect the remainder in the equation for the frequencies, which is present in the original equation of motion.

4 Estimates of the remainder

In the previous Section we found, that the influence of the remainder on the normal form solution can become non neglectable, depending on the actual value of the small parameters. Due to this fact the normal form solutions in Eq. (3) are accurate for short times only. Nevertheless one can ask for the stability time

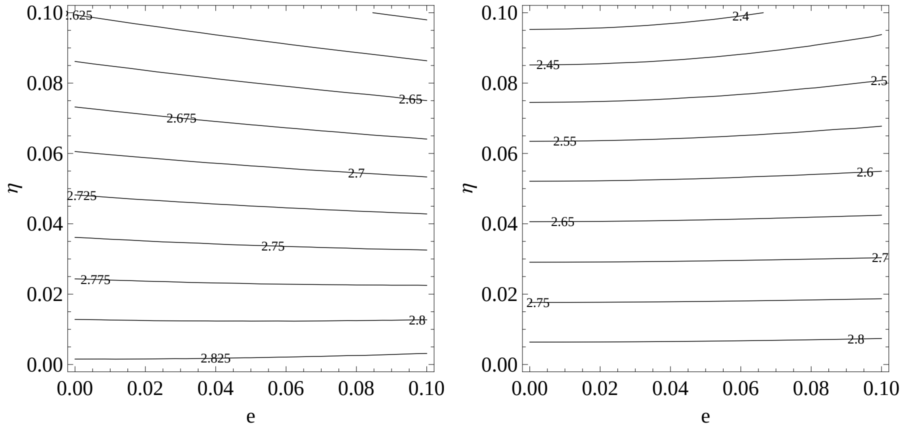

Figure 3: *Normalized frequencies of the motion of the third body in the Sitnikov problem (left) vs. the main frequency of the small body in the same parameter space obtained from direct numerical integration of the original equations of motion (right).*

T up to which the dynamics of the original systems remains close to the normal form dynamics. In a more formal way we may ask for a stability statement in the Sitnikov problem of the form $m = 1, 2$:

$$\forall |t| < T(e, \eta) : \| J_m(t) - J_m(0) \| < \alpha(e, \eta)$$

where the stability time $T = T(e, \eta)$ and the maximum variation in the actions $\alpha = \alpha(e, \eta)$ depend on the small parameters, since the norm of the remainder itself is a function of the parameters (e, η) and the normalization order r:

$$\left\| R^{(r+1)} \right\|_{e,\eta} = \left\| R^{(r+1)} \left(J_1', \phi_1', \phi_2'; e, \eta \right) \right\| \ .$$

Here we define the norm of the remainder as (σ constant, fixed):

$$\| R^{(r+1)} \|_{e,\eta} = \sum_{k \in \mathbb{Z}^2} \left| c_j \left(J_1; e, \eta \right) \right| e^{|k|\sigma} \ .$$

The question is, if it is possible to find a minimum of the norm of the remainder and connect it to the functions α and T in the stability theorem. It is possible to proof, that for the right choice of the small parameters the remainder

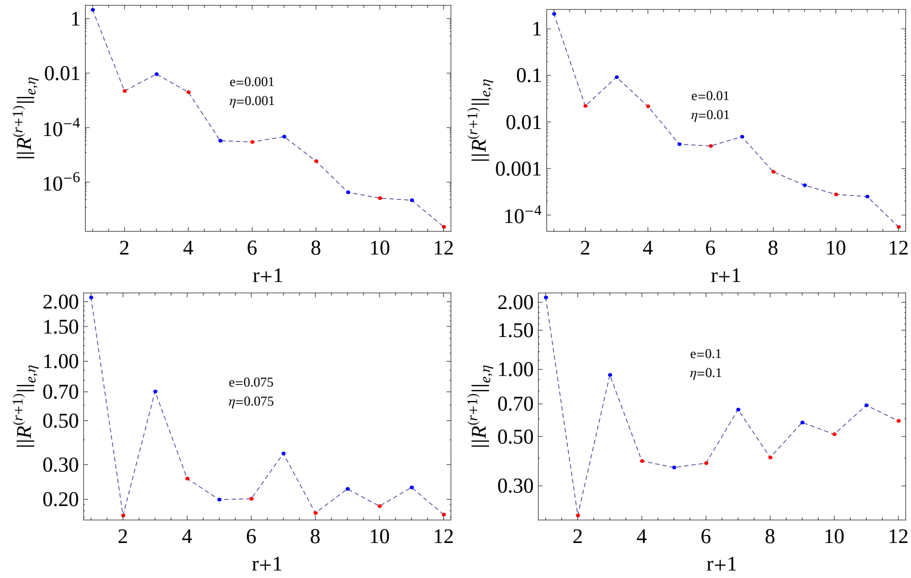

Figure 4: *Analysis of the remainder function* $R^{(r+1)}$ *vs. the order of normalization* r *for different small parameters* e *and* η *(see text). The dark and light points label odd and even orders in* r *respectively.*

becomes exponentially small, leading to exponential long stability times also. The interested reader is referred to papers concerning Nekhoroshev stability (Nekhoroshev , 1977; Pöschel , 1993; Efthymiopoulos et al. , 2004) for further reading. Nevertheless, in the case of the Sitnikov problem it is also interesting to investigate the influence of the remainder for values of the parameters e and η not leading to a Nekhoroshev-like statement.

The typical behaviour of the remainder is shown in Fig. 4. For sufficient small parameters ($e = \eta = 0.001$) the norm of the remainder decreases as the order of normalization increases (upper left). The actual size of the remainder depends on the given values for the parameters. For larger parameters $e = \eta = 0.01$ the norm of the remainder increases also (upper right). In the intermediate regime of parameters ($e = \eta = 0.075$) the remainder may decrease at the beginning but starts saturating and increasing after an optimal order of truncation (lower left). If the parameters become too large ($e = \eta = 0.1$),

e	η	time
0.001	0.001	$2.774 \cdot 10^{12}$
0.01	0.01	404120

Table 1: *Preliminary estimate of the stability time for small parameters* e *and* η *derived from the remainder of the problem.*

the norm of the remainder does not decrease at all (lower right). The normal form procedure does not converge, the effect of the remainder harms the stability of the system. In Di Ruzza & Lhotka (2010) the remainder was used to estimate the stability time in the Nekhoroshev sense, using the approach by Pöschel (1993). Based on the theorem stated there we were able to identify sets of parameters for which the exponential estimates apply. Preliminary results are shown in Table 1. The stability time for the set of parameters $e = \eta = 0.001$ turns out to be $2.774 \cdot 10^{12}$.

We derived the Birkhoff normal form of the approximate Hamiltonian flow, valid around the central equilibrium of the Sitnikov problem for small parameters e and η up to the order 12. From the normalized Hamiltonian we calculated the normalized frequencies to the system and compared with the main frequencies of the time series using Fourier analysis for various initial parameters. We explained the difference between the normal form solutions and the original dynamical system by analysing the remainder of the Hamiltonian. An estimate of the stability time for small parameters $e = 0.001$ and $\eta = 0.001$ is of the order $2.774 \cdot 10^{12}$ using the standard approach described in the paper by Di Ruzza & Lhotka (2010).

Acknowledgement

I thank Sara di Ruzza for doing the calculations of the stability time. This project is partly supported by the grants *ASI, "Studi di Esplorazione del Sistema Solare"*.

References

Bountis, T., Papadakis, K.E. 2009, Celest. Mech. Dyn. Astron., 104, 202

Ruzza, S., Lhotka, C. *Nekhoroshev estimates and Kolmogorov Arnold Moser tori in the Sitnikov problem* (submitted).

Dvorak, R. 1993, Celest. Mech. Dyn. Astron., 56, 71

Érdi, B., Kovács, T. 2009, Celest. Mech. Dyn. Astron., 105, 289

Efthymiopoulos, C., Giorgilli, A., Contopoulos, G. 2004, Journal of Physics A, 37, 10831

Hagel, J. 2009, Celest. Mech. and Dyn. Astron., 103, 251

Hagel, J., Lhotka, C., 2005, Celest. Mech. and Dyn. Astron., 93, 201

Moser, J. *Stable and Random Motions in Dynamical Systems*, Princeton University Press, Princeton, 1973.

Nekhoroshev, N. 1977, Russ. Math. Surveys, 32, 1

Pöschel, J. 1993, Math. Z., 213, 187

Sitnikov, K. A. 1960, Dokl. Akad. Nauk. USSR 133, 2, 303

Soulis, P., Bountis, T., Dvorak, R. 2007, Celest. Mech. and Dyn. Astron., 99, 129

Stumpff, K. *Himmelsmechanik I*, VEB, Deutscher Verlag der Wissenschaften, 1959.

PADEU PADEU **20**, 191 (2011)
ISBN 963 463 557

ADAPTIVE LIE-INTEGRATION

András Pál

[1]Eötvös University, Department of Astronomy, H-1518 Budapest, Pf. 32, Hungary
[2] Konkoly Observatory of the Hungarian Academy of Sciences, Konkoly Thege M. út 15-17, Budapest H-1121, Hungary

E-mail: `apal@szofi.elte.hu`

Abstract
This paper discusses some aspects of the Lie-integration method, that is a very effective algorithm for numerical solution of ordinary differential equations. We focus on the details how this method can be make adaptive, without losing (expensive) computation time.

Keywords: *Numerical methods: Lie-integration, planetary systems*

1 Introduction

Most of the problems related to celestial mechanics can be formalized using ordinary differential equations (ODEs). Namely, the given set of equations of motion (describing the dynamics of celestial bodies such as planets and stars) is written in the compact form of

$$\dot{x}_i = f_i(\mathbf{x}) \tag{1}$$

where $\mathbf{x} : \mathbb{R} \to \mathbb{R}^N$ ($\mathbf{x} = (x_1, \dots, x_N)$). One should note that all non-autonomous equation can be transformed into such an autonomous form with the introduction of a new variable. In addition, higher order ODEs can also be transformed into the above form by employing new variables. There are many types of integration schemes that aids the numerical computation of the solution of such differential equations:

- classic explicit methods (e.g. Runge-Kutta schemes, modified midpoint method, Bulirsch-Stoer algorithm, see Press et al. (1992));
- symplectic mappings (for special /Hamiltonian/ problems, e.g. Leap-Frog);
- implicit methods (e.g. modified Euler);
- Lie-integration: the power series expansion of the solution is computed and the coefficients are then summed appropriately (see Gröbner & Knapp , 1967; Hanslmeier & Dvorak , 1984).

The basic problem of the above mentioned algorithms is the following. The numerical solution is performed with a given step size, however, it is not obvious what is the "optimal" step size in order to obtain a certain (relative or absolute) precision. In practice, we can do either

- analytic estimations for this optimal step size; or
- explicit variations in the step size (until the desired precision is obtained).

With the exception of the Euler method, all of the explicit methods must compute the right-hand side of the ODE in instances that depend on the step size itself, therefore step size variation (if it turns out to be too small or too large) yields losing of computational time. On the other hand, analytic estimations might be used as a hint for the integration step size, but it is not guaranteed at all, whether the desired precision is reached or not.

In this paper we summarize the key points of the Lie-integration, focusing on the methods that make this numerical algorithm to be a very effective adaptive integrator.

2 Basics of the Lie-integration

Formally, the solution of the differential equation

$$\dot{\mathbf{x}} = \mathbf{f}(\mathbf{x}) \tag{2}$$

(where $\mathbf{f} : \mathbb{R}^N \to \mathbb{R}^N$) can be written as

$$\mathbf{x}(t + \Delta t) = \exp(\Delta t L)\mathbf{x}(t), \tag{3}$$

where $L = \sum\limits_{i=1}^{N} f_i D_i$ and $D_i = \frac{\partial}{\partial x_i}$ (L is the so-called *L*ie-operator). The exponential function can be expanded as:

$$\exp(\Delta t L) = \sum_{k=0}^{\infty} \frac{\Delta t^k}{k!} L^k. \tag{4}$$

The Lie-integration is the finite approximation of the sum in equation (4) (see also Hanslmeier & Dvorak , 1984). The advantages of this method are:

- Yields the coefficients of the Taylor-expansion (of course, these can be exploited for other purposes as well).
- The coefficients are computed using recurrence relations: the derivatives $L^{n+1}x_i$ are written as the functions of the derivatives $L^k x_j$ $(0 \leq k \leq n)$.
- If the coefficients are known, the computation of the sum is extremely fast, for *arbitrary* values of Δt. In other words, the coefficients do not have to be re-computed if the step size is altered.

However, there is a rather relevant disadvantage of this algorithm. Namely, it is not an explicit method: for each problem (set of differential equations), we need a different set of recurrence relations that should be derived independently. This derivation is highly not obvious (Hanslmeier & Dvorak , 1984; Pál & Süli , 2007) and such a derivation requires intuition. Therefore, Lie-integration is not a widespread method, although it is definitely more effective than the other techniques.

2.1 Linearized equations

Since many analysis (for instance, stability studies) require the solution of the linearized equations, here we briefly summarize the related equations if one wishes to employ a method based on the Lie-integration. As it is described in more details in Pál & Süli (2007) and Pál (2010), the solution of the linearized equations can be obtained as follows. Let us write the original set of ODEs $(\mathbf{x} : \mathbb{R} \to \mathbb{R}^N)$ and its linearized $(\xi : \mathbb{R} \to \mathbb{R}^N)$ in the form

$$\begin{aligned} \dot{x}_i &= f_i(\mathbf{x}), && (5) \\ \dot{\xi}_i &= \sum_{m=1}^{N} \xi_m \frac{\partial f_i(\mathbf{x})}{\partial x_m}. && (6) \end{aligned}$$

Additionally, let us introduce the operator

$$L = L_0 + L_\ell = f_i D_i + \xi_m D_m f_i \partial_i, \tag{7}$$

where $D_m = \frac{\partial}{\partial x_m}$ and $\partial_i = \frac{\partial}{\partial \xi_i}$ (thus, $L_0 = f_i D_i$ and $L_\ell = \xi_m D_m f_i \partial_i$). This extension of the original ODE does not modify the formal solution of equation (3), since $L_0 \xi_i \equiv 0$ for all $i = 1, \dots, N$.

Using these notations, we can write the solution similarly to the original equations:

$$\xi(t + \Delta t) = \exp(\Delta t L)\xi(t). \tag{8}$$

It has been proven (see Pál & Süli , 2007) that the derivatives $L^n \xi_k = (L_0 + L_\ell)^n \xi_k$ can be computed in a simpler manner, namely:

$$L^n \xi_k = \xi_m D_m L^n x_k = \xi_m D_m L_0^n x_k. \tag{9}$$

On the right-hand side, there are only functions of the D_m derivatives (in practice, in the form of $D_m L_0^n$).

3 Adaptive Lie-integration

The advantage of the Lie-integration scheme is that not only the step size that can be varied, but one can alter the integration order as well, simultaneously with the step size. In order to effectively reach the desired precision, an algorithm can be built as follows. Let us define a minimal and maximal integration (polynomial) order, $M_{\min}$ and $M_{\max}$. Then,

1. the integration (i.e. the computation of the coefficients and the summation) is performed for a given order M and step size Δt.

2. if the desired precision (δ) is reached earlier (so, $M < M_{\min}$), then Δt is multiplied (increased) by $M_{\max}/M_{\min}$ and the sum of the power series is calculated again (including the computation of the subsequent Lie-derivatives). This step might have to be repeated until M reaches $M_{\max}$.

3. If the precision δ is not obtained before the order $M_{\max}$, then Δt is multiplied (decreased) by $M_{\min}/M_{\max}$ and the sum is computed.

4. If the given precision is reached between $M_{\min}$ and $M_{\max}$, we proceed with the next integration step.

In practice, even machine precision ($\delta \approx 2 \cdot 10^{-16}$, for IEEE 64 bit numbers, `double` types) can be reached without any additional tricks. To make the integration as fast as possible, one has to have some proper choices for $M_{\min}$ and $M_{\max}$. Of course, these values depend on the problem, the actual implementation and the value of the desired precision δ. In practice, $M_{\min} \approx 16$ and $M_{\max} \approx 20$ is a good choice for the N-body problem and for machine precision.

3.1 Applications

The properties of a "regular" planetary system are: almost circular orbits; no orbital intersections and regular motion on shorter timescales. Below, we list some hints that can be exploited in order to make the previously discussed adaptive Lie-integration to be more efficient:

- The integration order is not the same for the bodies: for the inner planets higher orders are required for a certain step size (the orbital curvature is larger) and for the outer planets, a smaller order is adequate.

- Optimize the "crosstalk" between the coefficients: terms related to the interaction between the central body and a given planet have to be computed up to a higher order than the terms related to mutual interactions between this given planet and some outer planet(s).

- $1 \ll N$-body systems: although the initialization of the integration requires $\mathcal{O}(N^2)$ operation, we might save CPU time during the computation of the $1 \leq k$ Lie-coefficients by employing such an algorithm, thus such an implementation might be an $\mathcal{O}(N^p)$ one (where $1 \leq p < 2$).

The detailed analysis of the above mentioned possibilities are planned to be done in the near future.

3.2 Implementation

Basic implementation of the above mentioned method is available for UNIX-like systems. The "normal" implementation is a C code with ≈3,500 lines of code, including a command-line interface that parses simple configuration files, some basic chaos detection algorithms, and the full implementation of the adaptive integration (as described above).

Regarding to the computation speed, we should note that the number of basic arithmetic operations (addition, subtraction, multiplication) are scaled as

$N^2\mathcal{O}(M^2)$, while the number of more complex operations (division, exponential and power, square root) are scaled as N^2, i.e. the number of these (the most time-consuming) operations does not depend on the integration order.

4 Summary

In this paper, we showed that the Lie-integration is a very effective method, can be applied easily without losing (expensive) computation time as an adaptive integration scheme. In addition, if one needs for some analysis, the linearized equations can be derived almost automatically. Also, there are possibilities for analytical investigations if the model function is a result of an ordinary differential equation. See also (Pál , 2010) for some practical applications of the methods discussed in this paper (e.g. analysis of radial velocity variations in multiple planetary systems, uncertainty estimations, and so on).

Acknowledgement

This work has been supported by the scholarship of the Doctoral School of the Eötvös University and also in part by ESA grant PECS 98073. The support of the János Bolyai Research Scholarship of the Hungarian Academy of Sciences is also acknowledged.

References

Press, W.H., Teukolsky, S.A., Vetterling, W.T., Flannery, B.P. 1992, *Numerical Recipes in C: the art of scientific computing* Second Edition, Cambridge University Press

Gröbner, W., Knapp, H. 1967, *Contributions to the Method of Lie-Series* Bibliographisches Institut, Mannheim

Hanslmeier, A., Dvorak, R. 1984, A& A, 132, 203

Pál, A., Süli, Á. 2007, MNRAS, 381, 1515

Pál, A. 2010, MNRAS, 409, 975

Published by the Department of Astronomy of the Eötvös University
Budapest 2011